AIR-GAP TRANSMISSION LINES ON PRINTED CIRCUIT BOARDS FOR CHIP-TO-CHIP INTERCONNECTIONS

A Dissertation
Presented to
The Academic Faculty

by

Todd Joseph Spencer

In Partial Fulfillment
of the Requirements for the Degree
Doctor of Philosophy in the
School of Chemical and Biomolecular Engineering

Georgia Institute of Technology
May 2010

AIR-GAP TRANSMISSION LINES ON PRINTED CIRCUIT BOARDS FOR CHIP-TO-CHIP INTERCONNECTIONS

Approved by:

Dr. Paul A. Kohl, Advisor
School of Chemical & Biomolecular Engineering
Georgia Institute of Technology

Dr. Sue Ann Bidstrup Allen
School of Chemical & Biomolecular Engineering
Georgia Institute of Technology

Dr. Tom Fuller
School of Chemical & Biomolecular Engineering
Georgia Institute of Technology

Dr. James D. Meindl
School of Electrical and Computer Engineering
Georgia Institute of Technology

Dr. Kevin P. Martin
Nanotechnology Research Center
Georgia Institute of Technology

Date Approved: May 18, 2010

This thesis is dedicated to my beautiful wife Laura and our joyous son Coleman.

ACKNOWLEDGEMENTS

I would like to thank Dr. Paul A. Kohl for his advice, wisdom, tutelage, and patience throughout the years of my Ph.D. His knowledge and expertise in numerous scientific fields enabled broad-ranging discussions and investigations of diverse subject matter while maintaining focus on the goal of improving chip-to-chip link quality and board fabrication techniques.

I would like to thank the members of my thesis committee as well as many other faculty members who contributed their insights through discussions over the years, including Dr. Muhannad Bakir, Dr. Azad Naeemi, Dr. Andrei Federov, Dr. Yogendra Joshi, Dr. Kevin Martin, Dr. Sung Kyu Lim, Dr. Paul J. Joseph, Dr. Dennis Hess, Dr. C.P. Wong, and Dr. Gee-Kung Chang. I would like to thank Dr. Rizwan Bashirullah and Jikai Chen of University of Florida for their work designing chip-to-chip links and test structures and their continued contributions to implementing air cavity signal lines.

I would like also like to thank the many graduate students, undergraduate students, and post-doctoral researchers I have had the pleasure of working with on various projects over the years, including Dr. Bing Dang, Mark Cupta, Dr. Tyler Osborn, Dr. Ate He, Dr. Deepak Sekar, Michael Healy, Calvin King, Dr. Dhananjay Bhusari. Special thanks to Kristie DeLiso for her efforts mixing and analyzing PPC and hybrid glass formulations, Nathan Fritz for his efforts studying hybrid glass curing, and Dr. Rajarshi Saha and Dr. Yu-Chun (Brad) Chen for their assistance building air-cavity microstriplines and studying copper uptake. The completion of this work would not have been possible without the support efforts of all members of the Kohl group, Daphne Perry, and the MiRC cleanroom staff, especially Gary Spinner, Charlie Suh, Tran-Vinh Nguyen, William Kimes, and Scott Fowler.

I would like to thank my family, including my father Joseph for stimulating my interest in chemistry at a young age, mother Linda (dec.) for constantly challenging me in

mathematics, and my sister Laura for her friendship throughout childhood and beyond. Most importantly, I would like to thank my wife Laura for her love and support, for being my best friend, and for our beautiful son Coleman.

TABLE OF CONTENTS

LIST OF TABLES

LIST OF FIGURES

SUMMARY

Low-loss off-chip interconnects are required for energy-efficient communication in dense microprocessors. To meet these needs, air cavity parallel plate and microstrip lines with copper conductors were fabricated on an FR-4 epoxy-fiberglass substrate using conventional microelectronics manufacturing techniques. Copper transmission lines were separated by a composite dielectric of air and Avatrel 2000P and by a dielectric layer of air only. The composite dielectric lines were characterized to 10 GHz while the all air dielectric lines were characterized to 40 GHz. The transmission line structures showed loss as low 1.5 dB/cm at 40 GHz with an effective dielectric constant below 1.4. These novel structures show low loss in the dielectric due to the reduced relative permittivity and loss tangent introduced by the air cavity.

Transmission line structures with a composite dielectric were built by coating the sacrificial polymer poly(propylene carbonate) (PPC) over a copper signal line, encapsulating with an overcoat polymer, electroplating a ground line, and decomposing PPC to form an air cavity. The signal and ground wires were separated by a layer of 15 μm of air and 20 μm of Avatrel 2000P. Air cavity formation reduced dielectric constant more than 30 percent and loss of less than 0.5 dB/cm was measured at 10 GHz.

Residue from PPC decomposition was observed in the cavity of composite dielectric structures and the decomposition characteristics of PPC were evaluated to characterize the residue and understand its formation. Analysis of PPC decomposition based on molecular weight, molecular backbone structure, photoacid concentration and vapor pressure, casting solvent, and decomposition environment was performed using thermogravimetric analysis and extracting kinetic parameters.

Novel interaction of copper and PPC was observed and characterized for the self-patterning of PPC on copper. Copper is dissolved from the surface during PPC spincoating and interacts with the polymer chains to improve stability. The improved thermal stability allows selective patterning of PPC on copper. Decomposition characteristics, residual metals analysis, and diffusion profile were analyzed. The unique interaction could simplify air-gap processing for transmission lines.

Inorganic-organic hybrid polymers were characterized for use as overcoat materials. Curing characteristics of the monomers and mechanical properties of the polymer films were analyzed and compared with commercially available overcoat materials. The modulus and hardness of these polymers was too low for use as an air-gap overcoat, but may be valuable as a barrier layer for some applications.

The knowledge gained from building transmission line structures with a composite dielectric, analyzing PPC decomposition, interaction with copper, and comparison of hybrid polymers with commercial overcoats was used to build air-gap structures with improved electrical design. The ground metal was separated from the signal only by air. The signal wire was supported from above using 60 μm of Avatrel 8000P as an overcoat. Structures showed loss of less than 1.5 dB/cm at 40 GHz, the lowest reported value for a fully encapsulated transmission line structure.

1. INTRODUCTION

1.1. Motivation

Densely packed, energy efficient microprocessors are required for numerous high performance computing applications including cryptography, data mining, atomic physics and molecular biology simulations, and other scientific and mathematic fields. Maximizing bandwidth for chip-to-chip communication requires minimizing power dissipation in the logic circuits and interconnecting wires[1]. Elevated temperatures arising from power dissipation presents many challenges including increased power consumption due to higher transistor leakage currents and higher metal resistivity[2], signal integrity issues resulting from non-linear performance with temperature, and increased failure rates due to mechanisms such as electromigration, time dependent dielectric breakdown (TDDB), and heat induced stresses from coefficient of thermal expansion (CTE) mismatch.

Low power consumption in dense microprocessor arrays is required to maintain low processor temperatures because traditional cooling solutions (i.e. fans, heat sinks, and heat pipes) are large relative to chip size. These cooling solutions occupy large volumes above or near the chip, increasing wire lengths between adjacent processors in dense systems. The long wire length increases delay, resulting in idle processor cycles where no useful work is done. More importantly, the long wire length increases energy per bit to because larger transmit powers are required to maintain adequate signal-to-noise ratios.

Energy consumption associated with a typical logic operation in a state-of-the-art microprocessor is summarized in Figure 1.1. The details of process technology or architecture were not provided but were said to be representative of current high performance processors. The first two rows (64b Floating FMA (2 ops) and 64b Integer Add) account for the logic operation, while the remainder of the rows are contributions

from writing data for storage later and reading the data when it was needed. Most of the total energy in the operation is due to moving data across long wires on the chip and off-chip to memory, far greater than in the logic operation alone.

Energy Cost of Operations

Operation	Energy (pJ)
64b Floating FMA (2 ops)	100
64b Integer Add	1
Write 64b DFF	0.5
Read 64b Register (64 x 32 bank)	3.5
Read 64b RAM (64 x 2K)	25
Read tags (24 x 2K)	8
Move 64b 1mm	6
Move 64b 20mm	120
Move 64b off chip	256
Read 64b from DRAM	2000

Figure 1.1 Representative energy consumption in a typical high performance processor logic operation. This work was presented by William Dally at the Advanced Computing Symposium 2009 to illustrate the large energy consumption associated with moving data and the motivation for 3D integration[3].

Demand for low energy, low latency communication with memory has motivated 3-D integration, or chip stacking, which shortens wire lengths between chips and memory from centimeters to micrometers. Current integration techniques have focused on so-called 2½-D integration, where a memory die is stacked on a processor die. Reduced wire length lowers latency and reduces idle cycles when retrieving information from memory, but chip stacks add thermal resistance between processor and heat sink. Fully integrated 3-D systems layering multicore processors with memory in many tier stacks will dissipate an aggregate power in excess of 100 W/cm^2. Although die (or wafer) stacking limits are

not clear, multi-tier 3-D integration faces many challenges, including power delivery, cooling[4], and interconnection limitations[5] due to through silicon via (TSV) aspect ratio[6].

Beyond the chip-stacking limit, off-chip communication is required between memory and adjacent processors using low power signaling techniques coupled with low-loss interconnects. Specifically, the ITRS states, "a key bottleneck to the realization of high-performance microelectronic systems is the lack of low-latency, high-bandwidth, and high density off-chip interconnects. Some of the challenges in achieving high-bandwidth chip-to-chip communication using electrical interconnects include the high losses in the substrate dielectric, reflections and impedance discontinuities, and susceptibility to crosstalk[7]." In context, this statement motivates the need for optical interconnects, but optics integration suffers from processing complexity, the need for electro-optical conversion circuitry, and 90˚ routing presents challenges akin to impedance discontinuities and via stubs in electrical interconnects[8]. Electrical interconnects on cost-effective substrates such as epoxy-fiberglass FR-4 boards. The work presented here reduces substrate loss and latency and extends the length scale at which electrical interconnects outperform optics[9-10] by incorporating an air gap between two metal conductors in a monolithic buildup process.

1.2. Energy Consumption in Off-Chip Interconnects

1.2.1. International Technology Roadmap for Semiconductors (ITRS) – Key Metrics for Off-Chip Interconnects

The challenges associated with energy efficient signaling in future technology generations are highlighted using selected values from the 2007 ITRS in

Year	2012	2015	2018	2022
MPU Physical Gate Length (*nm*)	14	10	7	4
Maximum power – high performance MPUs (W)	198	198	198	198
Signal I/O – MPU (% of total pads)[a]	33.3	33.3	33.3	33.3

Total package pins – (high performance MPUs/ASICs)	5348	6191	7167	8712
Chip-to-board peripheral bus frequency (GHz)[b]	14.9	29.1	46.1	67.5

Table 1.1 Selected values from the 2007 International Technology Roadmap for Semiconductors highlighting package pin count, power, and signaling frequency. a) Signal I/O accounts for 50% of total pads in high performance ASICs. b) high performance chip-to-board frequency for differential pair point-to-point nets.

Year	2012	2015	2018	2022
MPU Physical Gate Length (*nm*)	14	10	7	4
Maximum power – high performance MPUs (W)	198	198	198	198
Signal I/O – MPU (% of total pads)[a]	33.3	33.3	33.3	33.3
Total package pins – (high performance MPUs/ASICs)	5348	6191	7167	8712
Chip-to-board peripheral bus frequency (GHz)[b]	14.9	29.1	46.1	67.5

Table 1.1 Selected values from the 2007 International Technology Roadmap for Semiconductors highlighting package pin count, power, and signaling frequency. a) Signal I/O accounts for 50% of total pads in high performance ASICs. b) high performance chip-to-board frequency for differential pair point-to-point nets

As years increase and minimum feature size (physical gate length) decreases, total chip power and percentage of chip-to-board pins dedicated to I/O remain constant for all future generations while the data rate per pin and total number of pins increases.

1.2.2. Energy per bit (pJ/bit or mW/Gbps)

Assuming the fraction of total chip power allocated to off-chip I/O remains constant, each off-chip data link must consume less energy while operating at a higher bit rate, giving rise to the metric of energy per bit. Energy per bit expressed in pJ/bit (10^{-12} J/bit) and power per data rate expressed in mW/Gbps (10^{-3}J/s / 10^{9} bit/s) are identical expressions of this metric and may be used interchangeably.

Energy per bit can be calculated based on the ITRS projections by allocating a portion of the power budget to off-chip I/O (20% of total 198 W chip power is chosen as

an approximation here). This leaves approximately 40 W for off-chip communication. Power per pin can be calculated by dividing this power (40 W) by 2904 signal I/O pins (1/3 of 8712 total pins) to yield 13.8 mW per pin. Assuming one bit per waveform (1 Gbps = 1GHz), dividing 13.8 mW per pin by the operating frequency 67.5 GHz yields 0.20 mW/Gbps or 0.20 pJ/bit.

The challenges of this 0.20 mW/Gbps milestone are highlighted in Figure 1.2, which reviews recently reported data for power efficiency versus data rate at different technology nodes. Energy per bit is more than an order of magnitude larger than the values required at the end of the ITRS. Off-chip data links in 2022 will also require data rates five to ten times larger than reported in Figure 1.2.

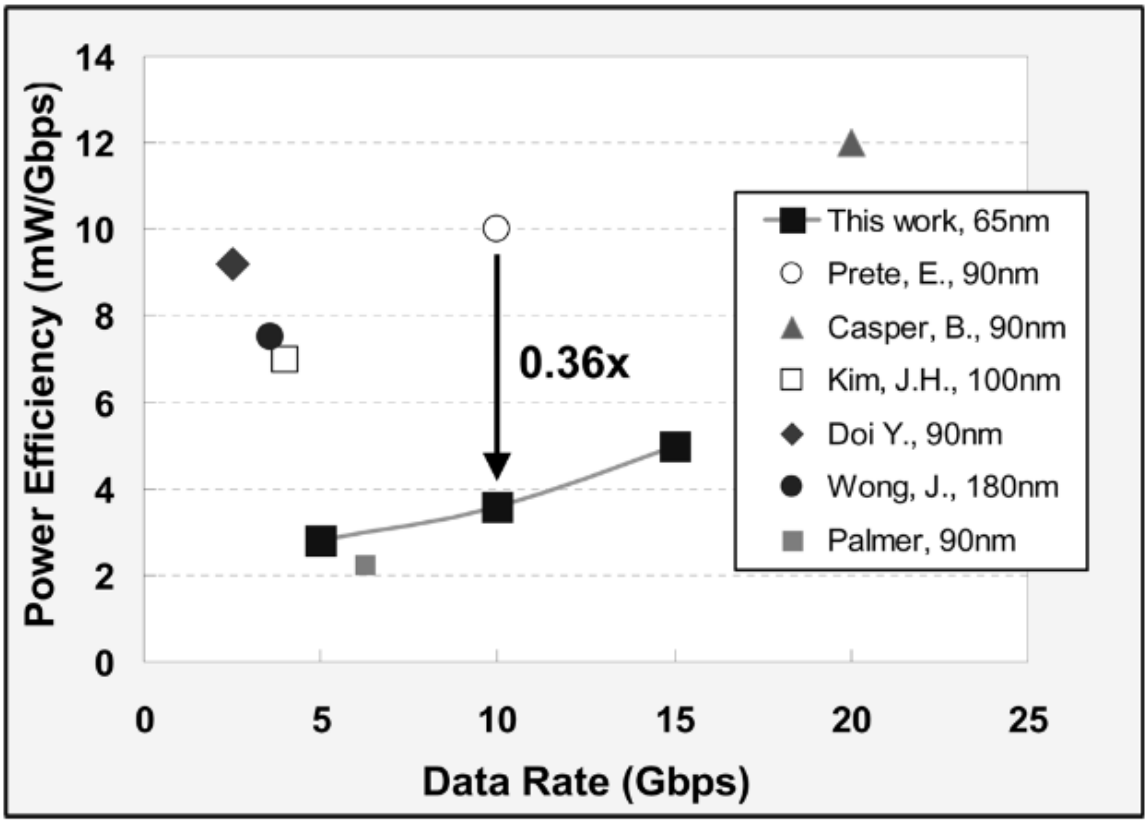

Figure 1.2 Energy per bit versus data rate reviewing some recently reported values at different technology nodes. “This work” refers to the work by [11] where this figure was reported. References to additional work may also be found here. ITRS requirements in 2022 demand mW/Gbps decrease by more than an order of magnitude and Gbps increase by nearly an order of magnitude.

1.2.3. Energy per bit dependence on data channel roll-off

Energy loss in the transmitter, receiver, and transmission media contribute to the total energy per bit. Total power consumption is highly dependent on wire length, circuit design, and technology node, but loss in the wire may contribute between 25 and 50 percent of total power consumption[9-10]. The loss in the wire is characterized by the roll-off (dB/GHz), a measure of decaying electric field strength with increasing frequency. Roll-off includes electrical loss contributions due to the length of the electrical link, the finite conductivity of the metal wires, loss through the insulator, and loss due to reflections at discontinuities like via stubs in devices and probe pads in test structures.

The roll-off in the data channel determines the optimum operating point for a given transceiver architecture. The trade-off between data channel quality, energy consumption, and bandwidth density is captured in Figure 1.3. A minimum energy per bit is achieved at a particular data rate based on the roll-off in the channel. For this particular architecture, the optimum data rate for a lossy channel (-6 dB/GHz) is approximately 2 Gb/s consuming 1 pJ/bit. A high quality channel (-0.1 dB/GHz) consumes half the energy (*ca*. 0.5 pJ/bit) while operating at ten times the data rate (20 Gb/s). Although total energy per bit is specific to circuit design in the transmitter and receiver, as the data channel quality increases, roll-off decreases, enabling larger data rates at lower energy penalties.

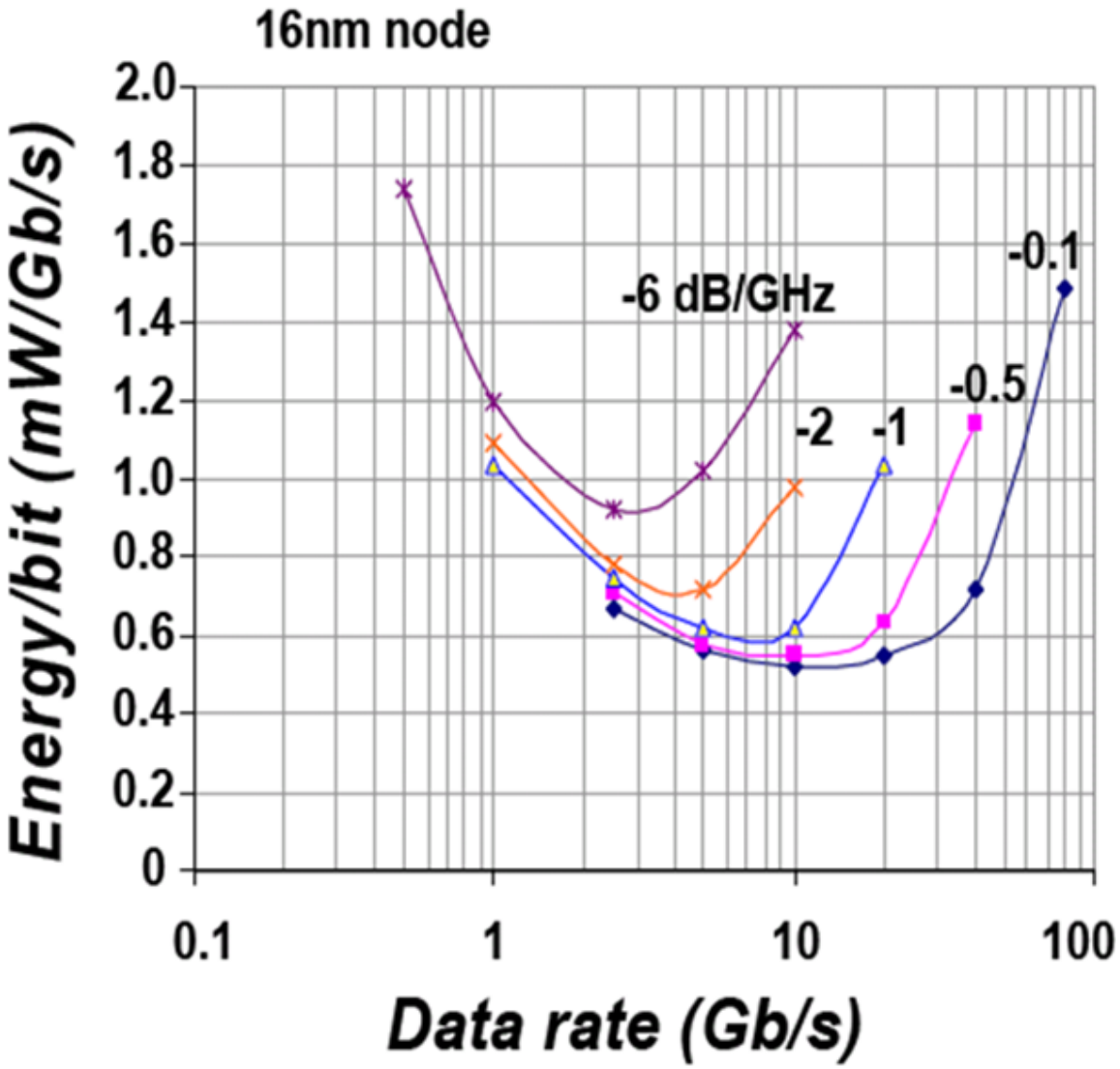

Figure 1.3 Energy per bit depends on roll-off (dB/GHz) in the data channel. Lower roll-off enables higher data rates for less energy per bit. Plot courtesy Rizwan Bashirullah (University of Florida)

1.2.3.1.Scattering parameter characterization of roll-off

Roll-off is characterized in transmission lines by measuring the scattering parameters, or S-parameters, with a network analyzer. S-parameters measure the voltage at an output port *i* relative to the voltage at an input port *j*. This is expressed as

$$S_{ij} = \frac{V_i^-}{V_j^+} \qquad 1.1$$

where

S_{ij} = element of scattering matrix for input port *j* and output port *i*

V_j^+ = voltage input at port *j*

V_i^- = voltage output at port *i*.

Thus, S_{21} is a measurement of voltage decay in an impedance matched transmission.

1.2.3.2.Roll-off due to line length

S-parameter measurements illustrating the effect of line length on roll-off are shown in Figure 1.4 Results reported in [12] for Tyco Quadroute traces showing increased roll-off (dB/GHz) for longer links. Increasing line length increases roll-off, which will increase power consumption and limit data rates.

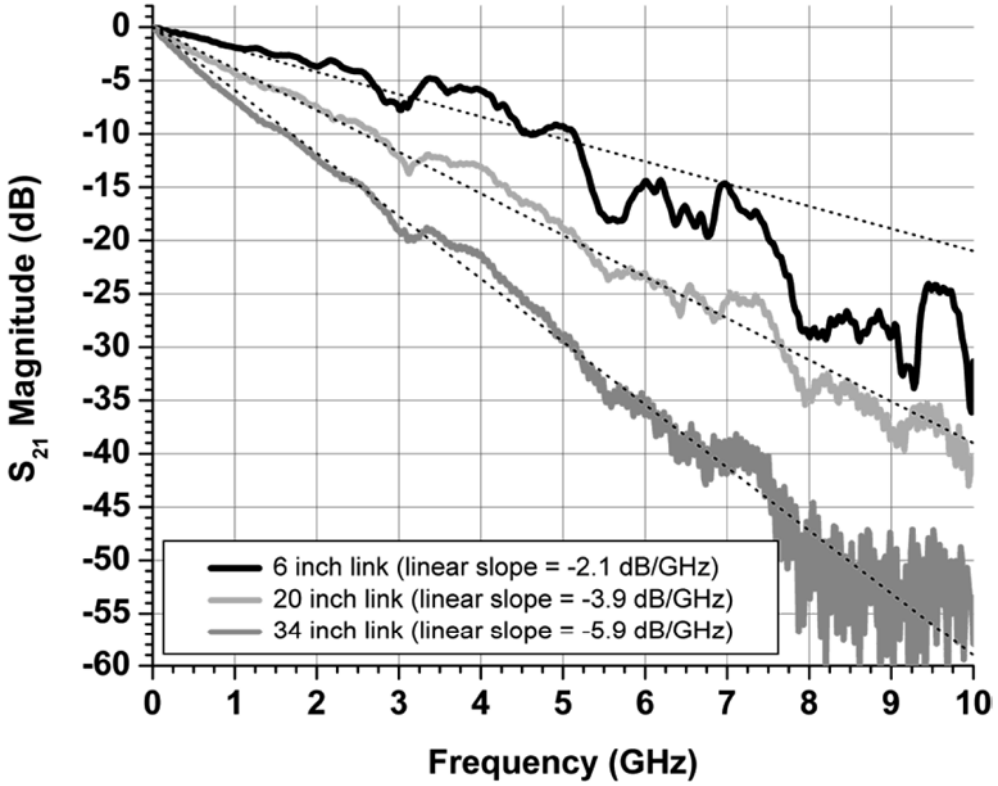

Figure 1.4 Results reported in [12] for Tyco Quadroute traces showing increased roll-off (dB/GHz) for longer links. The slope of each link is shown as a dashed line.

1.2.4. Energy consumption in electrical wires

Electric field strength decay is an alternative means to express losses due to wire length and transmission line quality. This decay is expressed in terms of its real part for an electric field propagating in the +z direction as

$$E|_{z+} = E_0 \cdot \exp(-\alpha \cdot l) \qquad 1.2$$

where l is the wire length and α is the attenuation due to contributions from the conductor and dielectric. This exponential decay is analogous to the measurement of S_{21} in the scattering matrix for passive transmission line structures.

1.2.4.1.Attenuation in the conductor

The attenuation in the conductor is due to surface resistivity of the metal and is expressed for parallel plate conductors as

$$\alpha_c = \frac{\sqrt{\frac{\omega\mu_0\varepsilon_r}{2\sigma\mu_r}}}{\eta_0 d} \quad [Np/m] \qquad 1.3$$

where:

$\omega = 2\pi f$ = angular velocity [rad/s]

f = frequency [Hz]

μ_0 = permittivity of free space [H/m]

ε_r = relative permittivity

μ_r = relative permittivity

σ = electrical conductivity [S/m]

η_0 = characteristic impedance of free space [377 Ω]

d = dielectric thickness [m]

Np = 8.686 dB.

1.2.4.2.Attenuation in the dielectric

The dielectric loss is due to shunt resistance and is expressed for parallel plates as:

$$\alpha_d = \frac{\omega\sqrt{\mu_r\varepsilon_r}\tan\delta}{2c} \quad [Np/m] \qquad 1.4$$

where:

$\omega = 2\pi f$ = angular velocity [rad/s]

f = frequency [Hz]

μ_r = relative permittivity

ε_r = relative permittivity

$\tan\delta$ = loss tangent

c = speed of light *in vacuo* [$2.998 \cdot 10^8$ m/s]

Np = 8.686 dB [13].

Attenuation expressed in Equation 1.3 and Equation 1.4 is in Nepers per meter, which must be converted to dB to account for the natural log to $\log_{10}$ conversion (1 Np equal to 8.686 dB).

1.2.4.3.Opportunities for Improvement

Examining Equation 1.3 and Equation 1.4 reveals both are dependent on the relative permittivity of the dielectric, meaning low-k dielectrics will help reduce losses due to conductor and dielectric. The conductor loss scales with the square root of frequency while dielectric loss scales linearly with frequency. If loss tangent is sufficiently large, dielectric loss exceeds conductor loss at high frequencies.

Power loss in the conductor decreases as metal conductivity increases. High conductivity metals like copper ($5.81 \cdot 10^7$ S/m) and silver ($6.30 \cdot 10^7$ S/m) are used because they minimize ohmic loss in signal and ground layers. Copper is chosen despite having a slightly lower conductivity because copper is lower in cost than gold or silver, easier to

integrate, and possesses superior electromigration resistance. These limitations restrict the choice of conductor to copper.

Low dielectric constant insulators like dry air (ε_r=1.0005) contribute less conductor and dielectric loss. Loss in the dielectric decreases as relative permittivity and loss tangent decrease. Air gaps also reduce delay and parasitic losses in the dielectric. Air cavities benefit from a dielectric constant and loss tangent approaching that of vacuum without requiring hermetic overcoats needed to seal vacuum cavities.

1.3. Board level air-gap interconnects with copper conductors

The superior combination of copper and air-gap give air-insulated transmission line structures the lowest achievable electrical loss for off-chip interconnects. Presented in this work are air-gap parallel transmission lines with copper conductors and processing advances for sacrificial and overcoat layers. The high quality data channels presented here represent an important advancement for off-chip signal wires as they approach the physical limitations of electrical signal lines. Processing advances and analysis of sacrificial poly(propylene carbonate) (PPC) and its interaction with copper add valuable tools for low cost air-cavity encapsulation of off-chip interconnects.

The thesis is divided into eight chapters including a motivating chapter, a chapter reviewing air-cavity integration in microelectronics, five core chapters, and a concluding chapter highlighting the advancements in this work and the direction of future work. Each of the five core chapters address a specific need for low-cost manufacture of air-cavity microstriplines and have been published, submitted for publication, or are in preparation for submission to a peer-reviewed journal. As such, each chapter is self-motivating with an introduction to the subject matter contained in that chapter.

Chapter 2 introduces board and package level interconnects, air-gap microstriplines, and techniques for forming air gaps. Thermal degradation of sacrificial

poly(propylene carbonate) (PPC) is discussed, especially in the presence of stabilizers and end-capping agents. Overcoat materials are also reviewed briefly.

Chapter 3 describes air-gap microstriplines and parallel plate lines fabricated on FR-4 epoxy-fiberglass boards. Capacitance and loss tangent were measured during processing and completed structures were characterized to 10 GHz by S-parameters. Effective dielectric constants between 1.5 and 1.8 were estimated by phase loss.

Chapter 4 analyzes decomposition characteristics of poly(propylene carbonate) (PPC), the sacrificial polymer used to fabricate air-gap structures. The decomposition during pattern develop and decomposition during air-cavity formation was studied. Molecular weight, backbone structure, PAG concentration and vapor pressure, decomposition atmosphere, and casting solvent were evaluated.

Chapter 5 describes a novel self-patterning technique of PPC on copper lines. PPC dissolved in solvent oxidizes the copper surface and then etched by acid in the spincoating solution. The copper inhibits PPC decomposition in the region surrounding the copper line, reducing process steps by eliminating photomask alignment.

Chapter 6 studies polymerization of inorganic-organic hybrid monomers to form novel overcoats. Curing properties were analyzed using DSC and FTIR and film hardnesses were measured by nanoindentation. Blends with tetrafunctional monomers increased modulus and hardness but films were susceptible to brittle cracking.

Chapter 7 leverages knowledge from Chapters 2 through 5 to build air-gap microstriplines with an all air dielectric layer. The electrical design from Chapter 2 was revised to place the second metal layer below the overcoat. Sacrificial polymer residue in the cavity was minimized by reducing PAG content based on analysis in Chapter 3. PPC residue on probe pads caused by interaction with copper was eliminated by protecting the probe pads with titanium as described in Chapter 4. An aqueous develop polynorbornene with increased modulus was chosen to prevent sagging overcoats in lieu of polymers evaluated in Chapter 5 because the polynorbornene had superior processing and modulus.

Chapter 8 concludes by highlighting the major achievements and contributions of this work for processing air-cavity lines, reviewing limitations to implementing air-cavity lines in future generations of high speed printed wiring boards, and discussing benefits and drawbacks of air-cavity lines in microelectronics.

2. REVIEW OF AIR DIELECTRIC INTERCONNECTS

2.1. Introduction

Structures which reduce the dielectric constant by including an air gap between metal conductors have been reported on various substrates using a wide variety of fabrication techniques. These include supporting conductors on dielectric posts and using thermally decomposing materials to form encapsulated air-gaps. These techniques are reviewed below with electrical loss characteristics when available .

2.2. Air Insulated Transmission Line Structures

Air dielectrics are currently implemented for various microwave applications because they have low power loss and phase loss due to the low relative permittivity ε_r and loss tangent ($\tan \delta$). The most commonly implemented transmission line geometries which benefit from the low loss properties of air, the microstrip line and the coplanar waveguide (CPW), are shown in Figure 2.1 Cross-section representation of low-loss transmission line structures which benefit from air dielectric. The electric field in the microstrip line extends above the signal line into the air. The co-planar waveguide has more of the electric field concentrated in the air between the edge of the conductors at the expense of a wider footprint. Both are limited to top-layer structures and lose their benefit if encapsulated..

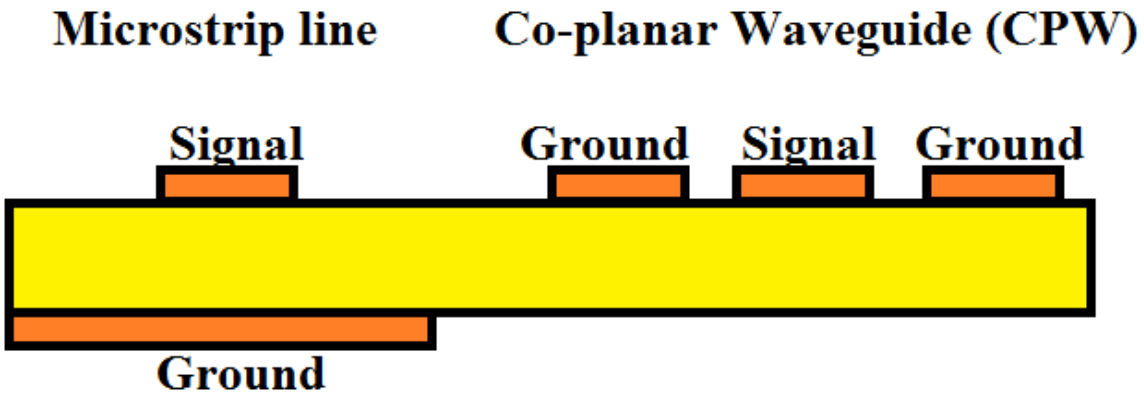

Figure 2.1 Cross-section representation of low-loss transmission line structures which benefit from air dielectric. The electric field in the microstrip line extends above the signal line into the air. The co-planar waveguide has more of the electric field concentrated in the air between the edge of the conductors at the expense of a wider footprint. Both are limited to top-layer structures and lose their benefit if encapsulated.

In the microstrip line the top layer metal serves as the signal conductor and the bottom layer metal is the ground. Although the field is concentrated in the dielectric, field lines extend into the air above the conductor, reducing overall loss but contributing to increased skew and jitter associated with phase velocity variation and slower rise time due to the quasi-TEM nature of the propagating wave. CPW lines place a signal metal between two ground metal wires on the same plane resulting in wide structures. The increased dielectric homogeneity comes at the expense of reduced line density. Both lines suffer performance degradation if encapsulated and are limited to use in top layer metals.

Although microstrip and CPW geometries benefit from lower loss in air, attenuation in the dielectric layer can be significant. Shown in Figure 2.2Figure 2.2 Results reported in [14] for microstriplines (MS) and coplanar waveguides (CPW) on silicon dioxide. W is line width and G is distance to ground. The scale on the right has been added to show loss in a 5.8 cm long line for comparison to results presented in Chapter 7. are attenuation measurements for CPW and MS lines on silicon with silicon dioxide as an insulator. Loss in a microstrip line on SU-8 nearly doubles due dielectric

loss caused by SU-8's high loss tangent (tan $\delta = 0.05$) as shown in Figure 2.3.Figure 2.3 Results reported in [15] for microstripline micromachined on SU-8. The scale on the right has been added to show loss in a 5.8 cm long line for comparison to results presented in Chapter 3 and Chapter 7.

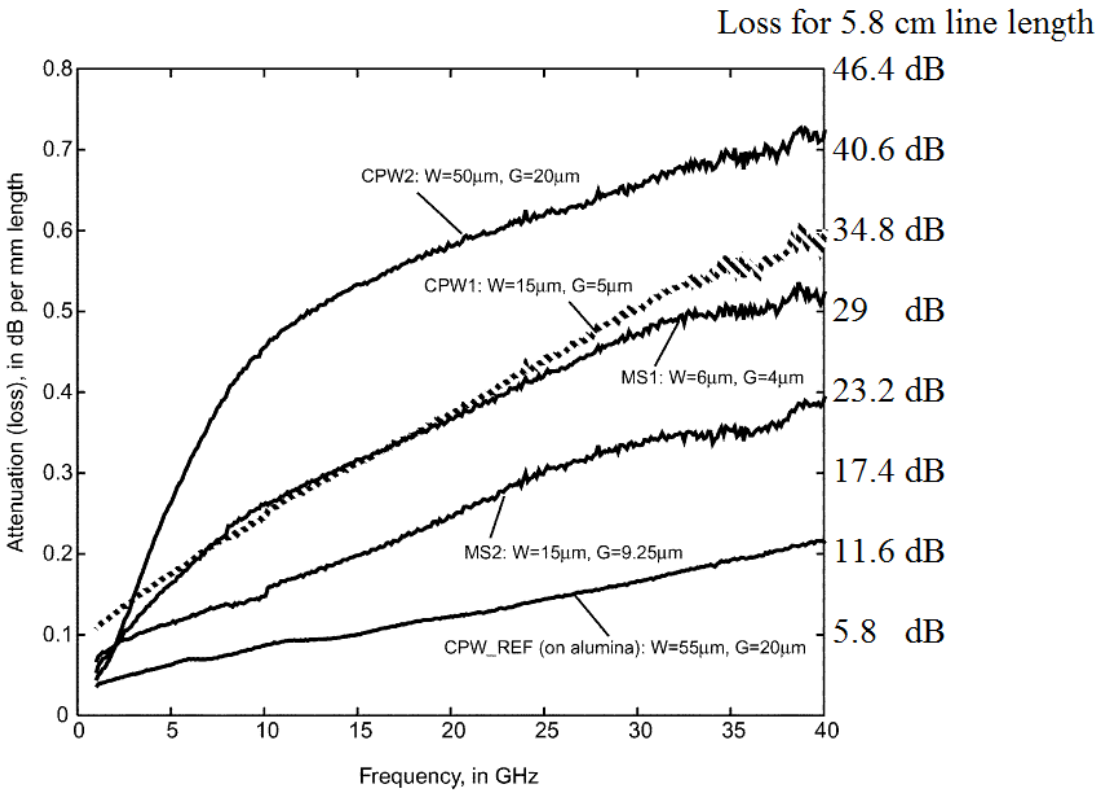

Figure 2.2 Results reported in [14] for microstriplines (MS) and coplanar waveguides (CPW) on silicon dioxide. W is line width and G is distance to ground. The scale on the right has been added to show loss in a 5.8 cm long line for comparison to results presented in Chapter 7.

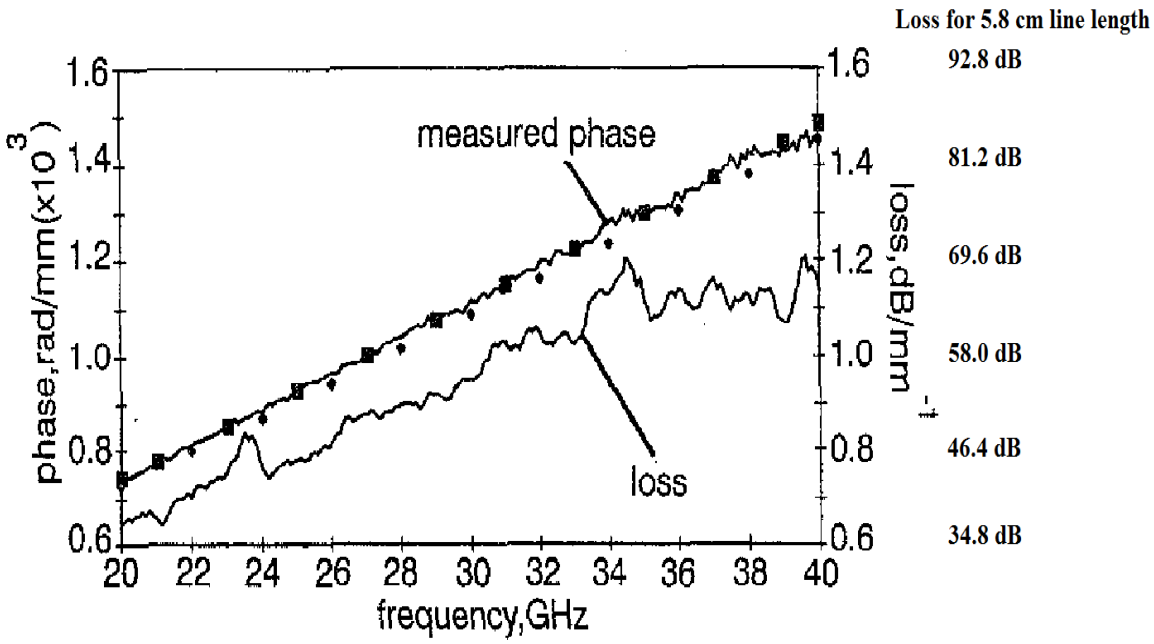

Figure 2.3 Results reported in [15] for microstripline micromachined on SU-8. The scale on the right has been added to show loss in a 5.8 cm long line for comparison to results presented in Chapter 3 and Chapter 7.

2.2.1. Dielectric post air-gap microstrip lines (DAMLs)

Air-gap microstrip lines supported dielectrics post have been reported on GaAs substrates. The air-gap is formed using a sacrificial photoresist layer which is removed by dissolution into acetone. The processing details are summarized in Figure 2.4. An SEM image of fabricated structures is shown in Figure 2.5. Different post widths visible in the image will contribute to reflections due to impedance mismatch, degrading overall performance. The attenuation characteristics measured for these lines are summarized in Figure 2.6. For comparison with results in Chapter 3 and Chapter 7, the loss in a 5.8 cm long line is shown on the right axis. Like microstrip lines and coplanar waveguides, these structures are limited to top layer metals.

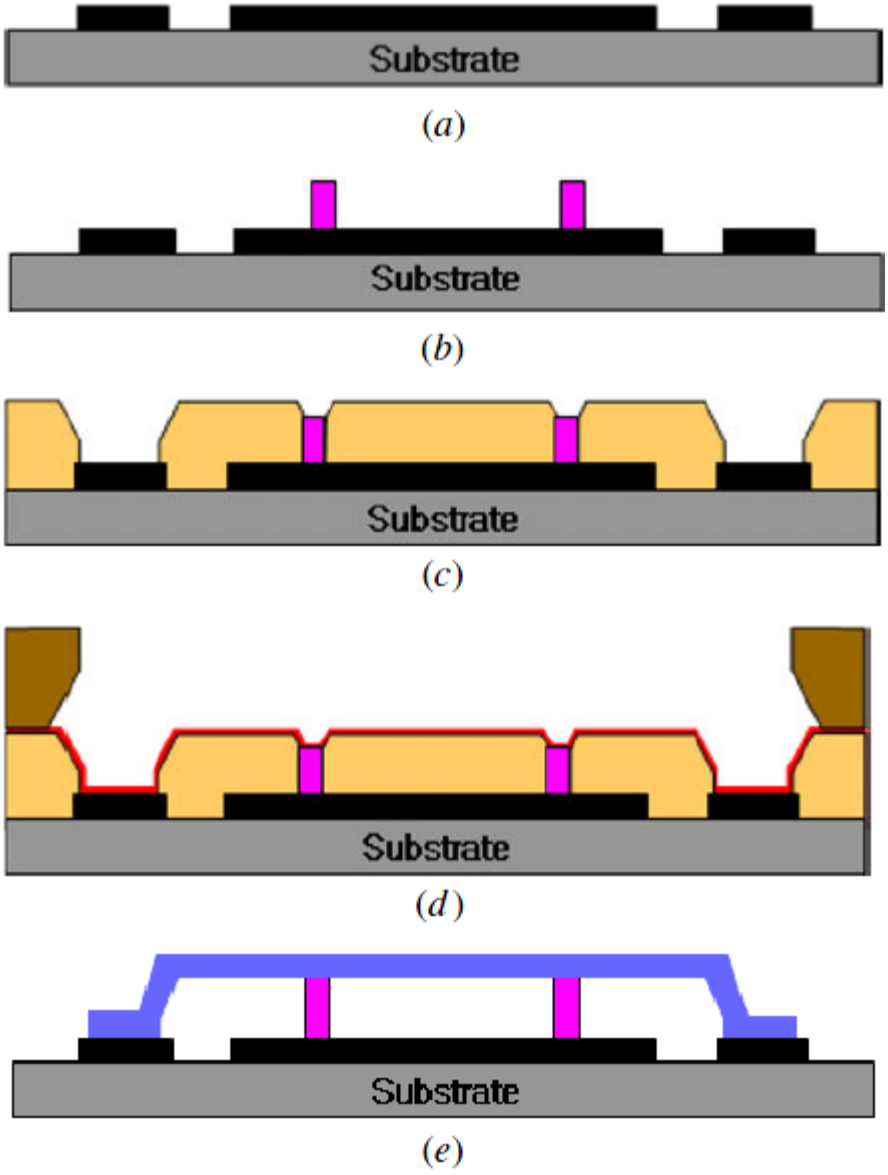

Figure 3. Fabrication process of DAML: (*a*) ground metal formation (Ti/Au 500/4000 Å), (*b*) post area formation, (*c*) sacrificial photoresist patterning and baking, (*d*) thin Au evaporation and second metal patterning, (*e*) sacrificial layer removal with the acetone.

Figure 2.4 Fabrication process reported in [16] for dielectric post air gap microstripline (DAML). Photoresist is dissolved with acetone to form an air-gap line but encapsulation and buildup of further layers is not possible. Additionally, undesireable reflections may arise from the characteristic impedance mismatch at the dielectric post supports.

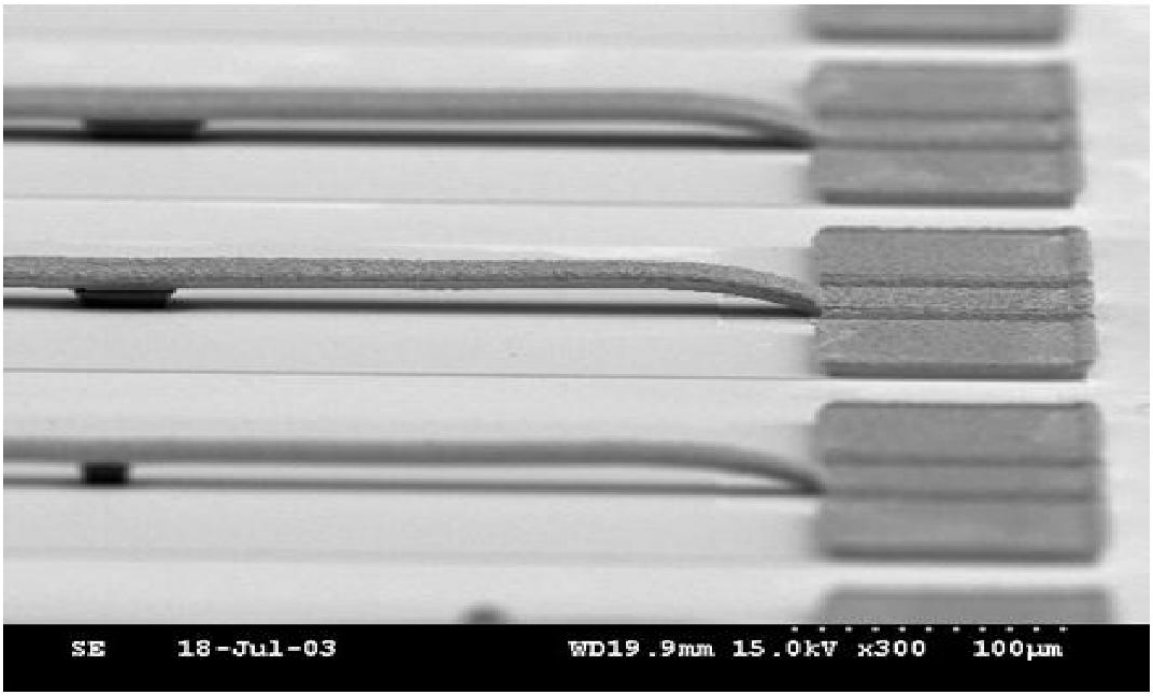

Figure 2.5 Dielectric post air gap microstripline (DAML) reported in [16]. Different post widths are visible in the SEM image

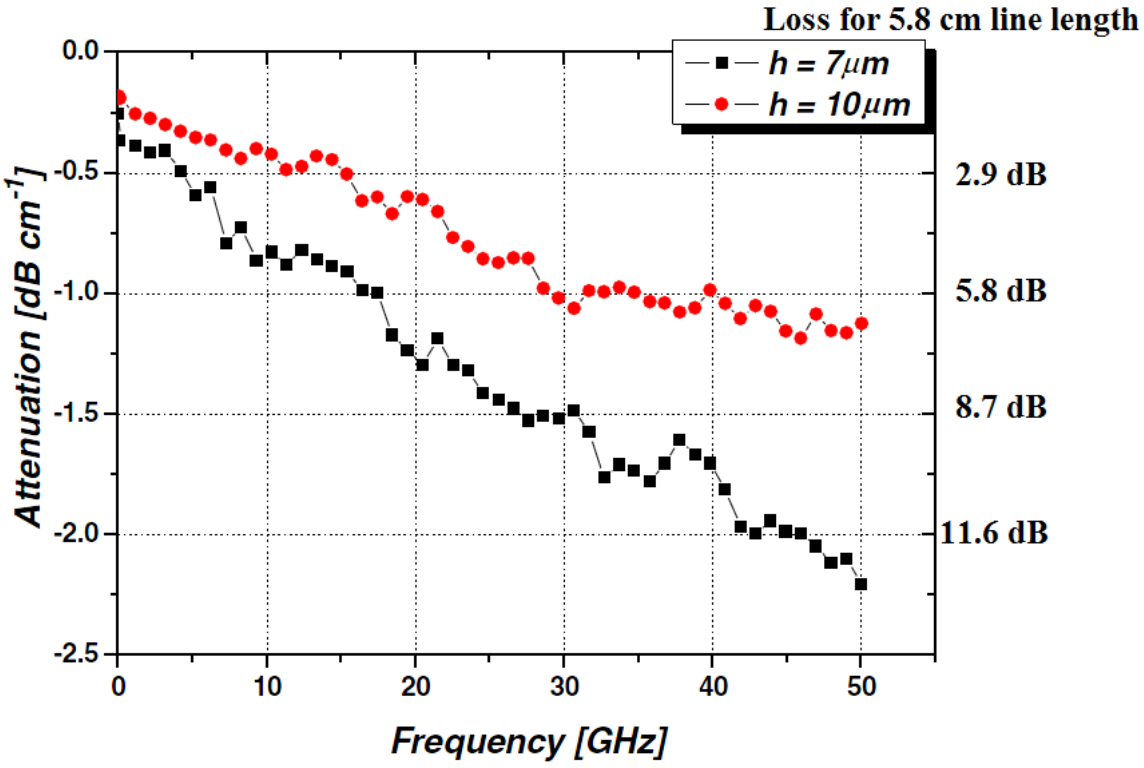

Figure 2.6 Results reported in [16] for dielectric post air gap microstripline. The scale on the right has been added to show loss in a 5.8 cm long line for comparison to results presented in Chapter 3 and Chapter 7.

2.2.2. Air cavity transmission lines on anodized aluminum

Air cavity lines on anodized aluminum have been reported for microstrip lines, coplanar waveguides, and microshield lines. The manufacturing process is summarized in Figure 2.7 Air-cavity transmission line structure build-up process on aluminum [17]. The signal line can be supported on a single strip of insulator or by dielectric posts similar to those reported for DAMLs. Shown in Figure 2.8 SEM photos of air-cavity transmission line on aluminum [17] are SEM images of the air cavity transmission lines. Although lamination of the microshield line might be viable, these lines cannot be easily encapsulated.

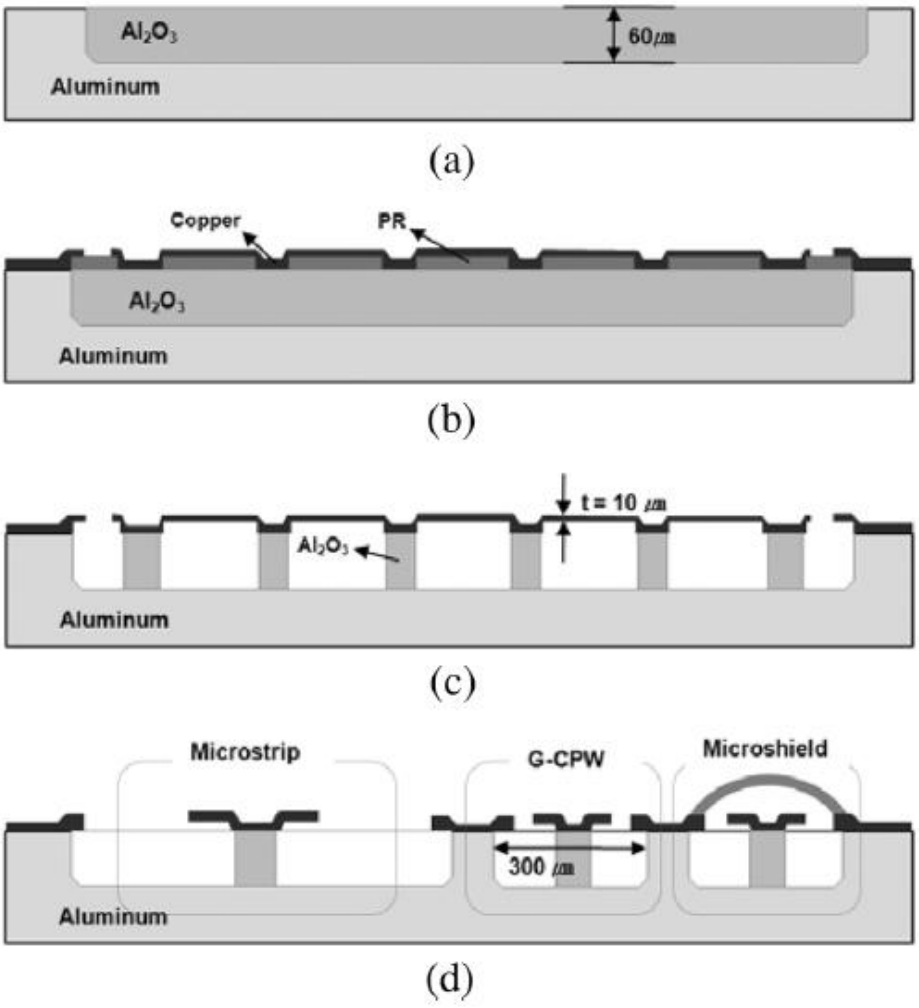

Fig. 1. Fabrication processes of air-cavity transmission lines. (a) Selective anodizing. (b) Formation of the signal metal on the sacrificial photoresist (PR). (c) Removing sacrificial PR and anodized porous alumina (Side cross-section). (d) Front cross- section of the air-cavity transmission lines.

Figure 2.7 Air-cavity transmission line structure build-up process on aluminum [17]

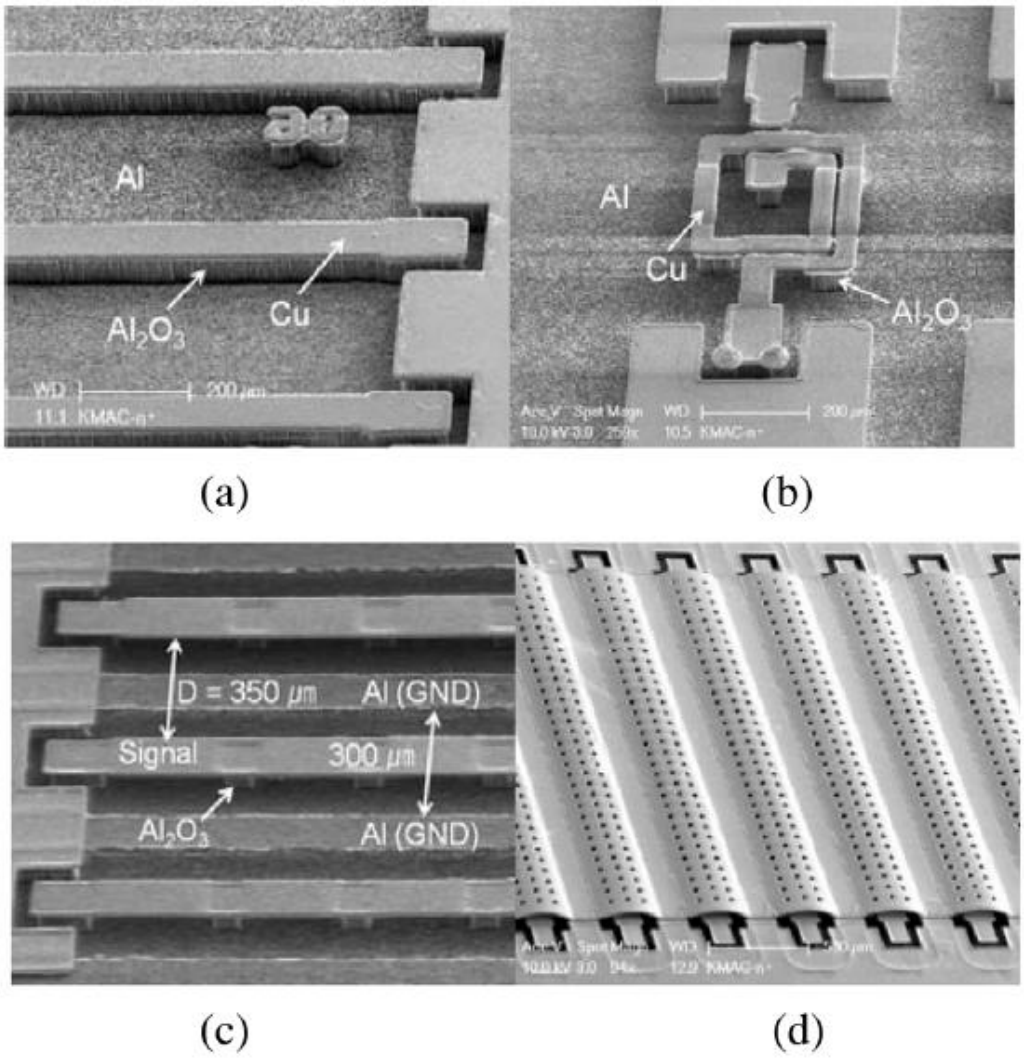

Fig. 2. SEM photograph of the fabricated air-cavity structures. (a) Normal microstrip lines after alumina etching. (b) Suspended spiral line using alumina posts. (c) G-CPWs with air-cavity. (d) Mircoshield lines with air-cavity.

Figure 2.8 SEM photos of air-cavity transmission line on aluminum [17]

3. AIR-GAP TRANSMISSION LINES ON ORGANIC SUBSTRATES FOR LOW-LOSS INTERCONNECTS

3.1. Overview

Presented in this chapter is a novel fabrication process and measured results for low-loss transmission lines with air-cladding. The transmission line structures were fabricated in parallel plate and suspended ground microstrip configurations on FR-4 and

BT substrates. The processing techniques are compatible with conventional MMIC fabrication. The air-gapped structure significantly lowers both the effective dielectric constant and the dissipation factor, resulting in lower attenuation and phase loss in the line.

The fabrication of low loss transmission line structures with an air dielectric layer is described. The channels are characterized at low frequency (10 kHz and 100 kHz) using capacitance and loss tangent and at high frequency (500 MHz to 10 GHz) using S-parameter measurements. The attenuation constant, phase constant, and quality factor were extracted from S-parameters. The incorporation of an air gap resulted in structures with effective dielectric constants between 1.5 and 1.8 and significantly lower loss tangents. The fabrication technique could be used to create more complicated air gap transmission line structures for use in monolithic microwave integrated circuits.

3.2. Introduction

Future generations of high performance microprocessors require cost-effective, manufacturable packages and substrates which lower the dielectric permittivity, provide a spatially uniform electrical environment, and which address global wiring scaling issues [1]. One area of particular interest is the propagation of high frequency signals through transmission lines without sacrificing circuit performance. This is especially important for multichip modules and high-performance servers, routers, and switches where interchip distances can be large and signal strength may be significantly degraded. A variety of material processing and signal processing techniques are currently being pursued to achieve low-loss transmission lines for these applications.

3.2.1. Drawbacks of conventional substrates

Conventional substrates used in monolithic microwave integrated circuits (MMICs), such as GaAs, or other high performance substrates, such as FR-4 and Duroid,

offer good loss characteristics, but are expensive relative to the much lower cost fiberglass/epoxy substrates based on resins of tetra-bromo bisphenol A (FR-4) and bismaleimide triazine (BT). While FR-4 is attractive for its low cost, it has a relatively high loss characteristic, which results in significant power dissipation in the dielectric. Typical FR-4 materials have dielectric constants in the range of 4.2 to 5.5 and a loss tangent of about 0.02. At high frequencies, the dielectric loss becomes the dominant loss mechanism [2] and low loss substrates are preferred.

3.2.2. Substrate integrated waveguide limitations

Substrate integrated waveguides on FR-4 optimized for low loss, low cross-talk, and maximum bandwidth were reported in [3]. Such waveguide structures achieved low-loss without multimoding and were shown to be compatible with current manufacturing technologies. However, the dimensions are large (line widths greater than 2.8 mm) and cannot be easily scaled for integration with multichip modules. This is because cut-off frequency increases as diameter decreases for TE and TM modes propagating in a rectangular cavity.

3.2.3. Complementary active signaling techniques

Digital signal processing techniques which can improve data rates are also being aggressively pursued as an alternative to passive solutions using low-loss materials. These techniques include four layer pulse amplitude modulation (PAM-4) and duobinary signaling. However, they can increase the circuit complexity and may result in increased power consumption [4]. Ideal low power signaling schemes employ active signaling techniques with low-loss electrical lines.

3.2.4. Air-gap structures for microelectronics

Previous work by Kohl et al. has presented techniques for air cavity encapsulation using an SiO_2 encapsulant deposited by plasma enhanced chemical vapor deposition and

a thermally decomposed sacrificial polymer [5]. The gaseous products from the decomposition reaction are able to permeate through the overcoat leaving an air gap with little residue. Similar encapsulation techniques using sacrificial polymers were demonstrated using Avatrel as the encapsulant material. A variety of sizes and aspect ratios were reported [6]. Fabrication of two layered or stacked air-gaps was also demonstrated [7].

3.2.5. Photodefinable polycarbonates as sacrificial materials

Work by Jayachandran et al. demonstrated air cavity formation in Avatrel with reduced decomposition temperature with the addition of small quantities of photoacid generator [8]. The acid catalyzed reaction mechanism was described and the primary products of the decomposition were shown to be acetone and carbon dioxide. The photo acid generator salts lower both the thermal and photolytic decomposition temperature via an acid-catalyzed decomposition reaction. The lower decomposition temperature has several benefits, including reduced energy needs and compatibility with organic substrates.

3.3. Background

3.3.1. Wave propagation factor and propagation velocity

The wave propagation factor, γ,of an exponentially decaying electromagnetic wave propagating in the +z direction can be expressed in terms of its real and imaginary part by:

$$\gamma = \alpha + j\beta \qquad 3.1$$

where:

α = attenuation constant [Np/m]

β = phase constant [rad/m]

$j = \sqrt{-1}$

Expressed in terms of the phase constant from Equation 3.1, the wave propagation velocity is given as

$$v_p = \frac{\omega}{\beta} = \frac{c}{\sqrt{\varepsilon_r}} \qquad 3.2$$

where:

υ_p = propagation velocity [m/s]

ω = angular velocity [rad/s]

β = phase constant [rad/m]

c = speed of light *in vacuo* [$2.998 \cdot 10^8$ m/s]

ε_r = relative permittivity [rad/m]

Thus, increased propagation velocity and reduced phase loss are achieved in materials with low dielectric constants [9], [10].

3.3.2. Attenuation in conductor and dielectric

The real component of the wave damping factor in a transmission line consists of loss contributions from the conductor and the dielectric. The conductor loss in a parallel plate waveguide can be expressed by

$$\alpha_c = \frac{\sqrt{\frac{\omega \mu_0 \varepsilon_r}{2\sigma \mu_r}}}{\eta_0 d} \qquad 3.3$$

where:

ω = angular velocity [rad/s]

μ_0 = permittivity of free space [H/m]

ε_r = relative permittivity

μ_r = relative permittivity

σ = electrical conductivity [S/m]

η_0 = characteristic impedance of free space [377 Ω]

d = dielectric thickness [m].

The dielectric loss can be expressed by

$$\alpha_d = \frac{\omega\sqrt{\mu_r \varepsilon_r}\,\tan\delta}{2c} \qquad 3.4$$

where:

ω = angular velocity [rad/s]

μ_r = relative permittivity

ε_r = relative permittivity

tan δ = loss tangent

c = speed of light *in vacuo* [$2.998 \cdot 10^8$ m/s] [9].

From Equation 3.3 and Equation 3.4, it can be seen that the conductor loss scales with the square root of frequency while the dielectric loss scales linearly with the frequency. Similar expressions for the conductor and dielectric losses in a microstrip were expressed by Hammerstad et al. using an effective dielectric constant [11]. The dielectric loss in a microstrip line is somewhat lower than in a parallel plate line, but is still usually the dominant loss mechanism at high frequencies. It is clear from Equation 3.3 and Equation 3.4 that reduction of the dielectric constant reduces the loss in both mechanisms. Transmission line structures using higher conductivity materials will have lower conductor losses while dielectric materials with lower loss tangents diminish the contribution of the dielectric.

3.3.3. Dielectric constant reduction with air-gap

In order to increase signal propagation velocity and reduce dielectric loss in a transmission line, an air-gap can be included in the dielectric layer to lower its relative permittivity [9]. The dielectric constant of an air-gapped substrate can be calculated from

$$\varepsilon_{air-gap} = \frac{\varepsilon_r (h_a + h)}{h + \varepsilon_r h_a} \quad 3.5$$

where:

ε_r = relative permittivity

h_a = air cavity thickness (μm)

h = dielectric overcoat thickness (μm)

The effective dielectric of such an air-gapped structure approaches unity when the substrate thickness is minimized[12].

3.3.4. Air-gap transmission lines for microelectronics

Air-gap transmission lines using a dielectric post for structural support were demonstrated by Jeong et al. on GaAs substrates [13]. Devices were fabricated in several conventional transmission line geometries using both surface micromachining and photolithography [14-15]. Microstrip antenna designs on Duroid and FR-4 substrates have also utilized air-gaps to achieve lower dielectric constants. The incorporation of an air insulation layer reduces the substrate loss characteristic [16-18].

Many different techniques to create air-gaps have been investigated for use in microelectronics, including oxidation of sputtered carbon [19], oxidation of photoresist and other organic materials [5], thermal decomposition of sacrificial polymers [7], reflow of photoresist [13], and dissolution of photoresist into a solvent [14-15]. The former methods require high temperatures (T>200°C), which are incompatible with organic substrate processing while the latter require a fluid path to allow for contact of the photoresist with solvent.

3.4. Experimental

Air-insulated parallel plate and suspended ground microstrip lines were created on organic substrates using CMOS-compatible processing techniques and sacrificial polymer with photoacid generator. A copper signal line was etched with a sacrificial polymer layer defined around it. The polymer is then covered with an overcoat and an electroplated ground line. Illustratesd in Figure 3.1 is a simplified process flow diagram of the build-up procedure used in the fabrication.

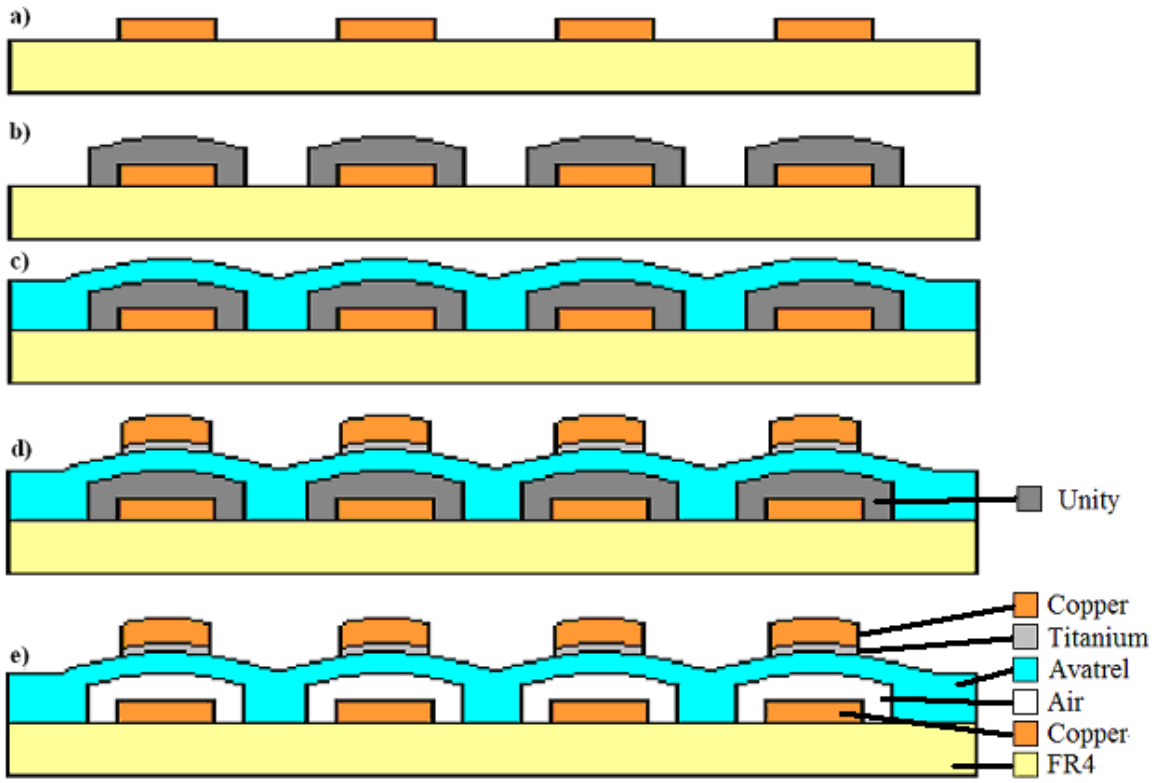

Figure 3.1 Simplified process flow diagram.

3.4.1. Signal line patterning

The substrate used was an FR-4 or BT substrate clad with 27 µm-thick copper. AZ4620 photoresist from Clariant was spun to a thickness of 10 µm onto the substrate and soft-baked at 110°C for 10 minutes. The resist was photopatterned and developed to define the 220 µm-wide transmission lines. The exposed copper was etched with a

solution of 15% H_2O_2 and 5% H_2SO_4. The photoresist was then stripped, leaving only the signal lines on the board shown in Figure 3.1a. The signal lines were 58 mm in length.

3.4.2. Sacrificial polymer patterning

The photosensitive sacrificial polymer, Unity 2203P from Promerus, LLC (Brecksville, OH) was spun onto the board to a thickness of 15 µm. Following a 10 minute soft-bake, the Unity was photodefined, developed on a hot plate at 110°C for 10 minutes and rinsed with isopropyl alcohol, leaving 600 µm-wide encapsulation regions over the signal lines as shown in Figure 3.1b.

3.4.3. Overcoat patterning

Avatrel 2000P dielectric polymer from Promerus was spun onto the board at a thickness of 20 µm over the encapsulated copper lines as illustrated in Figure 3.1c. The Avatrel was then dosed with 200 mJ/cm^2 (λ=365 nm) and developed to define regions allowing access to the probe pads.

3.4.4. Ground line patterning

An electroplating seed layer of Ti/Cu/Ti was sputtered onto the Avatrel overcoat at thicknesses of 150 Å / 1000 Å / 150 Å respectively. The titanium layers are required for adhesion of the copper to the overcoat polymer and the photoresist.

AZ4620 photoresist was again spun to a thickness of 10 µm and exposed to define an electroplating mask for ground lines of three different widths (150 µm, 220 µm, and 650 µm). The titanium layer was removed with a buffered oxide etch solution. The copper ground lines were electroplated to a thickness of 20 µm and the photoresist was stripped. The sputtered layer of titanium was etched away with BOE, the copper was etched away with a solution of 7.5% H_2O_2 and 5% H_2SO_4, and the final layer of titanium was etched

with BOE. This etched line structure, including the titanium adhesion layer between the ground copper and the overcoat polymer, is shown in Figure 3.1d.

3.4.5. Air cavity formation

The polymer overcoat was then cured in a nitrogen purged tube furnace heated to 180°C for 2 hours at a ramp rate of 3°C/min from 25°C to 150°C and 1°C/min from 150°C to 180°C. The Avatrel cured while the decomposition products of the encapsulated Unity permeated through the overcoat, leaving the structure pictured in Figure 3.1e. The structure dimensions are shown in Figure 3.2.

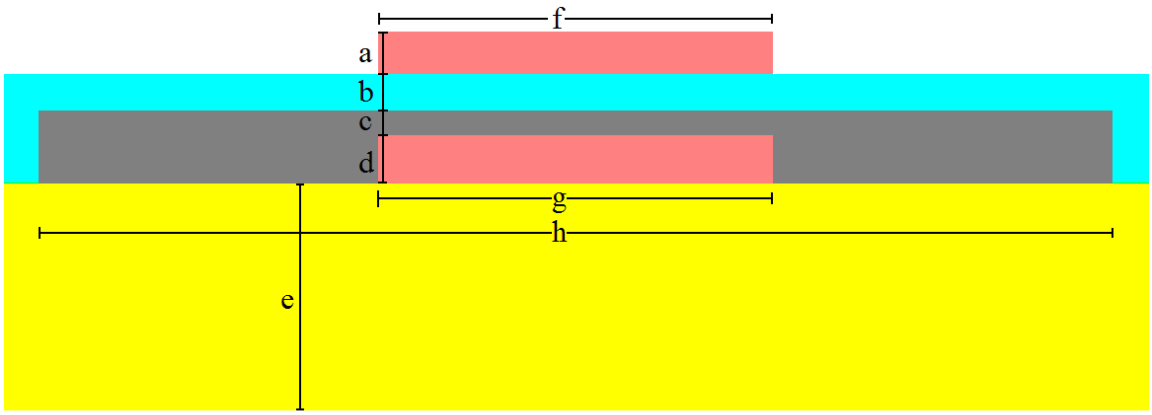

Figure 3.2 Dimensions for electrostatic and high frequency simulations. The dimensions for the parallel plate structures are a=24 µm, b=20 µm, c=15 µm, d=27 µm, e=1 mm, f=220 µm, g=220 µm, and h=600 µm. For the narrow ground line case, dimensions are the same except f=150 µm. For the suspended ground microstrip dimensions are the same except c=30 µm and f=650 µm.

3.4.6. SEM cross-sections and optical images

A scanning electron microscope (SEM) cross-section of the fabricated parallel plate line is shown in Figure 3.3 SEM of the parallel plate line. The ground line is slightly peeled back due to delamination during the dicing process. The particle in the air-gap is

also a result of the dicing process.. A line with a narrow ground line (150 µm wide) is shown in Figure 3.4. Slight residue from the sacrificial polymer is visible in the corner of the cavity but is not expected to impact performance. A top view of the probe pads for the parallel plate structure is shown in Figure 3.5.

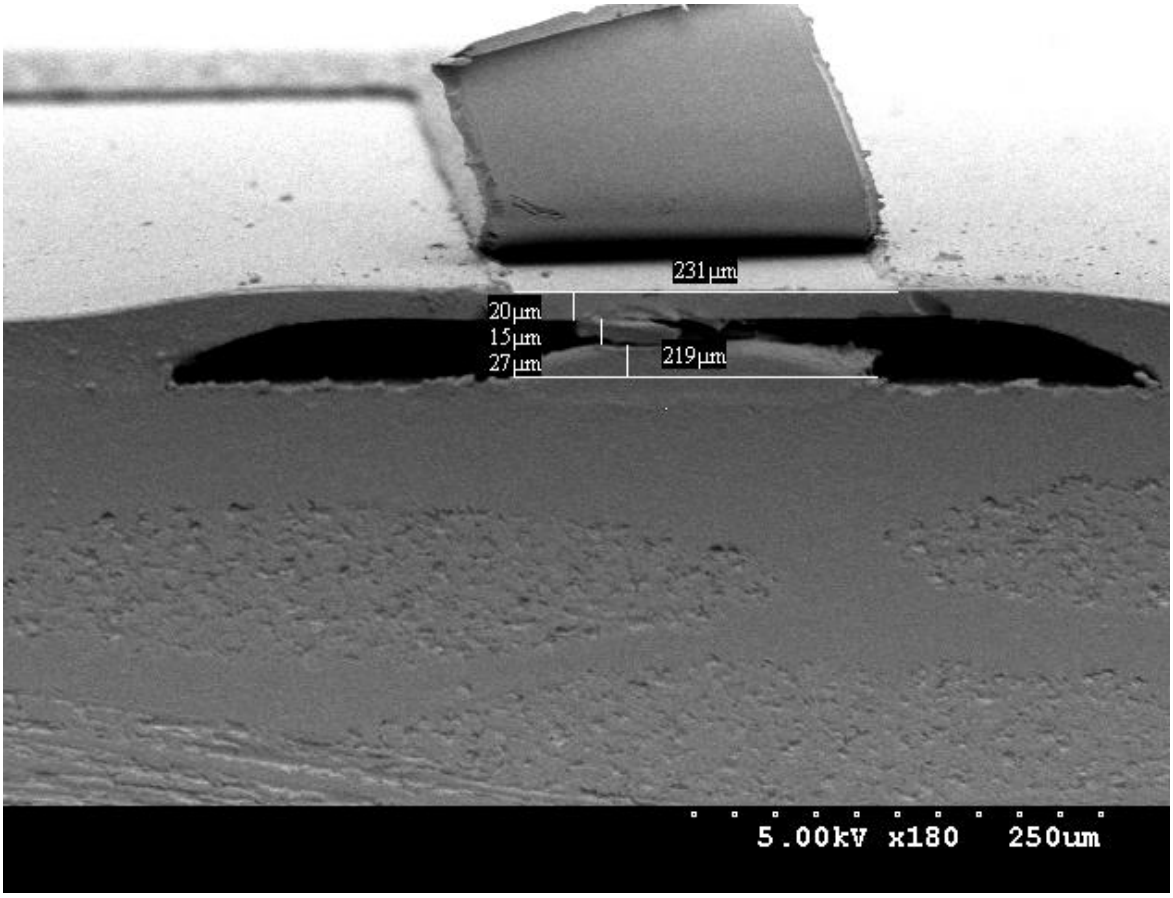

Figure 3.3 SEM of the parallel plate line. The ground line is slightly peeled back due to delamination during the dicing process. The particle in the air-gap is also a result of the dicing process.

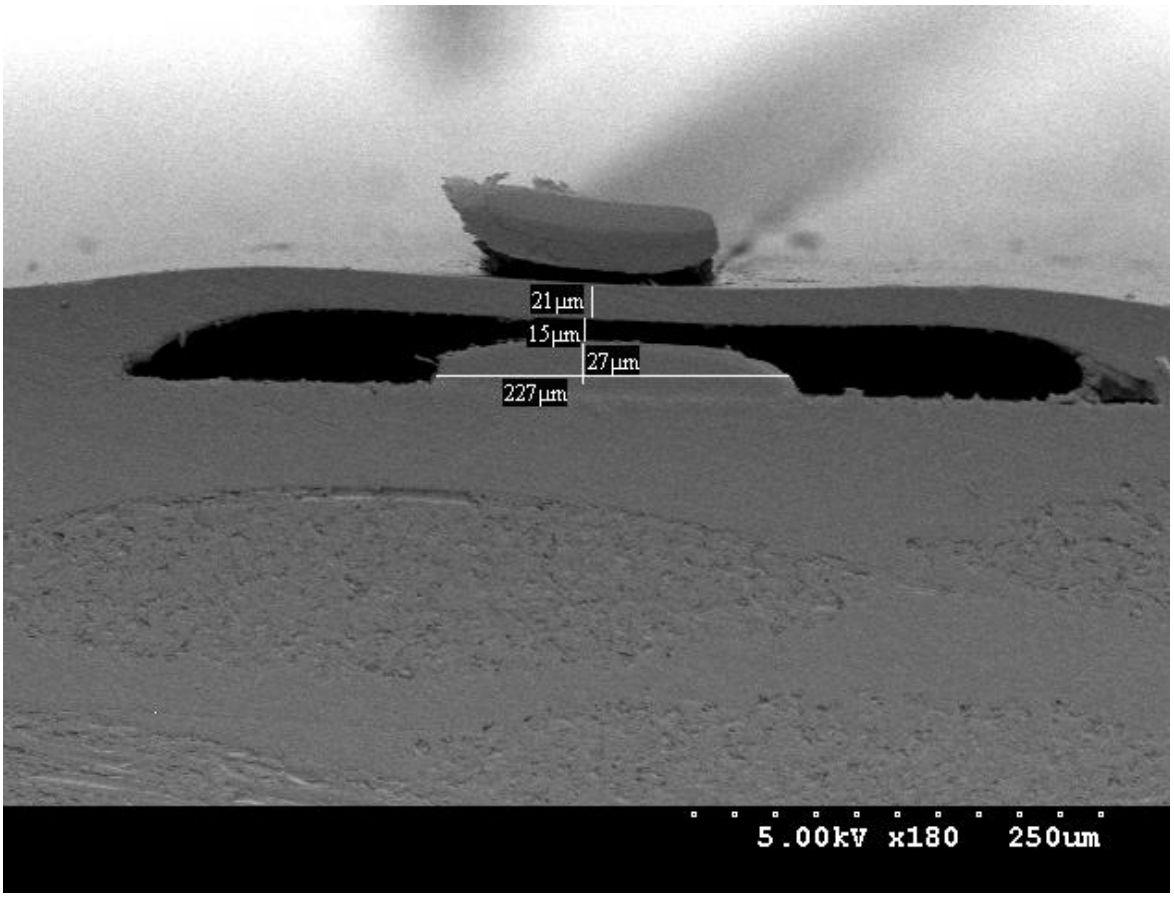

Figure 3.4 SEM of the narrow width ground line. The 150 µm wide ground line is peeled back due to delamination during the dicing process. Slight residue is seen in the right corner of the air cavity but is not expected to impact electrical performance.

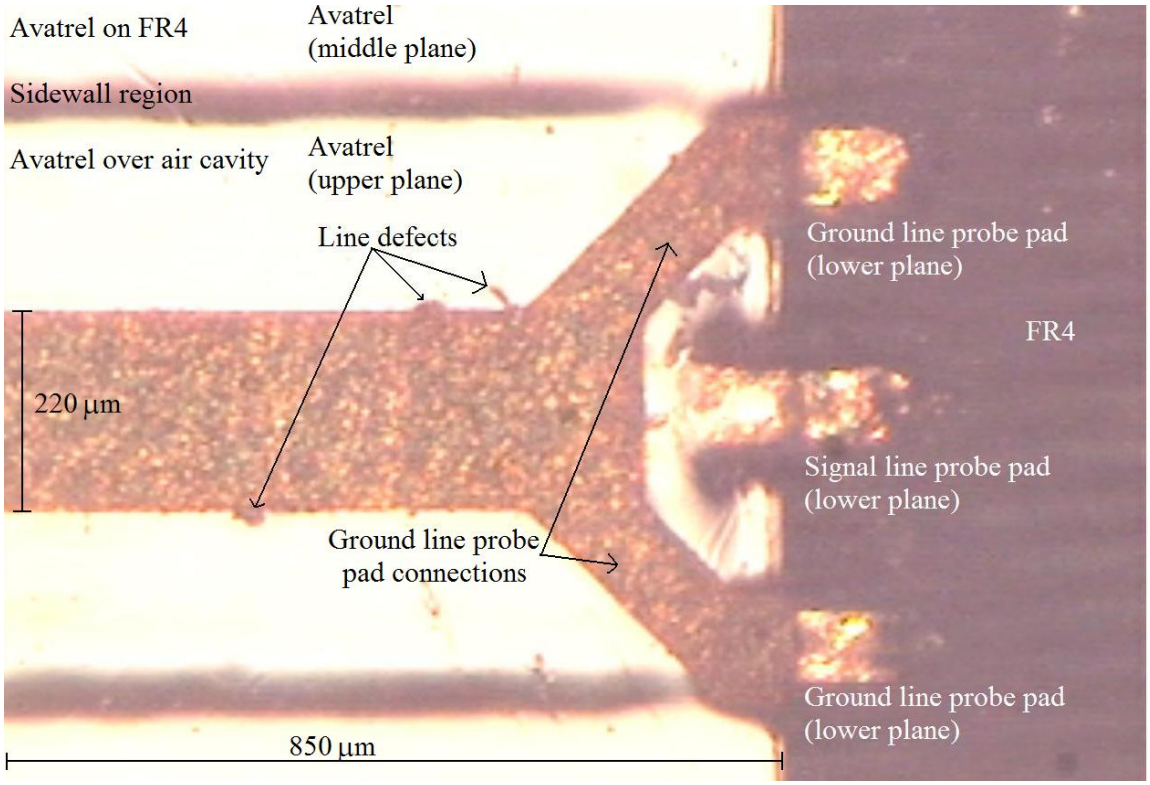

Figure 3.5 Top view of parallel plate structure probe pads

3.5. Capacitance and Loss Tangent Reduction

The structures were characterized at low frequency using an HP4263A LCR meter to measure capacitance and loss tangent at 10 kHz and 100 kHz. Measurements were taken before and after decomposition of the sacrificial polymer. The capacitance of the structures was simulated using a 2-D electrostatic field simulator. The material properties used in the simulation are listed in Table 3.1.

Material	ε_r	tan δ	thickness (μm)
FR4	3.9	.015	1000
Signal Cu	-	-	27
Unity	2.28	.004	15[a]
Air	1.0006	-	15[a]
Avatrel	2.5	.009	20
Ground Cu	-	-	24

Table 3.1 Material properties used in simulations

3.5.1. LCR meter calibration

The LCR meter was calibrated according to the manufacturer's instructions by performing open, short, and cable corrections. Probe needles were first separated by several centimeters to perform the open correction and then touched together to perform the short correction. The LCR meter also enabled accounting for effects of the 1 meter cables. The structures were then probed from one end by first lowering one probe needle onto the ground probe pad and then lowering the other onto the pad for the signal line. No change in measured results was observed when the probe needle positions were reversed. For capacitance measurements, the LCR meter has an error of +/-0.1 pF.

3.5.2. Capacitance measurements

Summarized in Table 3.2 are the measured values of capacitance before and after decomposition of the sacrificial polymer. The formation of the air-gap resulted in a reduction of capacitance of 27 to 44 percent at 10 kHz. Results at 100 kHz were slightly less capacitive (measurements were between 0.1 and 0.2 pF lower than 10kHz). The capacitance reduction is consistent with the reduction in effective dielectric expected from Equation 3.5. The simulated values of capacitance are somewhat higher than measured results, although air-gap inclusion results in a similar capacitance reduction. Better agreement between simulated and measured result is possible by accounting for topographical features. Simulated capacitance does not include probe pad effects and treats the line as having uniform dimensions along the 58 mm line. An air-gap parallel plate structure has a capacitance 39 percent lower than an equivalent thickness of Avatrel (which has a capacitance of 9.69 pF) and 60 percent lower than an equivalent thickness of FR-4 (which has a capacitance of 14.77 pF).

Ground Line Width (μm)	Capacitance before Unity decomposition (pF)	Capacitance after Unity decomposition (pF)	% Reduction
650 (simulated)	*9.64*	*6.26*	*35*
650 (measured)	8.63	4.86	44
	9.19	5.35	42
220 (simulated)	*8.89*	*5.93*	*33*
220 (measured)	7.95	5.02	37
	7.96	5.29	34
	7.67	5.00	35
150 (simulated)	*7.44*	*5.11*	*31*
150 (measured)	5.37	3.89	28

Table 3.2 Capacitance measurements before and after Unity decomposition

The variance observed in the measured capacitance results for similar lines are likely due to processing defects. Edge effects were particularly important for the 650 μm wide ground line due to the inability to process larger board sizes. The three measured lines with 150 μm wide ground planes have very little variance between them. It is expected that in a manufacturing environment, this variance could be further reduced.

3.5.3. Loss tangent measurements

The measured values of the loss tangent for these structures are shown in Table 3.3. The loss tangent was read directly from the LCR meter simultaneously with the capacitance measurement. The inclusion of the air-gap significantly reduced the dissipation factor of the lines. A loss tangent reduction of greater than 85 percent was observed for each of the structures. The reduced capacitance and loss tangent values verify the presence of the air-gap.

Ground Line Width (μm)	tan δ before Unity Decomposition	tan δ after Unity Decomposition	% Reduction
650	0.0260	0.0031	88
	0.0211	0.0029	86
220	0.0174	0.0025	85
	0.0173	0.0027	85
	0.0171	0.0026	85
	0.0170	0.0023	87
150	0.0190	0.0025	87
	0.0187	0.0026	86
	0.0188	0.0029	85

Table 3.3 Loss tangent measurements before and after Unity decomposition

3.6. High Frequency Characteristics

The parallel plate structure was characterized at high frequency using an Agilent 8720ES S-Parameter Network Analyzer. The scattering parameters were measured from 100 MHz to 10 GHz using GSG probes with a pitch of 150 μm. Simulation of the high frequency performance of these structures was performed using the High Frequency Structure Simulator (HFSS) by Ansoft.

3.6.1. Network analyzer calibration

Prior to measurement, the network analyzer and probes were calibrated using a short, open, load, thru (SOLT) calibration. S-parameter measurements were made by placing the coplanar probe structures on the substrate surface and dragging towards probe pads until contact was made.

3.6.2. Measured and simulated S-parameters

The measured and simulated insertion loss for a parallel plate line 58 mm long are shown in Figure 3.6. Measured and simulated return loss are shown in Figure 3.7. It was not possible to de-embed these measurements due to the limitations of the research test vehicle and as a consequence, exact matching of simulated and measured values was not

possible. Other reasons for deviation from simulation may include differences in simulated and fabricated geometries, probe pad parasitics, line defects from the etching or electroplating processes, and/or calibration difficulties.

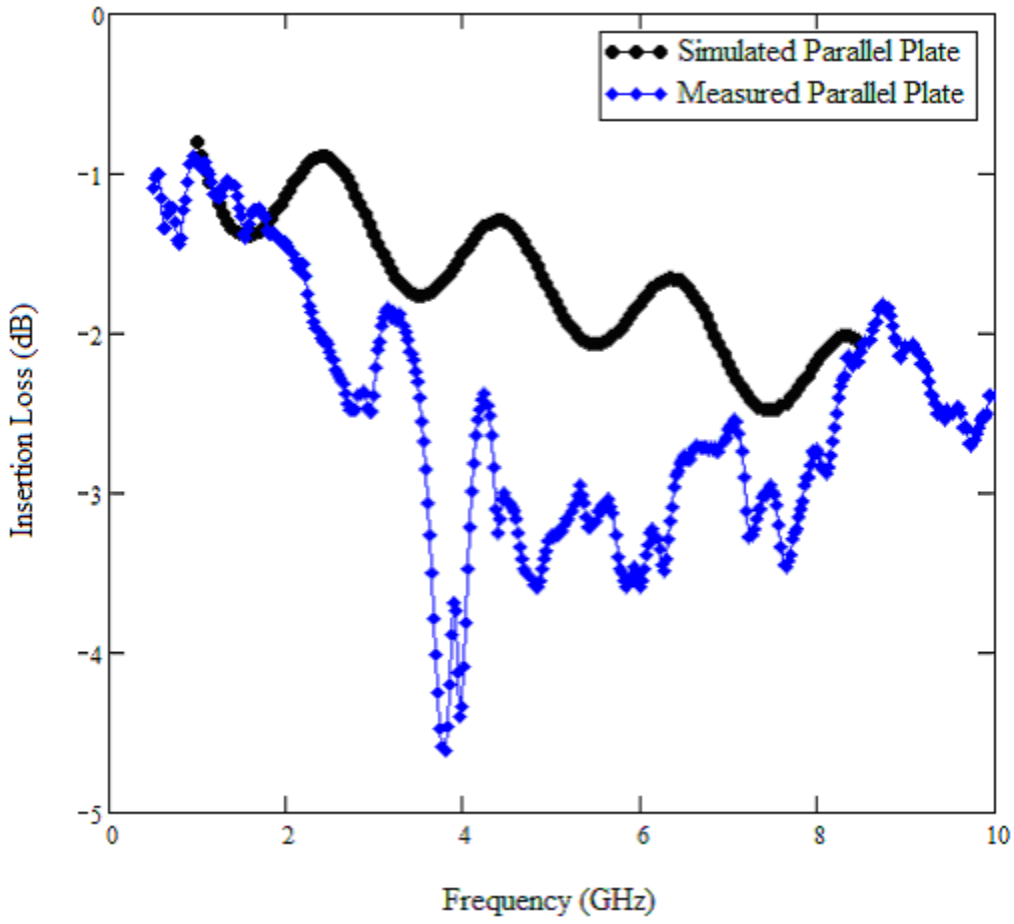

Figure 3.6 Measured and simulated insertion loss for parallel plate line

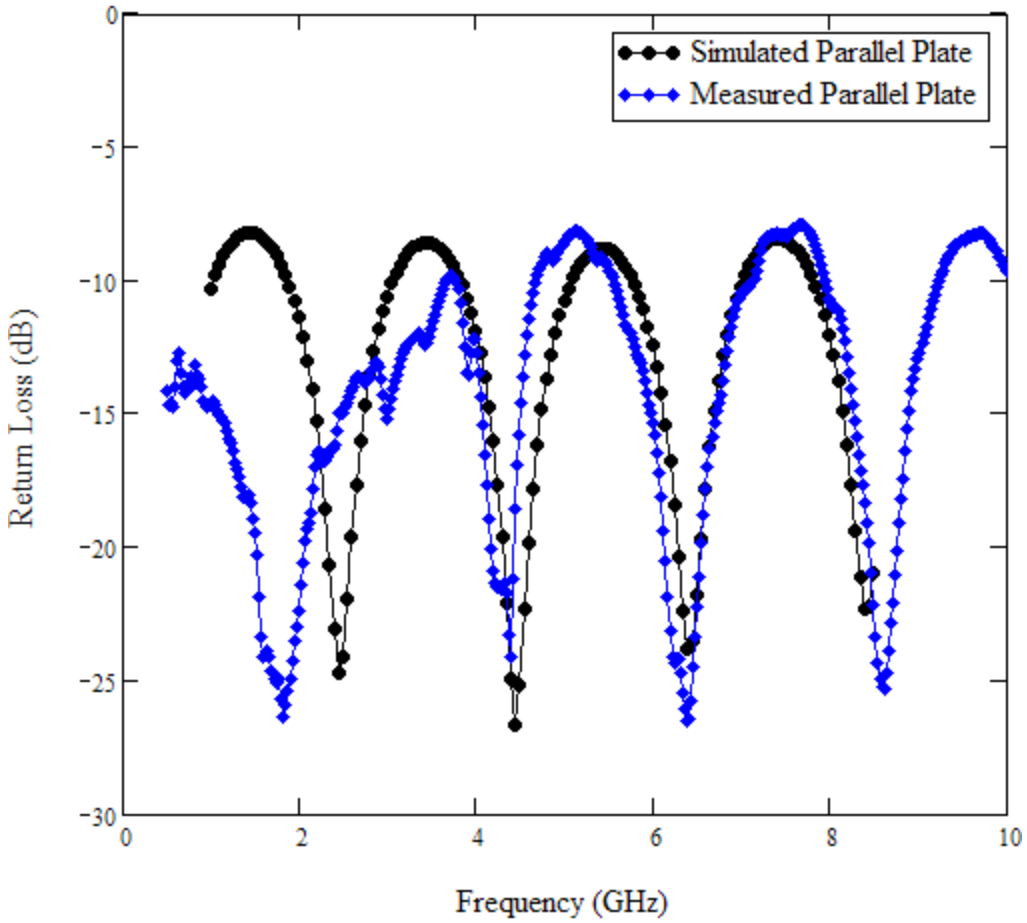

Figure 3.7 Simulated and measured return loss for parallel plate line

3.6.3. Effective dielectric constant

The effective dielectric constant was determined from the extracted phase constant and by rearranging the relation expressed in Equation 3.2. The phase constant was estimated from the measured and simulated scattering parameters using the technique described in [20]. For the parallel plate line, the extracted dielectric constant at high frequencies was approximately 1.5. The effective dielectric calculated using Equation 3.5 for an air-gap height of 15 μm and a dielectric thickness of 20 μm is 1.52.

3.6.4. Characteristic impedance

The characteristic impedance of the parallel plate line was approximately 40 Ω. This is lower than the targeted characteristic impedance of 50 Ω as a result of a thinner

overcoat film thickness over the sacrificial polymer regions. The 20 μm overcoat thickness is less than the desired thickness of 31 μm. The overcoat thickness is 31 μm over the planar regions of the board. This effect will be accounted for in future designs to achieve a characteristic impedance of 50 Ω.

3.7. Conclusions

Air-gap transmission line structures on FR-4 and BT have been demonstrated using a sacrificial polymer and CMOS compatible processing techniques. These low loss transmission line structures could be used for high frequency interchip communication with essentially zero dielectric loss and reduced conductor loss. Multilevel signaling techniques such as those described in [21] could be combined with the described low loss lines to achieve high data rates over long traces with low insertion loss.

Extensive reliability tests including thermal, mechanical, and electrical shock tests have not been performed. However, preliminary investigation demonstrated no critical failures after repeated drops from a height of 2 m. This is sensible because the forces experienced are small as a consequence of the small masses involved. Another set of lines with similar air cavity thickness (14 μm) demonstrated no change in measured capacitance after 18 months, suggesting the air-cavity is not subject to degradation due to creep. Future work will include a detailed reliability study which will include modeling of forces and stresses, including those experienced during assembly and operation.

The techniques demonstrated in the fabrication process can be extended to reduce the dielectric constant further by supporting the top conductor layer from above, adhering the bottom of the overcoat to the top of the ground conductor. Such a structure would have a dielectric constant close that of free space.

Additional transmission line structures could be fabricated in different geometries by layering air-gap structures as described in [8]. Coaxial or embedded stripline designs could be fabricated in this manner, which would provide low-loss as well as providing

good electrical shielding to prevent cross-talk between lines. These structures could be achieved using a buildup process or by entrenching the overcoat material to create a more planar structure.

The ability to form vias between layers while minimizing reflections is essential for multilayer structures. Proper design can mitigate reflections, but additional processing steps may be required to achieve this characteristic. Techniques which may simplify this process (such as nanoimprint lithography) are currently under investigation and will be included in future work. An additional benefit of imprint lithography is the ability to define smaller features in the sacrificial polymer.

Detailed investigation of electrical performance of different structure geometries including simulated eye diagrams will be included in a future study. Comparisons will be made between embedded stripline designs and parallel plate and suspended ground microstrip lines. The electrical characteristics of vias as well as coupling between lines will also be addressed.

4. DECOMPOSITION OF POLY(PROPYLENE CARBONATE) WITH UV SENSITIVE IODONIUM SALTS

4.1. Overview

In this chapter, the thermal decomposition behavior of solvent-cast PPC is evaluated using dynamic thermogravimetric analysis (DTGA) and compared with pure species decomposition properties. PPC from two sources with different molecular weights and different impurities were compared. The effect of nitrogen and air environments in the PPC decomposition chamber was studied. The influence of casting solvent on decomposition behavior has been evaluated using six polar solvents. Acid catalyzed decomposition of the PPC film was evaluated using triflic acid and UV-sensitive photo-acid generators (PAG).

The thermal decomposition data as a function of temperature and time was analyzed using Flynn-Wall-Ozawa and Coats-Redfern methods to extract values for the activation energy and pre-exponential factor. These kinetic parameters are important for predictive modeling of air cavity formation and designing controlled decomposition recipes[22]. With a sufficient amount of photoacid loading, decomposition proceeds at reduced temperatures via chain unzipping. The acid is created upon ultraviolet (UV) irradiation of the PAG. Without irradiation of the PAG or samples without acid loading, the PPC decomposed at temperatures above 180°C. Residue from the non-volatile component of the PAG salts was found to be proportional to the initial PAG concentration in the PPC. Low concentrations of PAG showed anomalously slower decomposition rates after UV exposure and resulting in higher final decomposition temperatures due to foaming of the sample during decomposition.

4.2. Introduction

Poly(propylene carbonate) (PPC) is a soft aliphatic thermoplastic formed by the copolymerization of propylene oxide and carbon dioxide, as first reported by Inoue *et al*[23]. The glass transition temperature of PPC is near room temperature ($T_g \approx 25°C$ to 45°C) [24-25] and depends on molecular weight and backbone structural arrangement[26]. PPC has a relatively low decomposition temperature, with the five percent mass loss ($T_{d\text{-}5\%}$) widely reported to be approximately 180°C[27]. This has limited its commercial applications as a replacement for conventional plastics but makes it attractive as a sacrificial material. Numerous efforts have been made to increase the thermal stability and mechanical properties of PPC [25, 27-36]. Thermal decomposition in inert environments proceeds via unzipping into cyclic propylene carbonate (4-methyl-1,3-dioxolan-2-one) at lower temperatures (ca. 180 °C) followed by random chain scission at higher temperatures (ca. 250°C)[37]. The decomposition mechanism depends on molecular weight[25], temperature, ambient gaseous environment[38-39], and additives [37]. Techniques to increase the thermal stability have been reported [27-28, 33-35]. Methods to lower the decomposition temperature for use as a sacrificial material has also been reported [6, 8, 40-41].

4.2.1. PPC as a sacrificial material

The low decomposition temperature and volatile products make PPC an ideal sacrificial material for microelectronic applications which are constrained to temperatures between ca. 100°C and 250°C. This is well within the stability range of epoxy-based products. Gaseous cavities can be created by forming spatial PPC patterns followed by overcoating with a dielectric material. The PPC decomposition products can diffuse

through the overcoat leaving an embedded gas cavity within the overcoat whose shape is determined by the original shape of the PPC pattern. Embedded cavities are potentially valuable in the packaging of microchips and microelectromechanical systems (MEMS).

4.2.2. Sacrificial PPC applications

Air cavities or other gas-filled spaces are valuable in a variety of semiconductor manufacturing and microchip packaging technologies including microfluidic channels for microprocessor cooling[42], lab-on-a-chip applications[43], air-insulated electrical signal lines[44], and vacuum packaging of MEMS resonators[45]. Air cavities surrounding a core waveguide in fiber optical cables have shown low losses[46]. Similar low losses were demonstrated in porous fiber structures with subwavelength holes[47]. Thermally decomposed PPC loaded with aluminum nitride particles has been studied for use in tape automated bonding[39, 48].

4.2.3. Acid catalyzed decomposition

A variety of polycarbonates including PPC [6, 8, 40] and polynorbornene formulations [49], have been previously studied for use as sacrificial materials. Air-cavities in a variety of dimensions have been reported using polynorbornene [44] and SiO_2 overcoats [30]. A small quantity of a photoacid generator (PAG), which creates a catalytic amount of an acid upon exposure to ultraviolet (UV) radiation, reduces the decomposition temperature, enabling direct photopatterning of the material without the need for a hardmask [8]. Small amounts of residue were observed in the cavities following decomposition [8, 44-45]. Improved decomposition was reported by using a combination of PAGs generating acids with different vapor pressures[40].

4.3. Background

Poly(propylene carbonate) is synthesized via copolymerization of propylene oxide and carbon dioxide in the presence of a catalyst at elevated pressures. The primary backbone component is propylene carbonate as shown in Figure 4.1. Impurities, especially ether linkages are present in the backbone as an undesired by-product of the synthesis, at typically less than 10 mole percent.

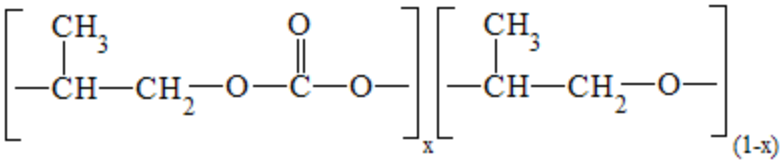

Figure 4.1 Backbone structure of poly(propylene carbonate) (PPC).

Molecular weights are typically on the order of 10^4 to 10^5 g/mol [50] and yield of the alternating co-polymer is highly dependent on catalyst and cocatalyst selection. Increased polyether content depresses the glass transition temperature by as much as 30°C while the thermal stability increases with increasing number of ether linkages.

4.3.1. Backbone structure

Depending on polymerization conditions, catalyst, and cocatalyst, the local structure of backbone components varies, affecting thermal stability and mechanical properties. Ring opening of propylene oxide may occur at either the α or β-positions. The α-site mechanism opens the bond between the oxygen atom and the center carbon (CH group) of the propylene unit whereas the β-site mechanism opens the bond between the oxygen and the CH_2 group in the ring. Thus, the methyl group can be on the alpha or beta carbon with respect to the oxygen in the ring-opened propylene oxide and polymer structure depends on which ring-opening position dominates. The regiostructure of PPC

can exist in three different configurations as shown in Figure 4.2 Backbone structure configurations of PPC. It should be noted that Head-to-Head and Tail-to-Tail configurations are effectively the same monomer unit and cannot exist in exclusively one configuration. The Head-to-Tail configuration can exist solely as members of these other configurations.. These configurations have been termed head-to-head (HH), tail-to-tail (TT), and head-to-tail (HT) configurations. An important feature of the HH and TT configurations is they coexist with each other in alternating units or with chains of head-to-tail configurations. Poly(propylene carbonate) cannot exist exclusively of HH or TT configurations because they must be coupled with another configuration. PPC made from units in the head-to-tail arrangement, however, can exist solely in this configuration.

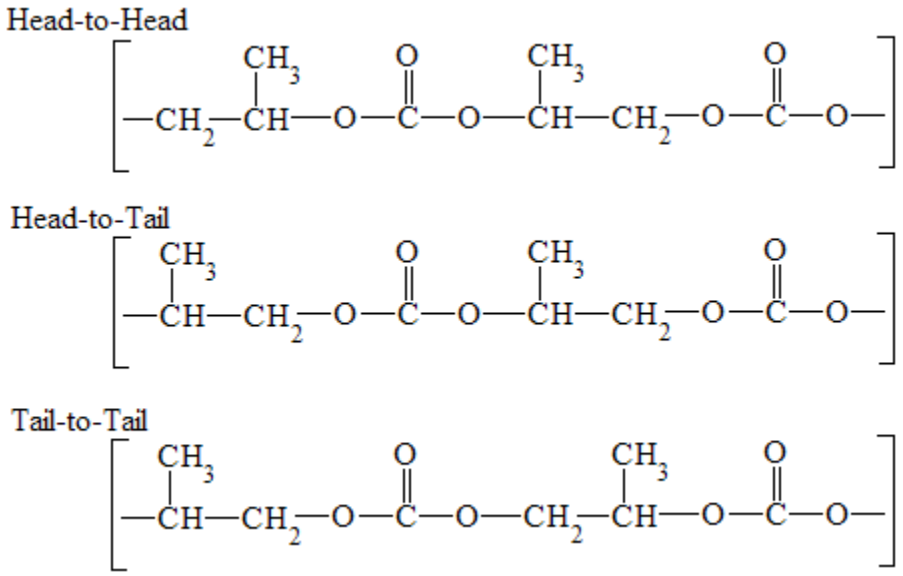

Figure 4.2 Backbone structure configurations of PPC. It should be noted that Head-to-Head and Tail-to-Tail configurations are effectively the same monomer unit and cannot exist in exclusively one configuration. The Head-to-Tail configuration can exist solely as members of these other configurations.

4.3.2. Synthesis and catalysts

Choice of catalyst is important in order to minimize the ether linkages, maximize yield of the alternating copolymer, and residual catalyst may influence decomposition.

Common catalysts used in PPC polymerization include heterogeneous zinc compounds, aluminum porphyrins, Co^{III}(salen), Cr^{III}(salen). High co-polymer yield results in fewer ether linkages but increases susceptibility to decomposition via chain unzipping. The unzipping mechanism occurs in highly regular PPC because terminal alcohols allow the cyclic monomer to form and detach from the backbone. Because the endgroup remains terminated with an alcohol, the cyclization continues and the backbone of the polymer unzips.

Molecular weights as low as 13,000 g/mol [51] and as high as 144,600 g/mol [37] have been synthesized in the presence of zinc glutarate, zinc-cobalt and zinc-nickel complexes [52]. Higher molecular weights are difficult to synthesize due to spontaneous depolymerization into the more thermodynamically stable cyclic propylene carbonate, especially at elevated temperatures[26], although 176,000 g/mol PPC was reported using allyl glycidyl ether as a cross-linker [53]. Catalyst and cocatalyst determine regio-structure of high molecular weight PPC with cationic initiators opening propylene oxide at both α- and β-positions, while anionic initiators, coordination initiators, and Lewis base cocatalysts open the epoxide ring primarily in the α-position. Ring opening at the α-position gives a more regular structure with an increased number of HT linkages and reduced ether linkages [26, 54-55]. Co-polymer yield can be improved by vacuum activation of the catalyst prior to polymerization [25].

Residual catalyst may impact thermal stability since removal of catalyst has been suggested to increase thermal stability by inhibiting chain scission [37]. The choice of solvent for use in catalyst recovery may also influence thermal stability. Removal of catalyst after polymerization is performed by precipitation in chlorinated solvents,

typically chloroform [29-30, 37, 56] or dichloromethane [26, 53-54, 57-58] and quenching with dilute hydrochloric acid in methanol. Acetone has also been reported for purification/catalyst precipitation [36]. Other studies have suggested residual catalyst does not alter thermal stability.

4.3.3. Mechanical properties of PPC with impurities

The mechanical properties of PPC were not evaluated here but are important for sacrificial material patterning via photopatterning and imprint lithography. Small weight percentages of PAGs used in this study and residual solvents are not expected to change mechanical properties significantly from the bulk. However, these properties will be influenced by polyether content, molecular weight, and region-structure. Chemical foaming in the presence of low quantities of PAG.

The backbone structure and influence of additives have been the subject of numerous other studies[24, 28-31, 59-66] and depend on polyether content [24, 62] and backbone structure[26]. Glass transition temperatures of the alternating co-polymer are between 35°C and 40°C, but are as low as 8°C with greater polyether content. Increasing molecular weight with more HT units increases the glass transition temperature to 45°C and improves tensile and compressive strength [26]. Tensile strength of the alternating copolymer is reported in the range of 22 MPa [28, 32, 67] and 32 MPa [29-30, 62], but may be as low as 8 MPa [63, 65, 68].

The influence of small quantitites of additives (less than 10 wt%) on mechanical properties have not been widely reported. Weight percentages of octadecanoic acid of 0.28% to 2.27% showed a slight increase in glass transition temperature. Other hydrogen-bonded complexes including clay nanoparticles reported an increase in shear

modulus and viscosity at 2.5 wt% loading [35]. Glass transition temperature, tensile strength, and Young's modulus increased at loadings between 1 wt% and 10 wt% [28, 65]. Chemical foaming [61, 69] will change mechanical properties from that of the bulk polymer due to porosity. Blends with poly(butylene succinate) [70], poly(3-hydroxybutyrate) [66], poly(lactic acid) [71], and glycerol starch [68] increased storage modulus and tensile strength linearly with additive concentration. Terpolymerization with bisphenol-A [67], cyclohexene carbonate [24, 62], (2-napthyloxy)methyl oxirane [30], and N-(2,3-epoxyl-propyl)carbazole [29] raised tensile strength and glass transition temperature while maleic anhydride decreased tensile strength.

4.3.4. Thermal degradation

The low degradation temperature of PPC has also limited broad commercial adoption. The onset of degradation is widely reported as the temperature where 5 percent weight loss occurs ($T_{d\text{-}5\%}$) and is highly dependent on heating rate. Isothermal decomposition and slow heating rates (< 5°C/min) were used to obtain a degradation temperature as low as 180°C, whereas studies using faster heating rates (10°C/min to 25°C/min) reported degradation temperatures above 240 °C [6, 8, 25, 27-28, 30, 32, 34-35, 37, 51, 54, 60, 62-63, 65, 68, 70, 72]. Higher decomposition temperature reported using faster heating rates are an artifact of the measurement technique. Isothermal degradation in these studies likely occurs near 180°C.

The decomposition mechanism of the backbone depends on decomposition environment, molecular weight of the polymer, number of ether linkages, and backbone regiostructure. In oxygenated atmospheres, decomposition primarily occurs via chain scission into combustion products. In a nitrogen environment, the backbone primarily

decomposes via chain unzipping from the ends of the polymer chain or unzipping following chain scission [38-39, 48]. Higher molecular weight structures decompose almost exclusively via the chain unzipping mechanism from terminal –OH groups [25, 38]. Ether linkages inhibit chain unzipping and result in larger molecular weight decomposition fragments [8]. HT structured backbones most easily undergo decomposition via chain unzipping due to the highly regular structure. Although it is unclear which mechanism is dominant, unzipping into cyclic propylene carbonate can occur via either carbonate backbiting or alkoxide backbiting [63]. The chain unzipping mechanisms of highly regular head-to-tail PPC is illustrated in Figure 4.3. In the alkoxide backbiting mechanism, a strong nucleophile attacks the carbonyl atom, as shown from the left side (a) of Figure 4.3. In the carbonate backbiting mechanism, a weak nucleophile attacks an electrophilic carbon as shown on the right side (b) of Figure 4.3. Density functional theory (DFT) simulations suggest carbonate backbiting (b) has a lower activation energy[73]. HH and TT regiostructures inhibit this mechanism but may undergo sidegroup rearrangement to allow unzipping to proceed, albeit at a slightly lower rate.

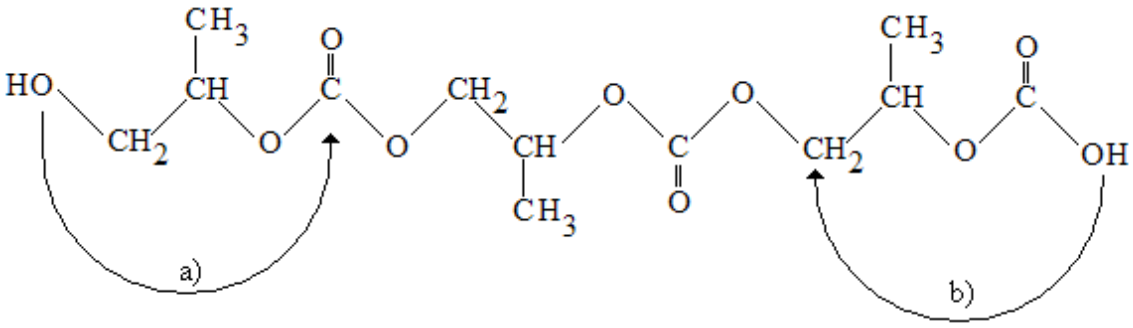

Figure 4.3 Chain unzipping in high molecular weight PPC with head-to-tail regiostructure. Unzipping can occur via a) alkoxide biting or b) carbonate biting. DFT calculations have suggested that mechanism b) is more energetically favorable.

4.3.5. Techniques to improve thermal stability

Techniques to raise the decomposition temperature of PPC include blending with inorganic and organic filler materials such as calcium carbonate [31, 69], starch [68, 74], other polymers [36, 66, 71], montmorillonite [65, 75] and organoclays[35], polymerizing with additional backbone components[24, 29-30, 32, 58, 62, 76], and end-capping of carbonate groups[27, 34] The low degradation temperature has also been exploited for use in microelectronic cooling and packaging applications [6-8, 44-45]. Acid catalyzed degradation lowered the decomposition temperature using UV sensitive PAG [8, 40-41]. Degradation in soil and buffer solution has also been reported[38].

Techniques to improve thermal stability via the addition of fillers have been modestly successful. Blends with calcium carbonate particles showed improved thermal stability with large particles, but nanoparticles actually lowered the thermal decomposition temperature. Blends of PPC with dried starch had slightly depressed decomposition onset temperatures but further decomposition was not observed until higher temperatures [68]. Residue in these blends is attributable to the filler particles.

Blending PPC with other polymers has also been attempted to improve the thermal stability. Physical blends with poly(butylene succinate) (PBS), poly(3-hydroxybutyrate), and poly(lactic acid) with carbon black elevated the onset decomposition temperature by about 50 °C at heating rates of 20 °C/min. The thermal decomposition profile for PBS blends was segmented with an initial decomposition proportional to the weight percentage of PPC and the secondary decomposition due to the PBS content [70].

End-capping of the terminal hydroxyl groups has been described as a way to increase thermal stability to inhibit the unzipping mechanism. Small quantities of maleic

anhydride, benzoyl chloride, ethyl silicate, acetic anhydride, and phosphorus oxychloride were used to delay the onset of decomposition [27]. End-capping with maleic anhydride has been evaluated as a function of backbone content relative to propylene oxide [32] and blended with ethyl cellulose [72].

Hydrogen bonding between polymer blends and additives may also stabilize PPC against thermal decomposition. The addition of octadecanoic acid at weight fractions between 0.28 wt% and 2.17 wt% demonstrated improved thermal stability [34]. Calcium stearate, a derivative of ocatdecanoic acid, also stabilized PPC by coordinating with the metal ion [33]. Hydrogen bonding has also been observed in polymer blends [36]. Low weight fractions of organic clays capable of hydrogen bonding dispersed in PPC increased thermal stability [28, 35]. Additionally, end-capping agents may be hydrolyzed in the presence of water to form hydrogen bonding structures which augment thermal stability in addition to suppression of the unzipping mechanism [27].

4.3.6. Photoacid generator (PAG) residue

Small quantities of residue remain from the decomposed photosensitive PPC formulations. X-ray photoelectron spectroscopy (XPS) results indicated the residue contained primarily fragments of the PAG [77]. Energy dispersive x-ray fluorescence (EDS) analysis confirmed the primary residue resulted from the PAG [45]. The residue may also contain higher molecular weight products from decomposition such as alkenes and ketones as observed by mass spectroscopy [8]. These products may result from dehydrogenation in the presence of acid or due to irregularities in the backbone.

4.3.7. Dynamic thermogravimetric analysis (DTGA)

Dynamic thermogravimetric analysis (DTGA) is used to assess the thermal stability of PPC by measuring mass loss as a function of temperature at a fixed heating rate. In prior studies, heating rates have been as low as 5°C/min and as high as 30°C/min. Rapid heating rates are a poor indicator of overall film stability. Slow heating rates enable clearer differentiation of decomposition characteristics.

4.3.8. Kinetic analysis of DTGA data

Thermal decomposition of solids as a function of time is described using the Arrhenius equation multiplied by an expression for the fractional decomposition, α, as shown by Equation 4.1.

$$\frac{d\alpha}{dt} = A \cdot e^{\frac{-E_a}{R \cdot T}} \cdot f(\alpha) \qquad 4.1$$

where:

A = pre-exponential factor [1/s]

E_a = activation energy [J/mol]

t = time [s]

R = ideal gas constant [8.314 J/(mol·K)]

$f(\alpha)$ can be expressed by a variety of power law or logarithmic functions. Under dynamic conditions where the sample temperature is being linearly increased at a heating rate β, Equation 4.1 can be expressed as a function of temperature as shown in Equation 4.2.

$$\frac{d\alpha}{dT} = \frac{A}{\beta} \cdot e^{\frac{-E_a}{R \cdot T}} \cdot f(\alpha) \qquad 4.2$$

where:

A = pre-exponential factor [1/s]

E_a = activation energy [J/mol]

The integrated quantity, g(α) is shown in Equation 4.3.

$$g(\alpha) = \int_0^{\alpha} \frac{d\alpha}{f(\alpha)} = \int_0^{T} \frac{A}{\beta} \cdot e^{\frac{-E_a}{R \cdot T}} \qquad 4.3$$

Numerous expressions with associated physical mechanisms have been proposed to describe thermal decomposition curves with both sigmoidal and deceleration functions. These functions can be used to describe effects of boundary conditions, diffusion limitations, and multiple nucleation sites on an individual particle [78], which are not as relevant here.

4.3.8.1. Kissinger Method

The ASTM standard technique for dynamic thermal decomposition analysis uses the method of Kissinger, which adopts Equation 4.3 and defines $f(\alpha)=(1-\alpha)^n$, where n is the reaction order . Thus, Equation 4.3 can be rearranged into

$$\ln\left(\frac{\beta}{T_{max}^2}\right) = \ln\left(\frac{A \cdot R}{E_a}\right) + \ln\left(n(1-\alpha_{max})^{n-1}\right) - \frac{E_a}{R \cdot T_{max}} \qquad 4.4$$

where T_{max} is the temperature at the maximum decomposition rate (inflection point in dynamic TGA curve) and α_{max} is the degree of conversion at the inflection point. For a first order reaction (n=1) [79-81], Equation 4.4 reduces to Equation 4.5.

$$\ln\left(\frac{\beta}{T_{max}^2}\right) = \ln\left(\frac{A \cdot R}{E_a}\right) - \frac{E_a}{R \cdot T_{max}} \qquad 4.5$$

By plotting the left side of Equation 4.5 versus $1/T_{max}$ and performing a linear regression analysis, the slope and intercept can be used to determine the activation energy and pre-exponential factor, respectively.

4.3.8.2. Coats-Redfern Method

The Coats-Redfern method of analysis offers an advantage over other techniques because a single data set is needed instead of multiple heating rates, as required by the Kissinger and Ozawa methods. The Coats-Redfern method is expressed in Equation 4.6.

$$\ln\left(\frac{g(\alpha)}{\mathrm{T}_{\max}^2}\right) = \ln\left(\frac{A\cdot R}{\beta\cdot \mathrm{E_a}}\right)\left(1-\frac{2\cdot R\cdot \overline{T}}{E_a}\right) - \frac{E_a}{R\cdot T_{\max}} \qquad 4.6$$

The algebraic expression $g(\alpha)$ depends on the physical mechanism of decomposition [51]. For a first order reaction with a single nucleation site on an individual particle, $g(\alpha)=-\ln(1-\alpha)$ and Equation 4.6 and is expressed in Equation 4.7.

$$\ln\left(\frac{-\ln(1-\alpha)}{\mathrm{T}^2}\right) = \ln\left(\frac{A\cdot R}{\beta\cdot \mathrm{E_a}}\right)\left(1-\frac{2\cdot R\cdot \overline{T}}{E_a}\right) - \frac{E_a}{R\cdot T} \qquad 4.7.$$

Thus, by plotting $\ln[-\ln(1-\alpha)/\mathrm{T}_{\max}^2]$ vs. -1/T, the slope and intercept can be used to determine the activation energy and pre-exponential factor. Alternatively, kinetic parameters for higher order reactions can be determined by fitting for the best regression value at various powers. First order (linear) regression of decomposition data are indicative of single reaction mechanisms, whereas non-linear plots are indicative of complex or competing reactions[27]. High molecular weight PPC at low heating rates decomposes primarily by backbone unzipping and thus first order reaction kinetics are considered here. Higher order regression has greater utility when competing mechanisms are present (i.e. unzipping vs. chain scission), but only gives a better mathematical fit of the curve and offers little insight into physical mechanisms. This analysis is not presented here because direct comparison of activation energies is impossible with this technique, but has been used in other PPC decomposition studies [6, 27].

4.4. Experimental

Poly(propylene carbonate) was obtained from QPac-Aldrich and Novomer Inc. and studied as received without purification. Solutions of polymer, PAG, and solvent were mixed for one week on a bottle roller. The films were spin-cast to 10 μm thickness on glass slides. The PPC film was soft baked at 110°C for 20 minutes to evaporate the solvent. Following solvent volatilization, film samples were removed from the glass slide using a razor blade and tweezers before being loaded into TGA weighing pans.

Films were also decomposed under glass on a hotplate to observe film decomposition with various PAG loadings. The samples were placed under glass and the chamber was purged for one hour with nitrogen. The hotplate temperature was increased at a rate of 1°C/min to a final temperature of 220°C. This provided a supplement to quantitative results and allowed for better understanding of the decomposition mechanism for different photoacid concentrations.

DTGA was performed using a Seiko TG/DTA 320 system. The TGA scale was re-zeroed for each weighing tin before every experiment. Samples between 10 mg and 15 mg were loaded onto the microbalance and the system purged for 30 minutes with nitrogen at a flowrate of 100 mL/min. Oxygen content for nitrogen purged decomposition was below 100 ppm. Samples were decomposed at heating rates of 0.5°C/min, 2°C/min, and 10°C/min. The temperature was increased from 30°C to 300°C and data were sampled at a frequency of 0.2 Hz for most studies. After decomposition, residue in the pan was observed qualitatively.

4.4.1. Casting solvents

PPC was dissolved in solvent to allow spincoating of thin films on a substrate. The primary solvent used in this study was γ-butyrolactone (GBL). Additional polar solvents including acetone, anisole, cyclohexanone, trichloroethylene, and dichloromethane were analyzed in this study. All solvents were obtained from Sigma-Aldrich. Samples dissolved in GBL were analyzed at heating rates of 0.5°C/min, 2°C/min, and 10°C/min. Experiments using different solvents were heated at 0.5°C/min for clearer differentiation of decomposition effects.

4.4.2. Photoacid generators (PAGs)

Acid catalyzed decomposition of polycarbonates has previously been reported for photopatterning of sacrificial materials [8]. In this study, triflic acid catalyzed decomposition was compared with two photo-acid generators which generate equivalent strength super-acids (i.e. entirely dissociated). The PAGs investigated in this study were the iodonium salts 4-methylphenyl[4-(1-methylethyl)phenyl] tetrakis(pentafluorophenyl) borate (referred to hereafter as Rhodorsil-FABA) and bis(4-tert-butylphenyl)iodonium tris(perfluoromethyl sulfonyl) methide (referred to hereafter as 3M-Methide). These photoacids were investigated because they had previously been identified as the most effective for acid catalyzed decomposition of PPC [77].

4.4.2.1.PAG Structure

The structure of the Rhodorsil-FABA PAG is illustrated in Figure 4.4 Photoacid generator structures; a) 4-methylphenyl[4-(1-methylethyl)phenyl] tetrakis(pentafluorophenyl) borate (Rhodorsil-FABA) b) (4-tert-butylphenyl)iodonium

tris(perfluoromethyl sulfonyl) methide (3M-Methide).a. The structure of the Methide PAG is illustrated in Figure 4.4b.

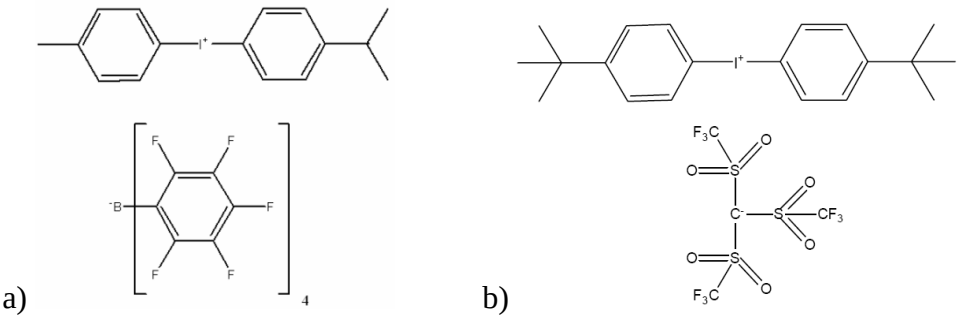

Figure 4.4 Photoacid generator structures; a) 4-methylphenyl[4-(1-methylethyl)phenyl] tetrakis(pentafluorophenyl) borate (Rhodorsil-FABA) b) (4-tert-butylphenyl)iodonium tris(perfluoromethyl sulfonyl) methide (3M-Methide).

4.4.2.2.Molecular weight and vapor pressure

Proper comparison of the PAGs requires equivalent molar acid content after UV exposure. The molecular weight of the Rhodorsil-FABA is 1016.26 g/mol and the molecular weight of the 3M-Methide is 804 g/mol. More importantly, the weight difference is primarily due to the structure of the anion, which correlates to the vapor pressure of the conjugate acid formed upon exposure to UV light. Tetrakis-pentafluorophenyl boric acid (generated by Rhodorsil-FABA) has essentially no vapor pressure at room temperature, whereas triflic acid (generated by 3M-Methide) has a vapor pressure of 8 torr at 25°C. Consequently, it is expected the Rhodorsil-FABA PAG will remain present in ever increasing concentration during decomposition, while the 3M-Methide PAG will decrease in concentration as the reaction proceeds due to evaporation.

4.4.3. Fourier transform infrared (FTIR) spectroscopy

Fourier Transform Infrared (FTIR) spectroscopy was used in an effort to identify influences of casting solvent and photoacid generators. FTIR data were collected using a Nicolet Magna IR 560 spectrometer. Data were collected in transmission mode in a nitrogen purged chamber under a nitrogen flowrate of 50 mL/min with 2 cm^{-1} resolution and averaged over 512 scans. Films were cast on a KBr disk at a thickness of approximately 1 um. Background scans of the KBr disk were performed prior to data collection for each polymer film.

4.5. Results

QPac and Novomer PPC were used as-received and decomposed in nitrogen and air environments. The heating rate for all samples was 2°C/minute. The TGA curves are shown in Figure 4.5. Kinetic parameters of activation energy (E_a) and pre-exponential factor (A) were calculated for a first order reaction using the Coats-Redfern method. These results, including the linear regression correlation value (R^2) and the decomposition completion fraction at the maximum weight loss rate (α_{max}), are listed in Table 4.1.

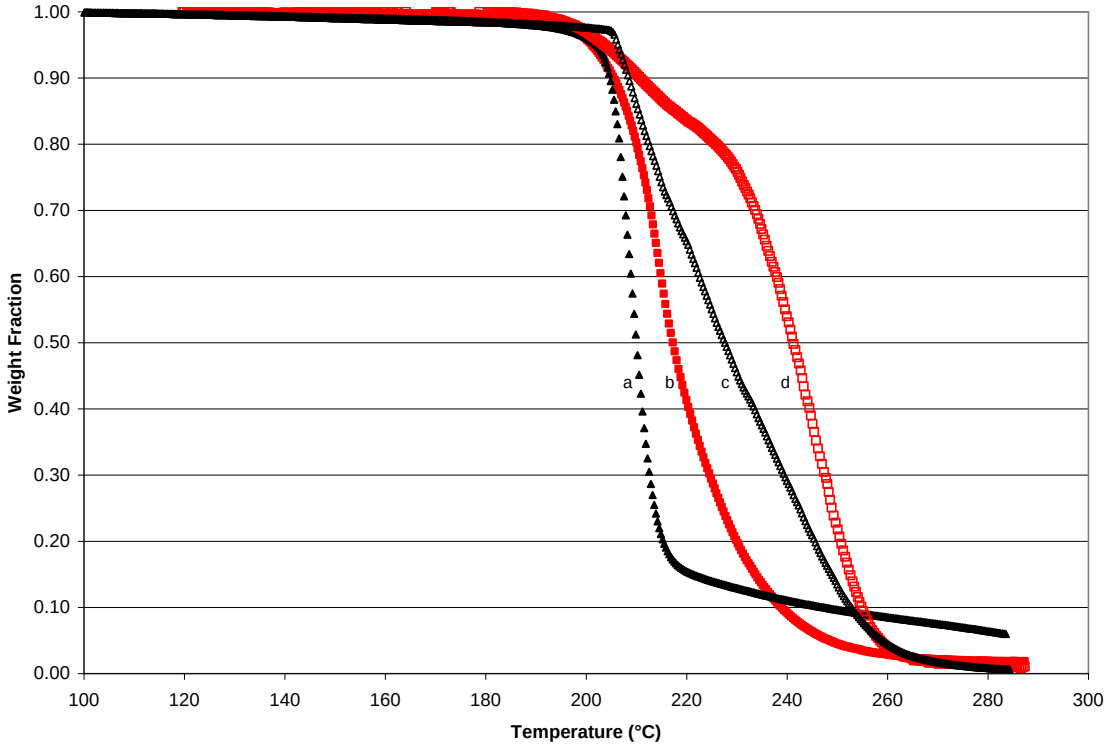

Figure 4.5 QPAC PPC in (a) air and (c) nitrogen; Novomer PPC (M_w=90,000; PD=1.5) in (b) air and (d) nitrogen.

	E_a (kJ/mol)	A (s^{-1})	R^2	α_{max}
QPAC – Air	119	7.22e5	0.9459	0.58
QPAC – Nitrogen	147	1.70e15	0.9883	0.41
Novomer – Air	120	3.21e5	0.9713	0.57
Novomer – Nitrogen	126	2.07e6	0.9569	0.48

Table 4.1 Pure species kinetic parameters calculated using Coats-Redfern technique for Air and Nitrogen environments

4.5.1. Pure PPC

QPac and Novomer PPC dissolved in γ-butyrolactone with no additional additives were spin-coated as films 10 μm thick and the solvent was evaporated by softbaking on a hotplate at 100°C. Films were decomposed in a nitrogen purged environment at heating rates of 0.5°C/min, 2°C/min, and 10°C/min. The dynamic thermogravimetric analysis plot for the QPac PPC is shown in Figure 4.6. DTGA curves of two different molecular weight PPCs of 90,000 g/mol and 100,000 g/mol from Novomer are shown in Figure 4.7

and Figure 4.8, respectively. Activation energies (E_a), pre-exponential factor, and correlation factor (R^2) obtained using the Coats-Redfern method for γ-butyrolactone dissolved blends at all heating rates are listed in Table 4.2 as well as the maximum completion fraction (α_{max}).

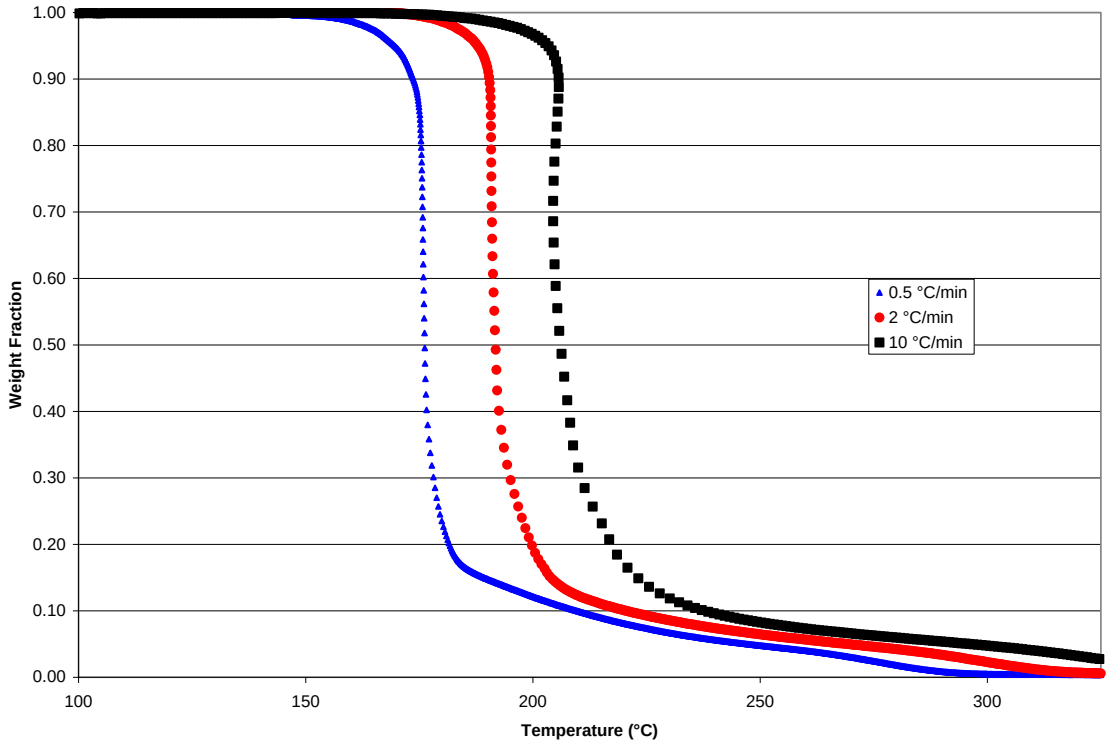

Figure 4.6 QPAC PPC dissolved in g-butyrolactone decomposed in a nitrogen purged environment at (a) 0.5°C/min, (b) 2°C/min, and (c) 10°C/min.

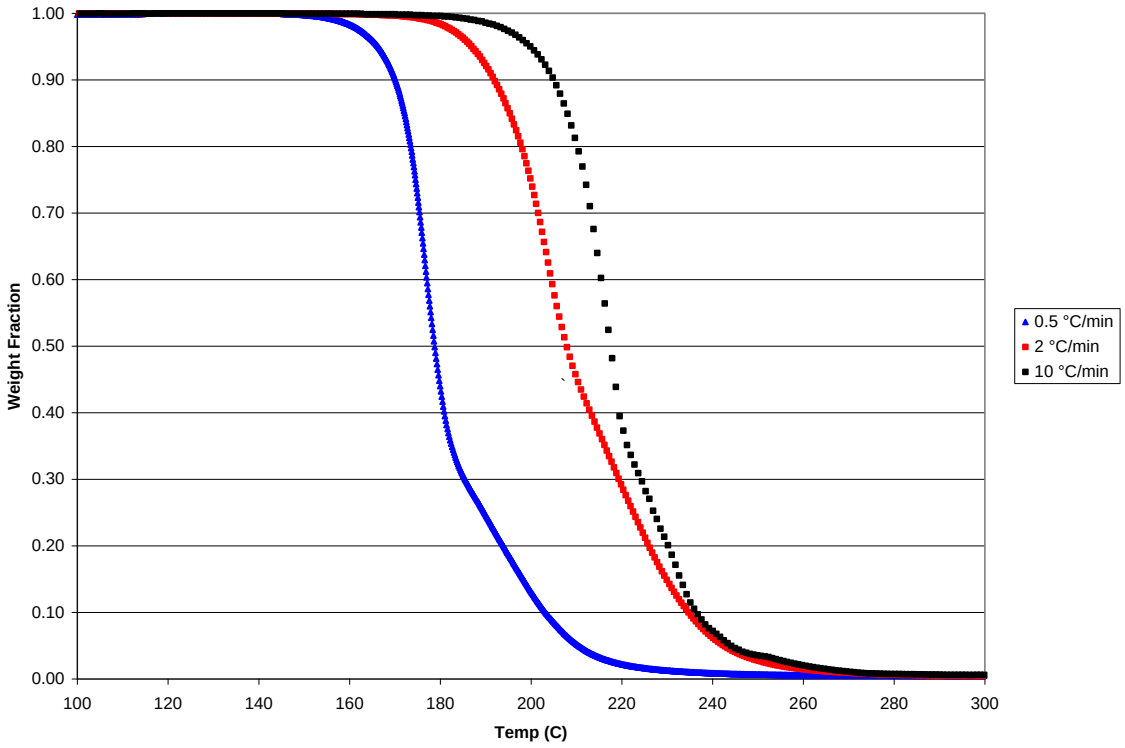

Figure 4.7 Novomer PPC (M_w=90,000; PD=1.5) in N_2 at heating rates of (a) 0.5°C/min, (b) 2°C/min, and (c) 10°C/min.

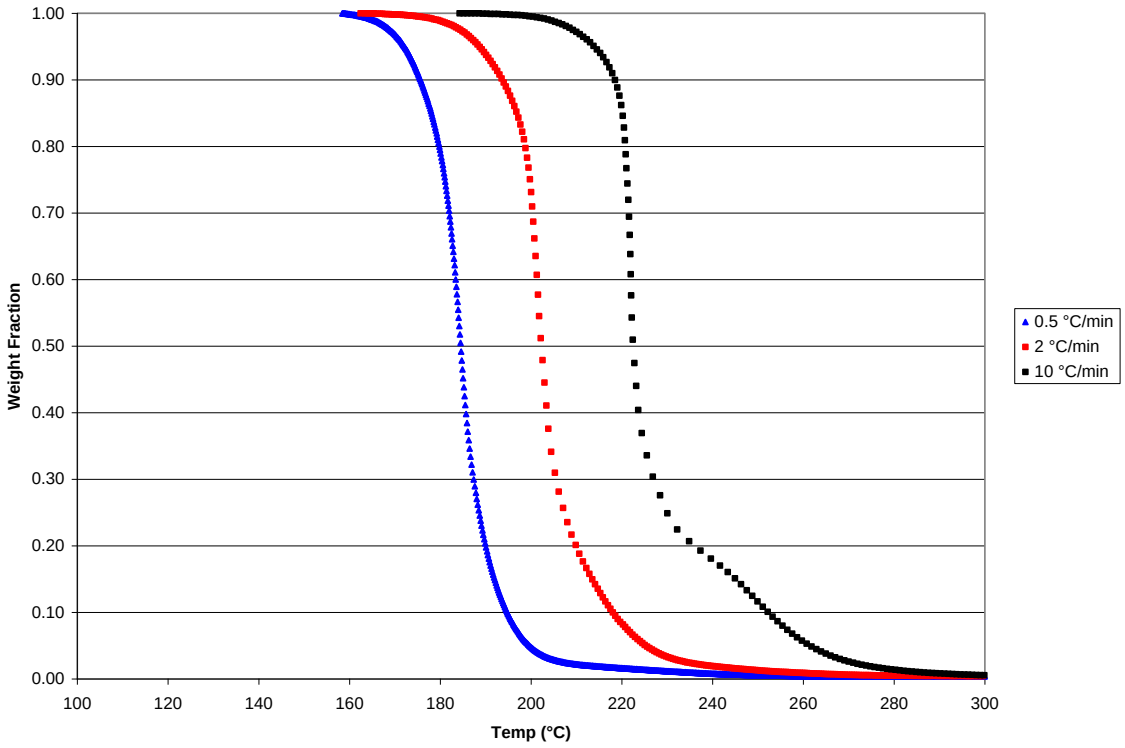

Figure 4.8 Novomer PPC (M_w=100,000; PD=1.9) in N_2 at heating rates of (a) 0.5°C/min, (b) 2°C/min, and (c) 10°C/min.

	E_a (kJ/mol)	A (s^{-1})	R^2	α_{max}
QPAC – 0.5 °C/min	285	2.66e25	0.9334	0.53
QPAC – 2 °C/min	407	1.89e39	0.9312	0.57
QPAC – 10 °C/min[a]	233	9.39e19	0.7973	0.55
Novomer 90k – 0.5 °C/min	295	5.82e26	0.9989	0.43
Novomer 90k – 2 °C/min	247	5.90e20	0.9958	0.47
Novomer 90k – 10 °C/min	234	9.36e19	0.9992	0.46
Novomer 100k – 0.5 °C/min	325	6.13e29	0.9973	0.60
Novomer 100k – 2 °C/min	288	2.11e25	0.9924	0.62
Novomer 100k – 10 °C/min	399	2.04e37	0.9515	0.60

Table 4.2 Kinetic parameters calculated using Coats-Redfern technique for PPC dissolved in γ-butyrolactone and for photoacid generators used in this study. a) The poor correlation factor for QPac heated at 10°C/min may be due to non-linear heating in the TGA (seen as a step backwards in temperature in the TGA in Figure 6) or due to the competing chain scission and unzipping mechanisms resulting from residual oxygen in the chamber.

4.5.2. Pure PAG

The two photoacid generators used in this study, (4-tert-butylphenyl)iodonium tris(perfluoromethyl sulfonyl) methide (3M-Methide) and 4-methylphenyl[4-(1-methylethyl)phenyl] tetrakis(pentafluorophenyl) borate (Rhodorsil-FABA), were heated at 0.5°C/min and decomposed at in a nitrogen purged environment. The PAGs were used in their as-received state without drying. They were examined by thermal analysis either neat or dissolved in solvent and dried in a TGA pan. The DTGA curves for these PAGs are shown in Figure 4.9. The activation energy (E_a), pre-exponential factor, and regression correlation (R^2) obtained using the Coats-Redfern method are listed in Table 4.3 with the maximum completion fraction (α_{max}).

	E_a (kJ/mol)	A (s^{-1})	R^2	α_{max}
Rhodorsil-FABA	155	1.33e13	0.9776	0.69
3M-Methide	303	5.61e30	0.9876	0.58

Table 4.3 Kinetic parameters calculated using Coats-Redfern technique for photoacid generators used in this study heated at 0.5°C/min.

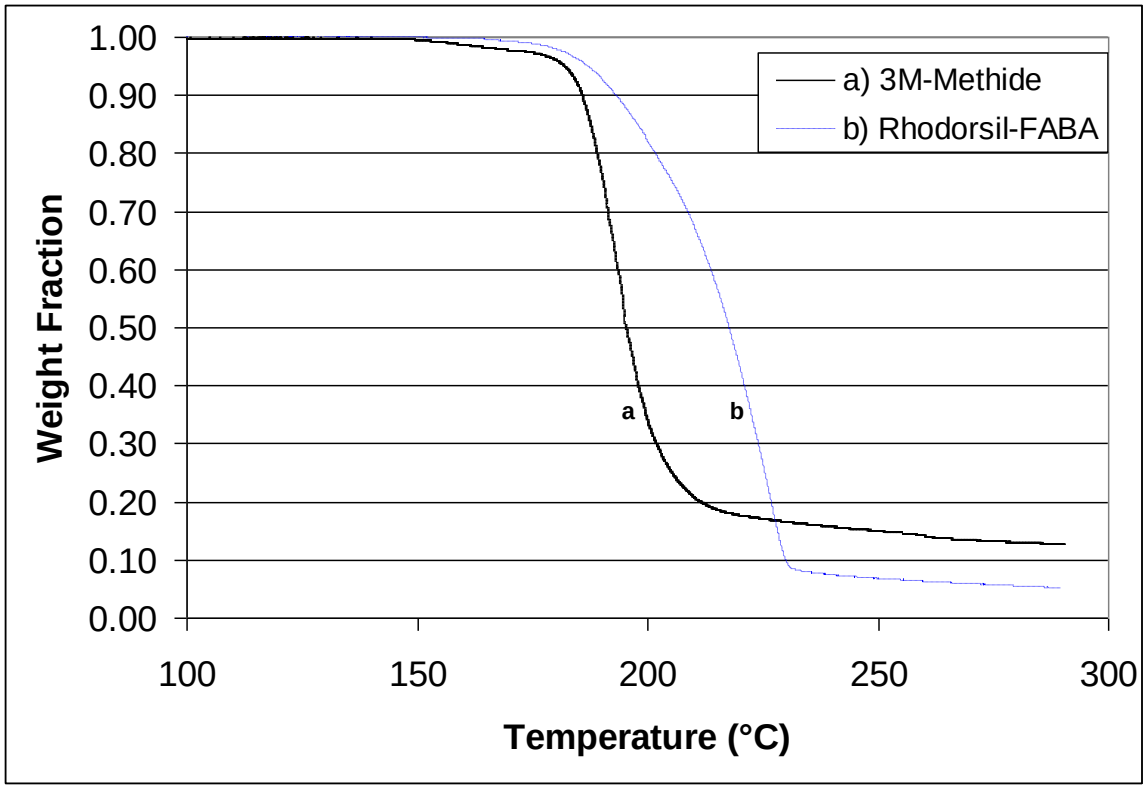

Figure 4.9 Thermal decomposition of photoacid generators in nitrogen heated at 0.5°C/min: a) (4-tert-butylphenyl)iodonium tris(perfluoromethyl sulfonyl) methide (3M-Methide); b) 4-methylphenyl[4-(1-methylethyl)phenyl] tetrakis(pentafluorophenyl) borate (Rhodorsil-FABA).

The thermal decomposition of the PAG is important because it can facilitate the acid activated decomposition mechanism of the PPC. Acid is generated upon thermal dissociation in a manner similar to UV exposure. Both PAGs exhibit five percent mass loss at temperatures near the decomposition temperature of PPC ($T_{d\text{-}5\%,Methide}$=182°C; $T_{d\text{-}5\%,\ FABA}$=187°C). The 3M-Methide PAG completely decomposes rapidly and thus may completely volatilize with little effect on PPC films while Rhodorsil-FABA does not decompose completely until 210°C, allowing the thermally generated acid to play an active role in decomposition of unexposed films.

4.5.3. PPC cast from solvent

Dissolving PPC in solvent allows control of film thickness by varying spin speed. PPC dissolves readily in numerous polar solvents including methylene chloride, anisole, acetone, γ-butyrolactone, trichloroethylene, and cyclohexanone. Novomer PPC with a molecular weight of 100,000 g/mol was dissolved in each of these solvents, spun as a 10 μm thick film, and decomposed in a nitrogen environment at a heating rate of 0.5°C/min. The DTGA curves for these films are shown in Figure 4.10. Table 4.4 shows the kinetic parameters extracted using the Coats-Redfern method. Residual solvent or interaction with PPC has a notable effect on the temperature for the onset of decomposition, as reflected in the activation energy and pre-exponential factor.

	E_a (kJ/mol)	A (s^{-1})	R^2	α_{max}
Acetone[a]	431	1.23e43	0.8621	0.72
Anisole	529	2.26e56	0.9859	0.67
γ-butyrolactone	583	4.13e21	0.9466	0.60
Trichloroethylene	457	3.87e43	0.9770	0.52
Methylene Chloride	458	4.71e43	0.9841	0.48
No Solvent Added	469	2.07e47	0.9972	0.60

Table 4.4 Kinetic parameters calculated using Coats-Redfern technique. a) The poor correlation factor for the kinetic parameters of the acetone dissolved sample is due to inversion of the curve in the middle of the decomposition range, seen as a step backwards in the TGA plot in Figure 4.10.

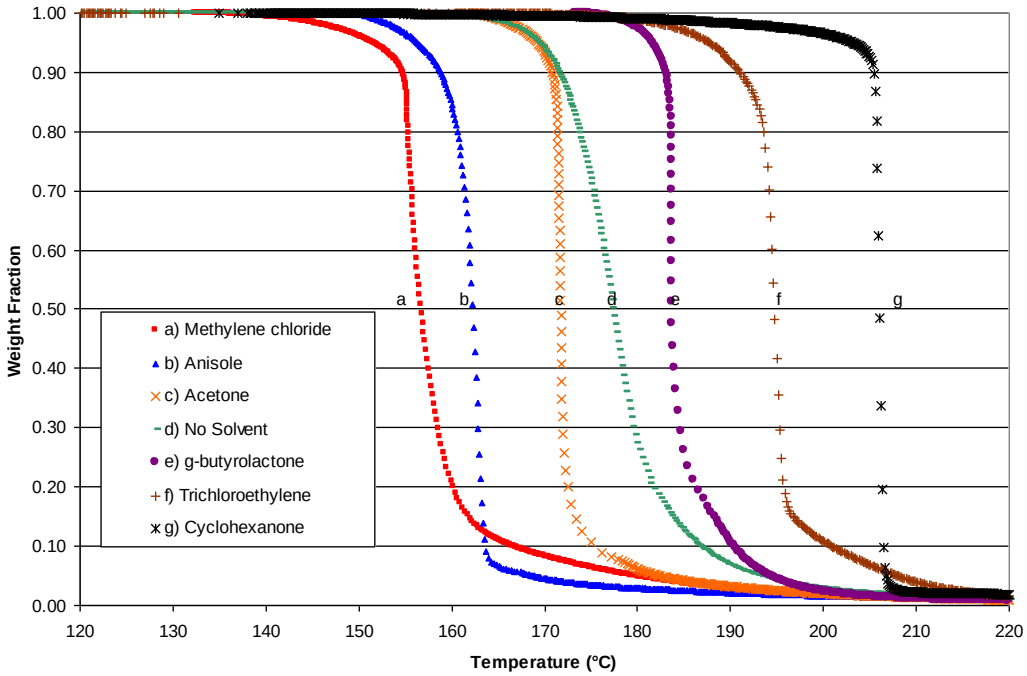

Figure 4.10 Solvent cast Novomer (MW=100k) PPC Weight Fraction vs. Temperature in nitrogen heated at 0.5°C/min compared with as received sample: (a) methylene chloride, (b) anisole, (c) acetone, (d) as-received (no solvent added), (e) γ-butyrolactone, (f) trichloroethylene, and (g) cyclohexanone.

No easily discernible trend can be seen on how the casting solvent may impact the thermal decomposition of PPC. Comparison of physical properties such as dipole moment, heat of vaporization, and boiling point show no pattern to the change in decomposition temperature. This suggests a more complex interaction between solvent and polymer backbone and may be an interaction with the terminal alcohol groups to suppress initiation or at the carbonyl sites to inhibit unzipping propagation. End-capping at the chain terminations seem most likely as this has been observed in other systems [27] where no evidence of hydrogen bonding was reported. All solvents in this study are readily hydrolyzed in the presence of water and these products may also be responsible

for end-capping of the polymer backbone. These effects may depend highly on molecular weight, polydispersity, and degree of film drying.

4.5.4. PPC containing PAG

The effects of two different photoacid generators (3M-Methide and Rhodorsil FABA) were studied by varying concentration and UV exposure. The Novomer PPC with a molecular weight of 90,000 g/mol and QPac PPC with a molecular weight of 50,000 g/mol were investigated by first dissolving the PAG in γ-butyrolactone with the polymer and mixing on a bottle roller. The photoacid concentrations by weight were 3.00 percent 3M-Methide and 3.75 percent Rhodorsil-FABA, which corresponds to an acid loading of approximately 1 mole of acid to 440 monomer units of the polymer. The average chain length of the Novomer PPC with a molecular weight of 90,000 g/mol is approximately 880 monomer units, which means there are 2 acid molecules per polymer chain. Upon UV exposure or thermal activation, the organic cation of the PAG decomposes. The remaining anion has a highly dispersed negative charge and thus generates a strong Brønsted acid. Since the acid is regenerated after each propylene carbonate decomposition, there is sufficient acid to initiate decomposition from each end of the backbone.

Ether linkages consume the acid upon decomposition by terminating the backbone with an alcohol group which does not allow polymer unzipping or acid regeneration. A lower acid concentration of 0.200 wt% 3M-Methide or 0.250 wt% Rhodorsil-FABA was also studied. This lower acid concentration corresponds to a mole ratio of 6600 monomer units per acid molecule. All UV exposures used a dose of 1 J/cm^2 at λ=248 nm.

4.5.4.1.Rhodorsil-FABA

The DTGA curves for UV exposed and unexposed films with 3.75 wt% Rhodorsil-FABA in QPac and Novomer (M.W.=90,000 g/mol) at heating rates of 0.5°C/min, 2°C/min, and 10°C/min in a nitrogen environment are shown in Figure 4.11. The UV exposed samples exhibit a low temperature, gradual decomposition while the unexposed films show a sharp decomposition at higher temperature. The shift in the decomposition temperature to lower values reflects the acid activation step. Additionally, the mass loss occurs over a broad temperature range in the exposed case, compared with a relatively narrow temperature range in the unexposed case.

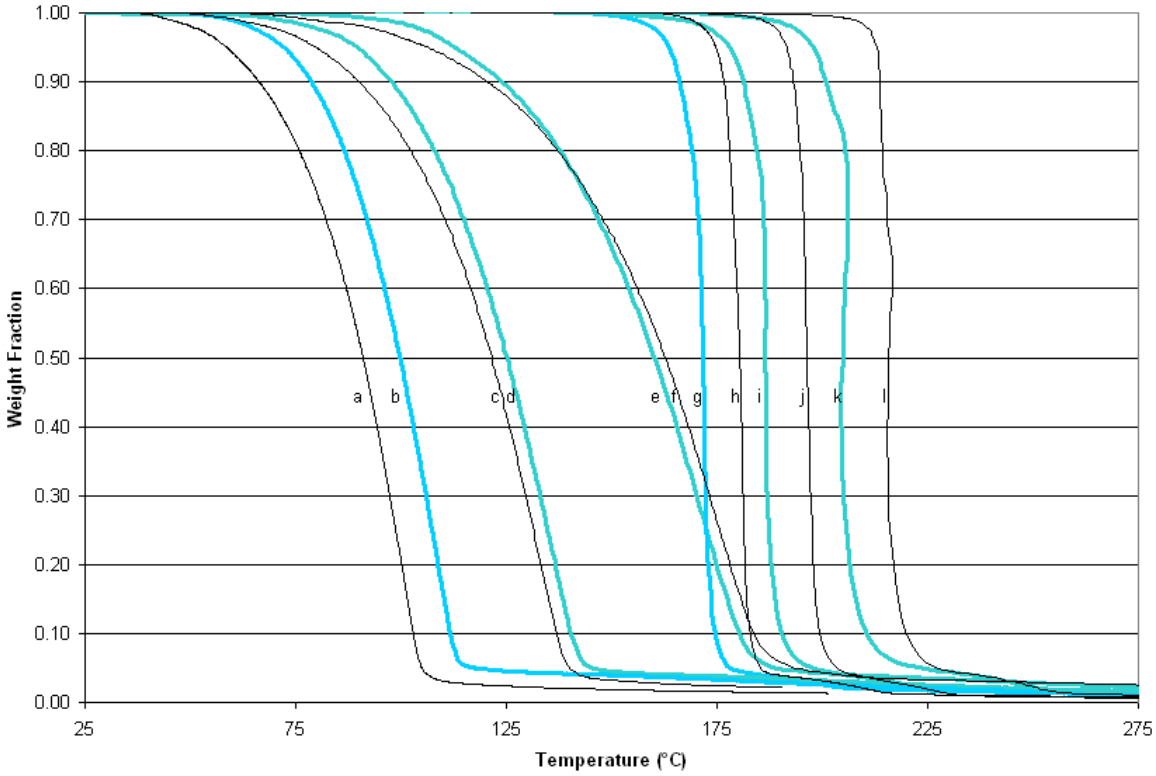

Figure 4.11 Novomer (thin black lines) and QPac (thick aqua lines) PPC with 3.75 wt% Rhodorsil-FABA PAG dissolved in γ-butyrolactone: (a),(b), (g), and (h) heated at 0. 5°C/min, (c), (d), (i), and (j) heated at 2°C/min, and (e), (f), (k), and (l) heated at 10°C/min. Curves (a)-(f) were exposed to 1 J/cm^2 of UV light at a wavelength of λ=248 nm.

4.5.4.2.3M-Methide

Decompostion of QPac and Novomer (M.W.=90,000) loaded with 3.00 wt% 3M-Methide PAG at heating rates of 0.5°C/min, 2°C/min, and 10°C/min with and without UV exposure is shown in Figure 4.12. Shown in Figure 4.13 are the low acid loading of the Rhodorsil-FABA PAG (0.25 wt%) for the exposed and unexposed cases at the heating rates listed above for QPac and Novomer (M.W.=90,000). Figure 4.14 shows the low acid loading of the 3M-Methide PAG (0.20 wt%) for QPac and 90,000 g/mol Novomer with UV exposure and without UV exposure at the same heating rates.

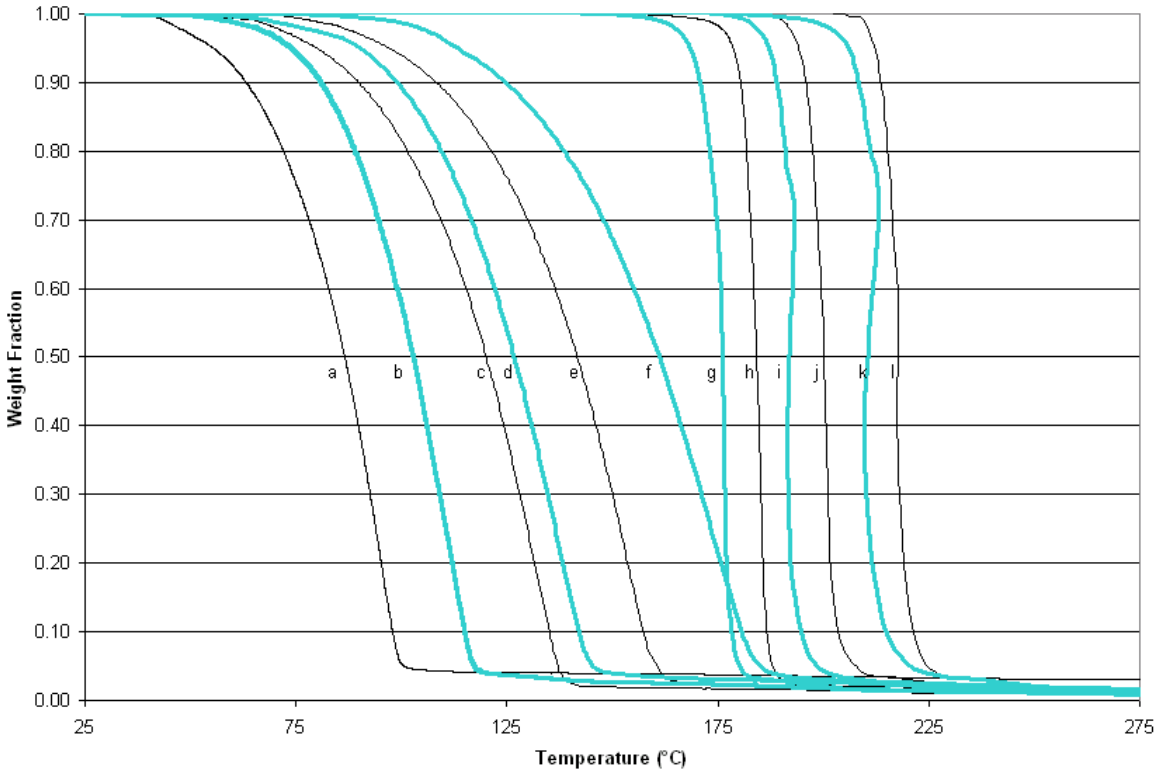

Figure 4.12 Novomer (thin black lines) and QPac (thick aqua lines) PPC with 3.0 wt% 3M-Methide PAG dissolved in γ-butyrolactone: (a), (b), (g), and (h) heated at 0. 5°C/min, (c), (d), (i), and (j) heated at 2°C/min, and (e), (f), (k), and (l) heated at 10°C/min. Curves (a)-(f) were exposed to 1 J/cm^2 of UV light at a wavelength of λ=248 nm.

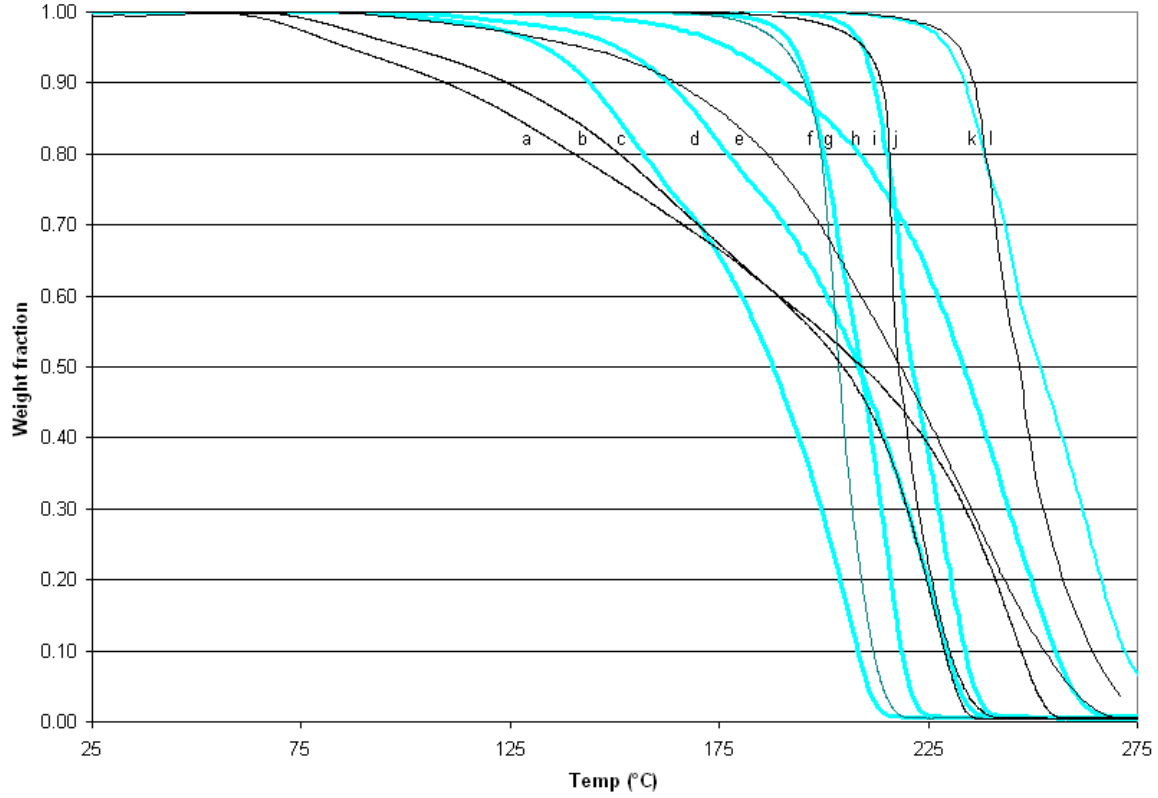

Figure 4.13 Novomer (thin black lines) and QPac (thick aqua lines) PPC with 0.25 wt% Rhodorsil-FABA PAG dissolved in γ-butyrolactone: (a), (c), (f), and (g) heated at 0. 5°C/min, (b), (d), (i), and (j) heated at 2°C/min, and (e), (h), (k), and (l) heated at 10°C/min. Curves (a)-(e) and (h) were exposed to 1 J/cm^2 of UV light at a wavelength of λ=248 nm.

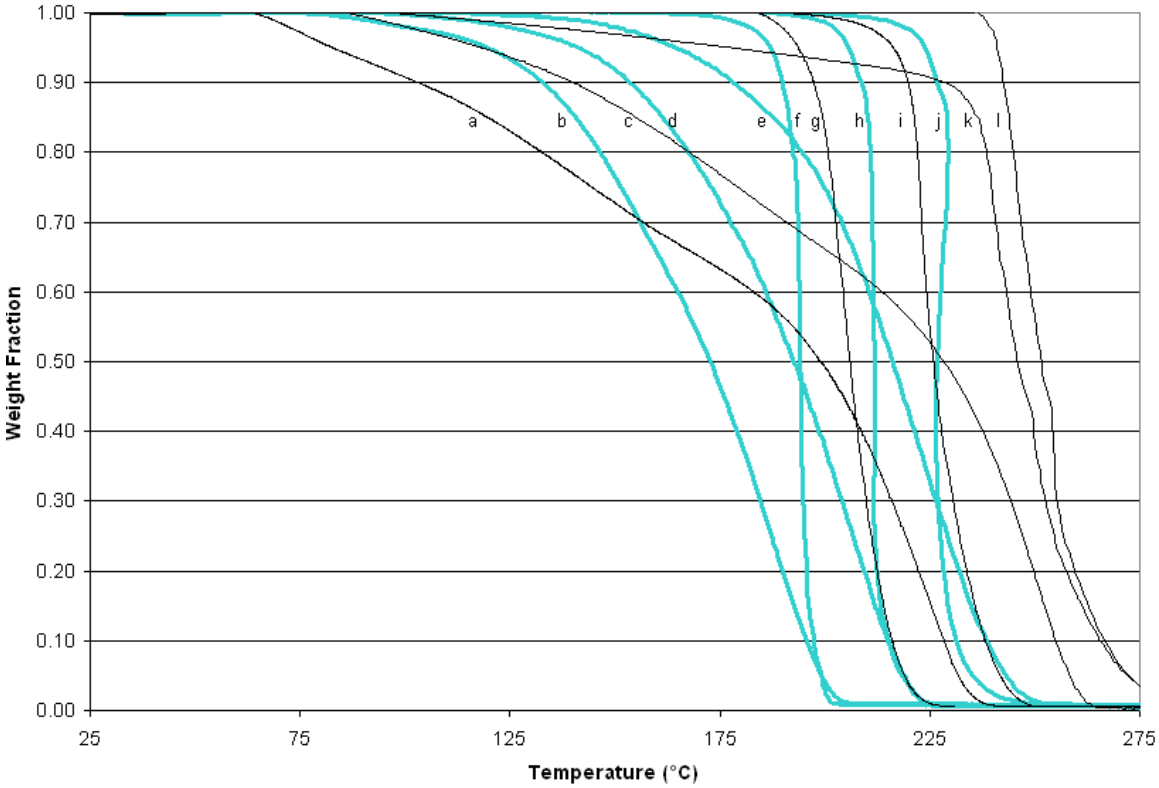

Figure 4.14 Novomer (thin black lines) and QPac (thick aqua lines) PPC with 0.20 wt% 3M-Methide PAG dissolved in γ-butyrolactone: (a), (b), (f), and (g) heated at 0. 5°C/min, (c), (d), (h), and (i) heated at 2°C/min, and (e), (j), (k), and (l) heated at 10°C/min. Curves (a)-(e) and (k) were exposed to 1 J/cm^2 of UV light at a wavelength of λ=248 nm.

4.5.4.3.Kinetic analysis

The 3M-Methide PAG had a lower decomposition onset temperature than the Rhodorsil-FABA PAG for the UV-exposed samples. Similar mass loss rates were observed in all exposed cases, consistent with a decomposition and steadily increasing rate of product loss. This is consistent with depolymerization into the cyclic monomer and a mass loss due to the evaporation of the liquid. In the unexposed cases, the films

with the FABA PAG had a slightly lower decomposition onset temperature and all samples exhibited behavior consistent with rapid decomposition and volatilization. This is consistent with depolymerization followed by immediate evaporation although chain scission may be competing. Table 4.5 summarizes the Coats-Redfern kinetic parameters for a first order reaction and completion fraction at the maximum decomposition rate (α_{max}) for the UV exposed cases for both base polymers, both photoacid concentrations of each PAG, and all heating rates. Table 4.6 lists the Coats-Redfern kinetic parameters and α_{max} for the unexposed cases of these same films.

Exposed	E_a (kJ/mol)	A (s^{-1})	R^2	α_{max}
	3.75 wt. % Rhodorsil-FABA			
QPac – 0.5 °C/min	98.2	2.90e10	0.9980	0.79
QPac – 2 °C/min	82.5	9.96e7	0.9993	0.80
QPac – 10 °C/min	76.4	9.86e6	0.9926	0.80
Novomer – 0.5 °C/min	79.7	1.12e8	0.9967	0.84
Novomer – 2 °C/min	69.4	1.85e6	0.9980	0.83
Novomer – 10 °C/min	58.4	3.89e4	0.9979	0.83
	3.00 wt. % 3M-Methide			
QPac – 0.5 °C/min	99.0	2.14e6	0.9995	0.80
QPac – 2 °C/min	83.7	3.43e4	0.9983	0.80
QPac – 10 °C/min	80.7	4.05e4	0.9951	0.84
Novomer – 0.5 °C/min	78.8	1.01e4	0.9984	0.86
Novomer – 2 °C/min	72.0	1.48e3	0.9967	0.91
Novomer – 10 °C/min	69.1	4.11e3	0.9966	0.88
	0.250 wt. % Rhodorsil-FABA			
QPac – 0.5 °C/min	70.1	1.44e0	0.9926	0.84
QPac – 2 °C/min	69.4	7.31e0	0.9967	0.81
QPac – 10 °C/min	80.1	9.25e2	0.9985	0.76
Novomer – 0.5 °C/min	28.3	3.80e-1	0.9574	0.84
Novomer – 2 °C/min	44.8	1.34e1	0.9847	0.90
Novomer – 10 °C/min	47.8	3.57e0	0.9918	0.78
	0.200 wt. % 3M-Methide			
QPac – 0.5 °C/min	62.4	2.99e-1	0.9980	0.74
QPac – 2 °C/min	73.4	4.05e1	0.9996	0.76
QPac – 10 °C/min	83.6	7.41e0	0.9980	0.71

Table 4.5 Coats-Redfern kinetic parameters for a first order reaction for UV exposed PPC films loaded with photoacid generator. All films were spun to a thickness of 10 μm when dissolved in γ-butyrolactone. Residual solvent was removed using a softbake temperature of 100°C.

Unexposed	E_a (kJ/mol)	A (s^{-1})	R^2	α_{max}
	3.75 wt. % FABA			
QPac – 0.5 °C/min	409	1.22e45	0.9744	0.69
QPac – 2 °C/min	338	5.82e35	0.9392	0.67
QPac – 10 °C/min	335	1.60e35	0.9959	0.70
Novomer – 0.5 °C/min	659	1.37e73	0.9751	0.80
Novomer – 2 °C/min	854	8.42e92	0.9733	0.78
Novomer – 10 °C/min	845	3.32e88	0.9660	0.80
	3.0 wt. % Methide			
QPac – 0.5 °C/min	489	9.99e48	0.9781	0.79
QPac – 2 °C/min	569	7.86e57	0.9956	0.36
QPac – 10 °C/min	414	7.85e37	0.9826	0.29
Novomer – 0.5 °C/min	747	3.40e78	0.9889	0.80
Novomer – 2 °C/min	783	6.01e80	0.9974	0.82
Novomer – 10 °C/min	763	8.46e76	0.9821	0.73
	0.25 wt. % FABA			
QPac – 0.5 °C/min	298	1.03e25	0.9889	0.73
QPac – 2 °C/min	463	4.34e29	0.9978	0.70
QPac – 10 °C/min	237	3.97e20	0.9651	0.74
Novomer – 0.5 °C/min	263	2.17e21	0.9781	0.48
Novomer – 2 °C/min	279	1.32e23	0.9112	0.40
Novomer – 10 °C/min	312	3.26e26	0.9849	0.57
	0.20 wt. % 3M-Methide			
QPac – 0.5 °C/min	409	2.37e38	0.9367	0.68
QPac – 2 °C/min	485	1.47e43	0.9562	0.65

Table 4.6 Coats-Redfern kinetic parameters for a first order reaction for unexposed PPC films loaded with photoacid generator. All films were spun to a thickness of 10 μm when dissolved in γ-butyrolactone. Residual solvent was removed using a softbake temperature of 100°C.

4.5.5. Solvent Cast PPC with FABA PAG

The influence of casting solvent on Rhodorsil-FABA PAG was analyzed at concentrations of 3.75 wt% and 0.25 wt%. The UV exposure dose was 1 J/cm^2 at λ=248 nm. All samples were decomposed at a heating rate of 0.5°C/min. Several casting solvents were compared including: γ-butyrolactone, acetone, anisole, and trichloroethylene. Each mixture had 3.75 wt% PAG. The DTGA curves from these films are shown in Figure 4.15. The kinetic parameters were calculated using the Coats-

Redfern method. The first order reaction parameters are listed in Table 4.7 along with the completion fraction at the point of maximum decomposition rate. A second set of samples were prepared with 0.25 wt% PAG examining the solvent effect including: γ-butyrolactone, acetone, anisole, and methylene chloride. The DTGA curves for these samples are shown in Figure 4.16. The Coats-Redfern kinetic parameters are listed in Table 4.8.

3.75% FABA	E_a (kJ/mol)	A (s^{-1})	R^2	α_{max}
	Exposed			
Acetone	45.5	4.66e-3	0.9502	0.82
Anisole	75.0	6.53e2	0.9934	0.80
γ-butyrolactone	75.8	1.74e3	0.9898	0.84
Trichloroethylene[a]	37.1	3.57e-2	0.9095	0.80
	Unexposed			
Acetone	411	3.80e40	0.9983	0.74
Anisole				
γ-butyrolactone	659	1.37e73	0.9751	0.80
Trichloroethylene	410	1.30e40	0.9685	0.74

Table 4.7 Calculated activation energies and pre-exponential factors for Novomer PPC thin films for different casting solvents loaded with 0.25 wt% Rhodorsil-FABA PAG and exposed to UV irradiation (1 J/cm^2; λ=248 nm) and unexposed samples. All values calculated using the Coats-Redfern method. Regression correlation factor (R^2) and completion fraction at the point of maximum decomposition rate (α_{max}) are also listed. a) Poor regression correlation is due to the segmented nature of the curve shown in Figure 4.15.

0.25% FABA	E_a (kJ/mol)	A (s^{-1})	R^2	α_{max}
	Exposed			
Acetone	63.4	3.79e0	0.9655	0.72
Anisole	57.5	2.82e-1	0.9883	0.60
γ-butyrolactone	28.3	3.80e-1	0.9574	0.84
Methylene chloride	48.8	8.42e-3	0.9919	0.61
	Unexposed			
Acetone	334	1.46e30	0.9935	0.87
Anisole	353	1.44e32	0.9957	0.86
γ-butyrolactone	263	2.17e21	0.9781	0.48
Methylene chloride	282	1.87e24	0.9946	0.87

Table 4.8 Calculated activation energies and pre-exponential factors for Novomer PPC thin films for different casting solvents loaded with 0.25 wt% Rhodorsil-FABA PAG and exposed to UV irradiation (1 J/cm^2; λ=248 nm) and unexposed samples. All values calculated using the Coats-Redfern method. Regression correlation factor (R^2) and completion fraction at the point of maximum decomposition rate (α_{max}) are also listed.

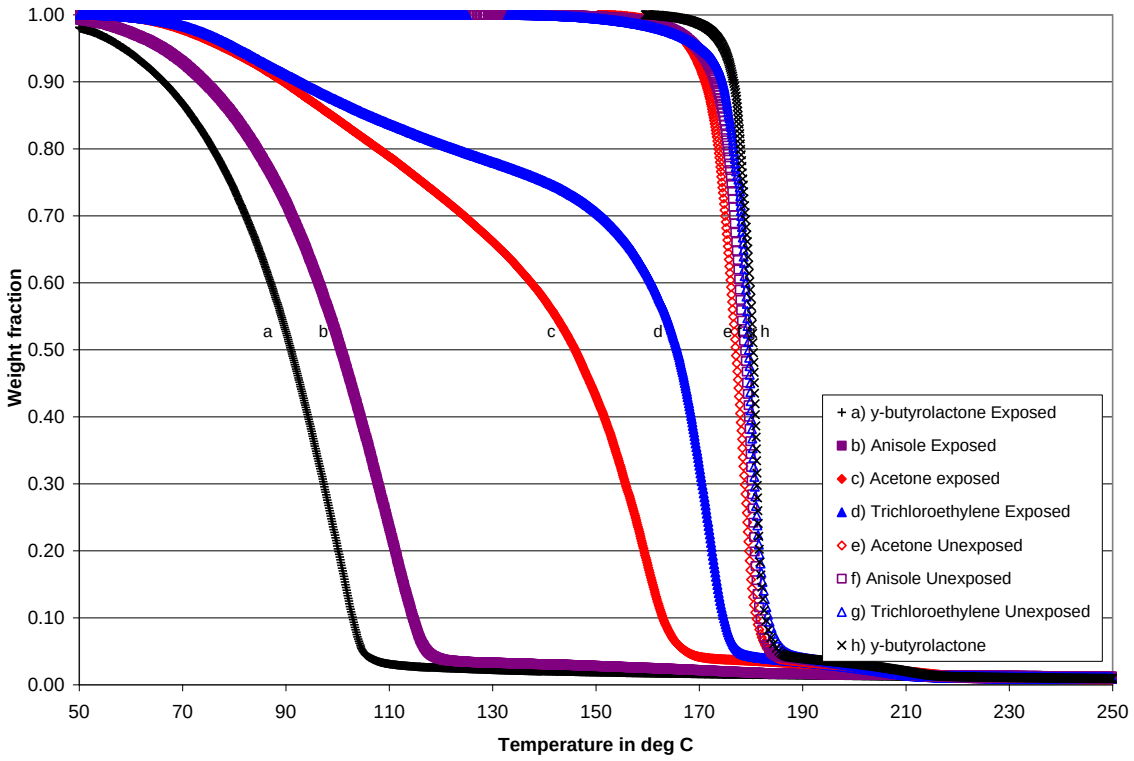

Figure 4.15 Novomer PPC with 3.75 wt% Rhodorsil-FABA PAG dissolved in different solvents: a) γ-butyrolactone (UV exposed); b) anisole (UV exposed); c) acetone (UV exposed); d) trichloroethylene (UV exposed); e) acetone (unexposed); f) anisole (unexposed); g) trichloroethylene (unexposed); h) γ-butyrolactone (unexposed).

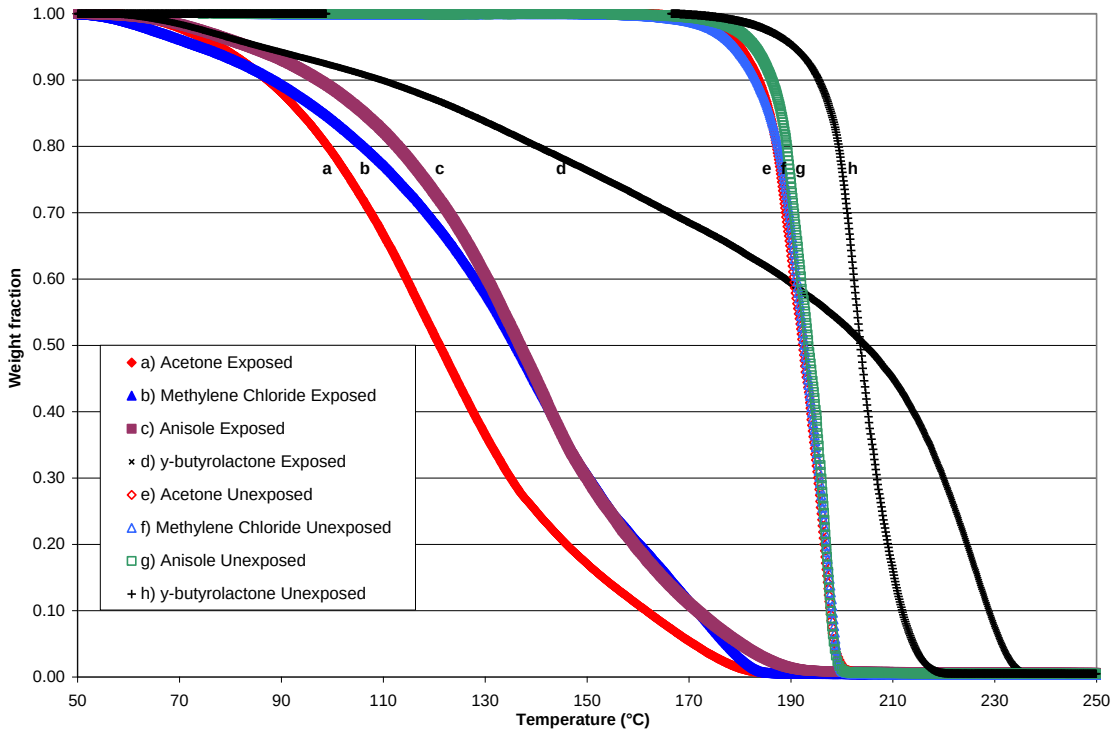

Figure 4.16 Novomer PPC with 0.25 wt% Rhodorsil-FABA PAG dissolved in different solvents: a) acetone (UV exposed); b) methylene chloride (UV exposed); c) anisole (UV exposed); d) γ-butyrolactone (UV exposed); e) acetone (unexposed); f) methylene chloride (unexposed); g) anisole (unexposed); h) γ-butyrolactone (unexposed).

Novomer material loaded with 10.0 wt%, 3.75 wt%, and 0.25 wt% of Rhodorsil-FABA PAG are compared in Figure 4.17. The residue remaining at temperatures above 180°C is primarily attributable to the initial PAG loading. This remaining fraction decomposes between 190°C and 230°C. Although not illustrated here, the decomposition curve of the Rhodorsil-FABA PAG from Figure 4.9 almost exactly overlays the "foot" observed in the decomposition range of the PAG.

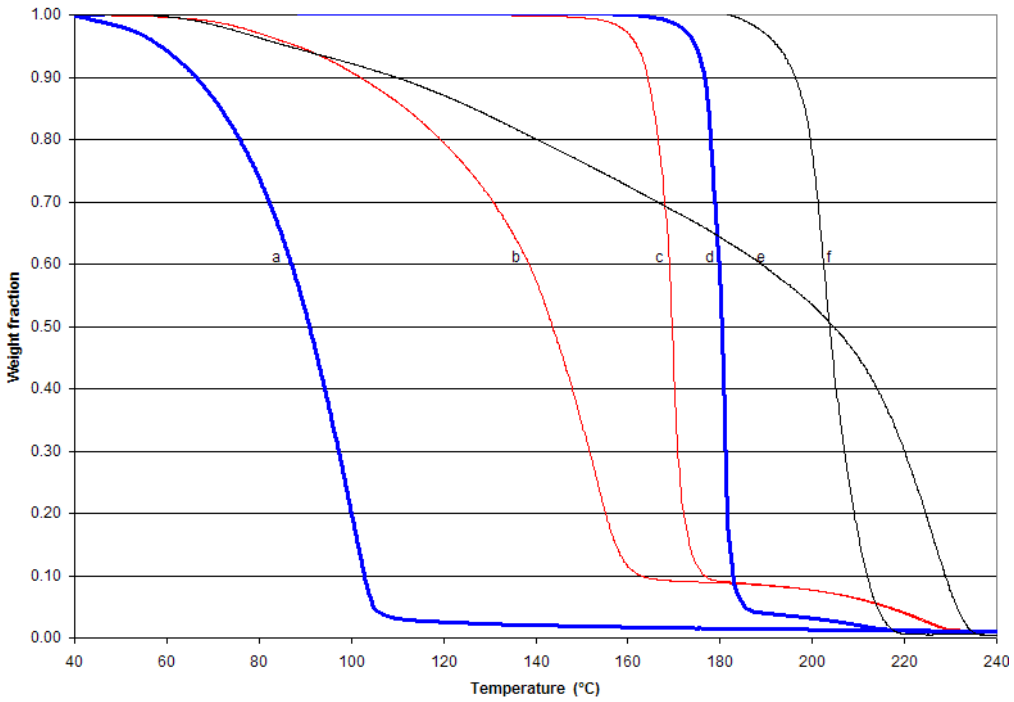

Figure 4.17 Exposed and unexposed Novomer with Rhodorsil-FABA at different concentrations. Shown in (a) and (d) are 3.75 wt%. Shown in (b) and (c) are 10.0 wt%. Shown in (e) and (f) are 0.25 wt%.

Figure 4.18 shows the comparison between the equivalent molar acid loadings (wt%. adjusted to achieve the same molar concentration) of 3M-Methide and Rhodorsil-FABA PAGs after UV exposure. PAG decomposition using triflic acid was examined to compare the effect of a strong acid which did not need to be UV exposed to form the acid. A 1.0 wt% solution of triflic acid was and PPC was made by using previously dried triflic acid and acetone as the solvent, as shown in Fig. 4.19. It was not possible to use γ-butyrolactone as the solvent because at the soft-bake temperature, 100°C, the triflic-acid containing film catalyzed the decomposition of the PPC polymer. The slightly higher temperature for weight loss with the triflic acid is consistent with the elevated weight loss temperature seen in Figure 4.15 for the acetone-solvent effect with Rhodorsil-FABA PAG.

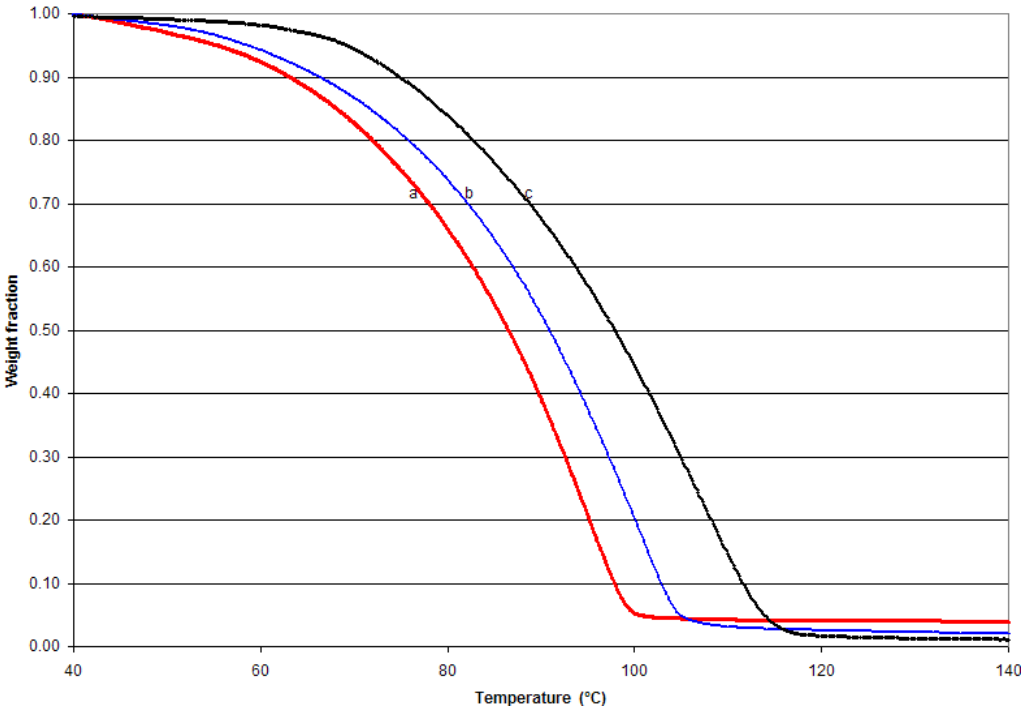

Figure 4.18 Exposed Novomer PPC with (a) 3.0 wt% 3M-Methide and (b) 3.75 wt% Rhodorsil-FABA and (c) an unexposed, air-dried film with a 1.0 wt% triflic acid.

The decomposition of PPC via chain unzipping into the monomer means that the decomposition profile, temperatures, rates, and calculated activation energies should be similar to that of the pure monomer. If the decomposition products are only the monomer, the TGA curves for PPC should match that of propylene carbonate, perhaps with a slight temperature lag due to the unzipping of the monomer. If, however, the polymer splits into lighter molecular weight fragments (i.e. acetone and carbon dioxide), then weight loss should occur more rapidly because these are more volatile products. To compare the monomer with polymer decomposition products, propylene carbonate was volatilized at heating rates of 0.5°C/min, 2°C/min, and 10°C/min. Propylene carbonate loaded with 3.75 wt% Rhodorsil-FABA and exposed to UV light was also studied at these heating rates. The DTGA curves for these experiments are shown in Figure 4.19.

The general shape is nearly identical at each heating rate, except for the foot on the PAG loaded liquid. This foot is present at the same wt% as the initial PAG loading and exhibits a second decomposition region as the PAG decomposes. Kinetic parameters extracted using the Coats-Redfern method are summarized in Table 4.9.

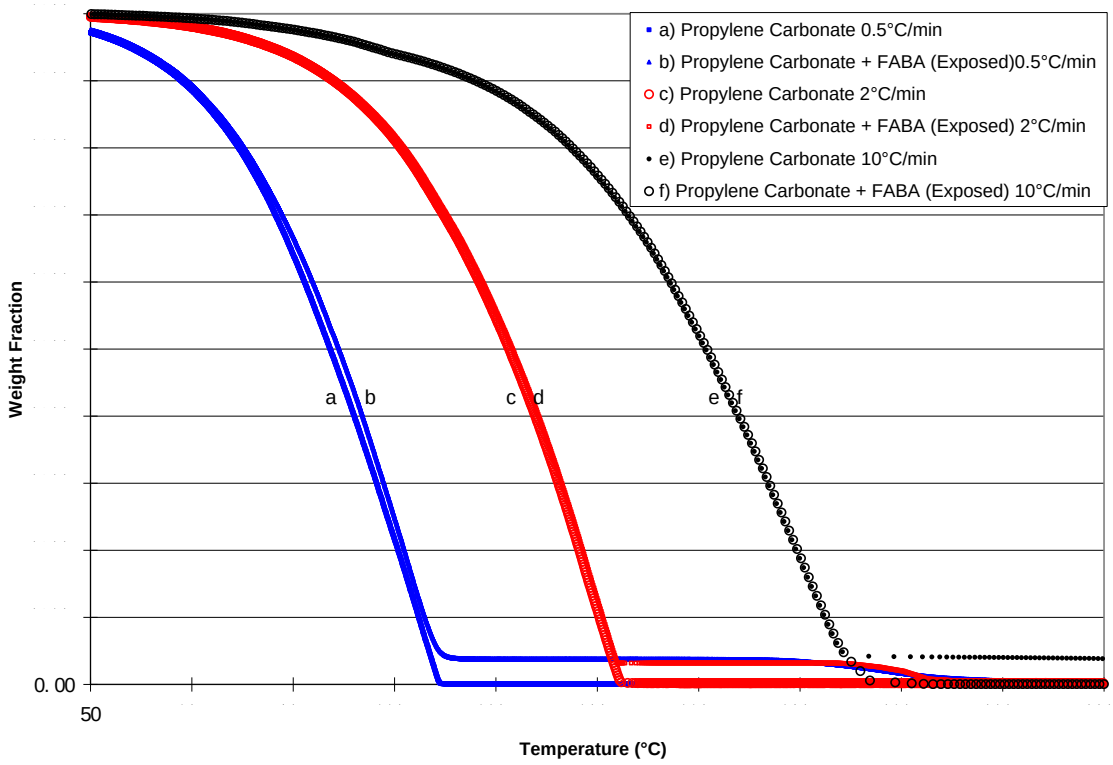

Figure 4.19 Dynamic TGAs of cyclic propylene carbonate at heating rates of (a) and (b) 0.5°C/min; (c) and (d) 2°C/min; and (e) and (f) 10°C/min. Curves a, c, and e are the monomer only. Curves b, d, and f contain 3.75 wt% Rhodorsil-FABA photoacid generator (PAG) and were exposed to 1 J/cm^2 of UV irradiation (λ=248 nm).

Propylene Carbonate (No PAG)				
0.5 °C/min	0.5 °C/min	0.5 °C/min	0.5 °C/min	0.5 °C/min
2 °C/min	2 °C/min	2 °C/min	2 °C/min	2 °C/min
10 °C/min	10 °C/min	10 °C/min	10 °C/min	10 °C/min
Propylene Carbonate (3.75 wt% FABA + UV exposure)				
0.5 °C/min	0.5 °C/min	0.5 °C/min	0.5 °C/min	0.5 °C/min
2 °C/min	2 °C/min	2 °C/min	2 °C/min	2 °C/min
10 °C/min	10 °C/min	10 °C/min	10 °C/min	10 °C/min

Table 4.9 Kinetic Parameters calculated by Coats-Redfern method of propylene carbonate without PAG and propylene carbonate with 3.75 wt% Rhodorsil-FABA PAG exposed to 1 J/cm^2 of UV radiation at λ=248 nm.

The kinetic parameters were calculated using the Kissinger method for all polymer blends evaluated in this study at multiple heating rates. The results of these calculations are summarized in Table 4.10. Additionally, the kinetic parameters extracted for the monomer with PAG and without PAG are included. Without PAG, the QPac PPC had a higher activation energy (165 kJ/mol) than the Novomer materials (136 kJ/mol and 142 kJ/mol). The mixtures containing QPac or Novomer with a high concentration of PAG before UV exposure had activation energies between 154 kJ/mol and 166 kJ/mol. UV exposure of the blends with a high concentration of PAG had lower activation energies between 45 kJ/mol and 71 kJ/mol. QPac showed a higher activation energy than the Novomer PPC. Low acid concentrations exhibited a mixed effect on the activation energies for both exposed and unexposed films with no easily distinguished trend.

	E_a (kJ/mol)	A (s^{-1})	R^2
QPac	165	1.19e16	0.9956
QPac + 0.20% Methide	121	1.81e10	0.9935
QPac + 0.25% FABA	130	1.12e11	0.9956
QPac + 3.0% Methide	157	1.34e15	0.9922
QPac + 3.75% FABA	158	2.51e15	0.9999
QPac + 0.20% Methide + 1J/cm^2 UV	134	1.02e12	0.9944
QPac + 0.25% FABA + 1J/cm^2 UV	142	1.79e12	0.9938
QPac + 3.0% Methide + 1J/cm^2 UV	58.6	3.71e4	0.9992
QPac + 3.75% FABA + 1J/cm^2 UV	71.1	3.32e2	0.9930
Novomer (MW=90 kg/mol)	136	2.39e12	0.9377
Novomer (MW=100 kg/mol)	142	8.96e12	0.9983
Novomer + 0.20% Methide	134	2.49e11	0.9999
Novomer + 0.25% FABA	165	9.92e14	0.9972
Novomer + 3.0% Methide	166	5.81e15	0.9981
Novomer + 3.75% FABA	154	3.66e14	0.9989
Novomer + 0.20% Methide + 1J/cm^2 UV	184	1.63e16	0.9487
Novomer + 0.25% FABA + 1J/cm^2 UV	150	1.34e13	1.000
Novomer + 3.0% Methide + 1J/cm^2 UV	56.0	3.15e4	0.9383
Novomer + 3.75% FABA + 1J/cm^2 UV	45.3	4.48e4	0.9986
Propylene Carbonate	50.3	1.89e3	0.9986
Propylene Carbonate+3.75% FABA+UV	48.8	1.25e3	0.9981

Table 4.10 Kinetic parameters calculated by Kissinger method for all solutions analyzed at multiple heating rates in this study. All polymer and polymer/PAG solutions were dissolved in γ-butyrolactone, cast as a film on a glass slide, and heated to 100°C to evaporate solvent. All data collected at heating rates of 0.5°C/min, 2°C/min, and 10°C/min.

Films decomposed under nitrogen exhibited widely varying behavior depending on the acid type and concentration. Samples without PAG and those which contained PAG but were not UV exposed demonstrated similar behavior. The PPC decomposed into a clear liquid product which quickly evaporated at the decomposition temperature. This decomposition occurred at approximately 190°C and appears to be consistent with depolymerization into a liquid product, which is likely propylene carbonate.

Films loaded with higher concentrations of photoacid (3.0 wt% 3M-Methide, 3.75 wt% Rhodorsil-FABA, and 10 wt% Rhodorsil-FABA) exhibited a somewhat similar

decomposition mechanism as the unloaded and unexposed samples. The onset of decomposition was much lower (by about 100°C) and the reaction occurred over a wide temperature range (from 100°C to 140°C). The films decomposed into a liquid with a dark tint which subsequently volatilized and left a dark-brown and/or black residue in the TGA pans. These samples were also observed to form bubbles in the pan, which was not seen with PPC films in the absence of PAG.

Films loaded with a low concentration of PAG (0.20 wt% and 0.25 wt% of 3M-Methide and Rhodorsil-FABA, respectively) showed very different decomposition characteristics than the unloaded, unexposed, or high PAG concentration samples. At these low concentrations, the nucleation and growth of gas bubbles in the polymer were clearly visible when the film was UV irradiated. In this case, the entrapped bubbles continuously expanded after formation, which caused the polymer to foam and expand in volume.

FT-IR was used to examine the thin polymer films deposited on KBr. Figure 4.21 shows the spectra of PPC films cast in different solvents after solvent evaporation. Figure 4.21 shows the PPC spectra for films cast in γ-butyrolactone in the presence of a small quantity of Rhodorsil-FABA. Additional spectra were gathered for UV exposed films and UV exposed films heated to 120°C. However, these spectra exactly overlay the unexposed spectra shown in Figure 4.21 but with a lower intensity due to the decreased film thickness. When the peaks are normalized for intensity around the C=O peak at 1750 cm^{-1}, they accurately overlay each other and are therefore not shown because no significant information can be discerned from them. Similar results were experienced in attempts to track film decomposition using UV-Visible light spectroscopy. Complete

decomposition of the film leaves very weak, nearly indistinguishable peaks, as has previously been reported [8].

Films with and without PAG and in different solvents exhibited very similar spectral peaks, as would be expected since the residual solvent is mostly removed and the PAG and only accounts for a few weight percent of the mixture. The broad peak at ca. 3000 cm^{-1} is attributable to C-H bond stretching in the propylene units. There may also be an OH peak hidden within this peak. The peak at 1760 cm^{-1} is attributed to the C=O of the carbonate groups. The broad peak at 1250 cm^{-1} is due to the C-O bond of the carbonate groups but also may be due to any irregularities (ether linkages) in the backbone of the polymer. The peak at 1475 cm^{-1} is due to C-C bonding in the propylene groups. The additional peaks in the 1350 cm^{-1} to 1450 cm^{-1} range are due to scissoring and bending of the C-H bonds.

As seen in Figure 4.20, the FTIR spectra of solvent cast PPC films do not distinguish the essential differences between various solvents used to cast the films. The C-H stretching (2850-2960 cm^{-1}), and bending and scissoring (1350-1470 cm^{-1}) modes exhibit slight variations between solvents. Very slight differences are seen at 1575 cm^{-1}, which may be attributed to carboxylate groups present at the ends of the polymer chains.

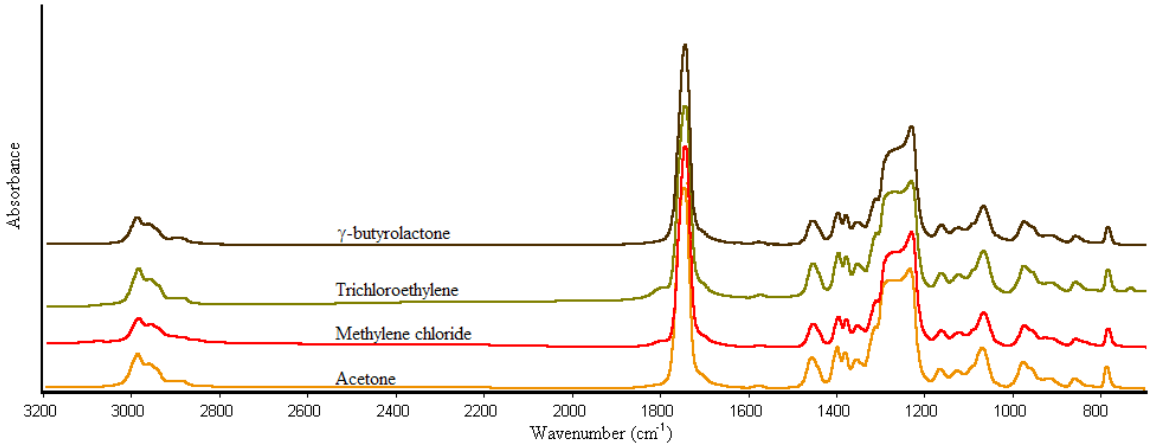

Figure 4.20 FTIR absorbance spectra for Novomer PPC dissolved in γ-butyrolactone, trichloroethylene, methylene chloride, and acetone

The influence of the Rhodorsil-FABA on the FTIR spectra is shown in Figure 4.21. Novomer PPC was dissolved in γ-butyrolactone and cast on KBr slides from solutions containing different weight percentages of Rhodorsil-FABA PAG. Additionally, the PAG alone was dissolved in γ-butyrolactone and cast on KBr. The primary peak in the Rhodorsil-FABA spectrum is seen at 1470 cm^{-1}, C-C bonding. Secondary peaks are seen at 975 cm^{-1} from the methyl groups and at 1514 cm^{-1} from benzene ring stretching. The peaks at 1470 cm^{-1} and 975 cm^{-1} are obscured by PPC peaks. The benzene ring peak at 1514 cm^{-1} is with higher PAG loadings and is the only clear difference between the spectra. No evidence of hydrogen bonding as observed in other PPC studies at 1550 cm^{-1} was observed here.

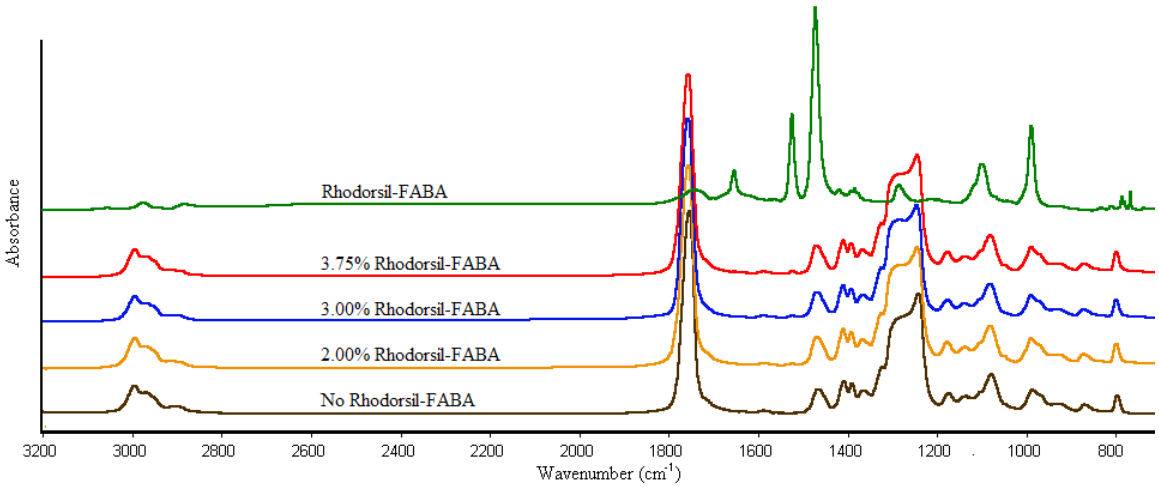

Figure 4.21 FTIR absorbance spectra for Novomer PPC dissolved in γ-butyrolactone with various weight percentage Rhodorsil FABA PAG.

4.6. Discussion

The enthalpy of vaporization of propylene carbonate has been reported to be between 49 kJ/mol [82] and 51 kJ/mol[83]. The propylene carbonate data analyzed using the Kissinger method yielded an activation energy in the same range as the as these literature values. The similar activation energies for the monomer with no additivies (50.5 kJ/mol) and with 3.75% Rhodorsil-FABA PAG (48.8 kJ/mol) indicates that the photoacid does not decompose the monomer into smaller fragment products and has little effect on the overall vapor pressure.

The activation energies calculated by the Kissinger method for the Novomer PPC with UV-exposed photoacid at high concentrations (3.0% 3M-Methide or 3.75% Rhodorsil-FABA) are very close to that of the heat of vaporization of the cyclic monomer. This suggests the formation of propylene carbonate via the chain unzipping mechanism and subsequent volatilization. The chain unzipping mechanism has been reported to be due to the formation of terminal –OH groups upon acid activation [8] and is the dominant decomposition mechanism in high molecular weight PPC[37]. Because the Novomer polymer had both higher molecular weight and higher regularity of repeat

units (HT), the lower activation energy of the Novomer material was consistent with chain unzipping into the monomer.

For the QPac material, fragmentation into larger molecular weight products likely competed with chain unzipping. Polyether groups present in the QPac PPC prevented acid regeneration by forming an alcohol termination unable to propagate the unzipping mechanism. The quenching of the unzipping mechanism by the ether groups are likely the reason for the higher activation energies calculated using kinetic analysis. This is particularly true at low concentration of PAG where acid regeneration is critical because the number of acid molecules is less than the number of polymer chains. The higher molecular weight decomposition products that result from the ether impurities may also contribute to the higher activation energy.

Deviations from the enthalpy of the monomer may also be attributed to the formation of hydrolysis products. 1,2-propanediol has been observed in PPC pyrolysates via FT-IR [37] and may form in the presence of water, although most of the water was likely removed during film drying on a hot plate. It is possible that some water remained bound within the polymer matrix and may have contributed to formation of minor products including 1,2-propanediol. Activation energies calculated using the techniques cited in this paper cannot distinguish between the cyclic monomer and the alcohol product because 1,2-propanediol has an enthalpy of vaporization close to that of propylene carbonate[84].

Decomposition of the monomer into carbon dioxide and acetone with additional heating has been reported, but this does not occur until higher temperatures than evaluated in this study. These products may result from decomposition in an oxygenated

atmosphere or at extremely fast ramp rates, but appear to be only minor products in this study. The TGA curves shown in Figure 4.19 suggest that the addition of photoacid to cyclic propylene carbonate does not dimerize or degrade the monomer. Thus, it is likely that the PAG has little or no impact after degradation of the polymer into cyclic propylene carbonate.

The exact influence of residual solvent on the decomposition behavior is very subtle. Some of the solvents evaluated in this study are capable of hydrogen bonding and thus stabilizing the PPC backbone, but no evidence of this is observed in the FTIR spectra. Additionally, the solvents evaluated in this study, with the notable exception of γ-butyrolactone, are not capable of undergoing polymerization. Although γ-butyrolactone has been copolymerized with PPC [66] and may undergo homopolymerization[85], it is difficult to polymerize except under controlled conditions [86], despite high ring strain[87]. No change in the viscosity of γ-butyrolactone was observed when photoacid was added to the solvent and UV exposed in the absence of PPC. Deviations in thermal stability due to residual solvent or interaction will depend highly on molecular weight, polydispersity, and film drying conditions and temperatures.

Without adequate photoacid loading (i.e. low weight percentages of PAG), decomposition proceeds slowly via the unzipping mechanism before proceeding via random chain scission at higher temperatures and subsequent unzipping. This results in a segmented and complex degradation curve as seen in Figures 4.13 and 4.14. The irregularity in the decomposition curves at these acid loadings levels is also likely the result of bubble entrapment of decomposition products during heating. Such effects are not accounted for in the kinetic models. TGA data and results of the open-face

decomposition observed under glass both indicate complex, multiphase behavior of the decomposition mechanism in the presence of PAG. Intumescent flame retardants (IFRs) are multicomponent systems where an acidic source chars a carbonization agent to form a low thermal conductivity layer while a blowing agent is converted to a gas and expands with heat. Consequently heat transfer into the sample and mass transfer out of the polymer are inhibited. The photoacid in our system coupled with the polymer backbone fragments potentially provide acid and carbonization agent, while the decomposition products act as a blowing agent. Chemical foaming of PPC has been reported to raise the thermal stability as measured by TGA [60-61]. The foaming effect observed for the UV exposed acid samples decomposed under glass are consistent with this expectation. Under sufficient acid loading, the polymer matrix decomposes to the liquid product and does not allow bubble entrapment. At low acid concentrations, the decomposition of the polymer matrix is incomplete allowing liquid decomposition products to convert into vapor which foams the polymer. These effects are responsible for the elevated activation energies at low acid loading as well as the complex and segmented degradation curves at these acid concentrations.

Differences in the calculated activation energies may be influenced by numerous other factors not previously discussed. Although every effort was made to mix a homogenous blend of solid polymer with photoacid generators, the local concentration of photoacid generator may have been greater than or less than the nominal concentration of the blend. The oxygen content in the TGA atmosphere may also have impacted the decomposition behavior. Although the TGA was purged with nitrogen for one hour before heating, reducing oxygen content to below 100 ppm, some experiments at

10°C/min exhibited characteristics consistent with an oxygenated environment (i.e. rapid decomposition with the absence of the "foot" observed in nitrogen environments).

4.7. Results

The acid catalyzed decomposition of PPC significantly reduces the activation energy as calculated by Coats-Redfern and Kissinger methods. The activation energies calculated using these techniques are similar to those calculated for cyclic propylene carbonate when sufficient quantities of acid are present. In these cases, the decomposition appears to occur via chain unzipping into cyclic propylene carbonate. Under insufficient acid loading, decomposition occurs via a composite decomposition mechanism where part of the polymer decomposes at low temperature and the remaining portion decomposes at higher temperatures.

Polymer purity and molecular weight impact the observed activation energy. Higher molecular weight products of the alternating copolymer most likely decompose via the chain unzipping mechanism. The high molecular weight, high purity polymer in this study (Novomer) decomposed with UV exposed PAG and had activation energies close to that of cyclic propylene carbonate. The similar activation energies suggest the acid generated upon UV exposure is sufficient to initiate chain unzipping, which is nearly identical to the reported values of the heat of vaporization. This suggests that upon acid activation, chain unzipping occurs at or below the temperature where cyclic propylene carbonate exhibits significant vapor pressure. Chain unzipping may occur at room temperature after acid activation but is not observed in thermogravimetric analysis because of the negligible vapor pressure of propylene carbonate at room temperature.

However, this is unlikely (or unzipping proceeds very slowly) as no liquid product is observed upon UV exposure without heating.

Residual solvent clearly impacts the decomposition, especially in the presence of UV activated PAG. The amount of solvent remaining in the polymer matrix was not measured and likely varied between samples and casting solvents. Because of the uncertainty regarding the solvent content within the solvent-cast films, it is difficult to say with certainty the role the solvent plays in increasing thermal stability. Other effects such as free volume/plasticization and absorbed energy in the form of heat of vaporization may also contribute to the observed thermal stability.

5. AIR-CLAD ENCAPSULATION OF COPPER CONDUCTORS USING SELF-PATTERNED POLY(PROPYLENE CARBONATE)

5.1. Overview

The incorporation of copper ions into poly(propylene carbonate) (PPC) films cast from γ-butyrolactone (GBL), trichloroethylene (TCE), or methylene chloride (MeCl) are shown to change the thermal stability of the polymer. The change in the thermal stability of the PPC is used to provide a self-aligned patterning method for the PPC on copper traces. The thermal decomposition of PPC is then used to create air-isolation regions around the copper traces. Copper metal is oxidized and dissolved into the PPC from the surface of the copper trace. The dissolved copper interferes with the decomposition mechanism of PPC raising the decomposition temperature of the PPC. The copper concentration profiles within the PPC, patterning resolution, and temperature effects on the PPC decomposition have been studied. The spatial resolution is limited by the lateral diffusion of the copper ions within the PPC. Thermogravimetric analysis (TGA) shows that copper ions make PPC more stable by up to 50˚C. Spectroscopic analysis indicates that the copper ions may stabilize the terminal carboxylic acid groups resulting in inhibition of PPC decomposition. The change in thermal stability based on exposure to patterned copper substrates results in the selective patterning of PPC without the need for an additional photo-patterning step.

5.2. Introduction

Air cavities are of interest in microelectronic packages and microelectromechanical system (MEMS) for microfluidic devices[6-7, 42-43], cantilever resonators[45], and electrical insulation[44]. Air cavity encapsulation of copper signal

lines is particularly valuable because it reduces signal-to-noise in copper connections, increase the electric field propagation velocity, and enable high frequency signaling while consuming less energy per bit transmitted. Methods of producing low-loss, air-cavity insulation which use self-aligned, simple processing techniques are especially valuable.

Sacrificial materials patterned in precisely defined geometries are required for air cavity encapsulation of components, such as electrical signal wires. Poly(propylene carbonate) (PPC) has been used as a sacrificial placeholder to define air cavity regions around electrical signal wires [7-8, 44-45]. The PPC was overcoated with a dielectric material then thermally decomposed into gaseous products where permeate through the overcoat leaving a precise air-cavity. PPC cleanly decomposes into low molecular weight products which easily permeate a variety of overcoats[6, 8, 40, 88]. Alternating layers of conductors and insulators can be fabricated with air-insulation, however, each layer of PPC requires a photolithographic step in addition to patterning of the line and via-hole connection. Copper conductors are of the most interest because they have high conductivity and low cost. Thus, air-encapsulation of copper conductors is of most interest.

PPC is a copolymer of carbon dioxide and propylene oxide polymerized at high pressure in the presence of catalyst[26, 38, 51-52, 54, 63-64, 73, 89]. The highly-regular form of PPC has the highest glass transition temperature, highest modulus, and highest decomposition temperature because longer chain polymers have fewer terminations where decomposition can initiate. PPC decomposes by chain scission and unzipping[27, 37-38, 57]. Decomposition propagates via chain unzipping at low temperatures because the cyclic monomer is more thermodynamically favorable than the straight chain polymer. At higher temperatures, chain scission competes with the unzipping decomposition mechanism. Acid activation lowers the decomposition temperature by destabilizing the polymer and promoting ring cyclization into the monomer. Acid is regenerated after each cyclic monomer detaches from the backbone, propagating

decomposition rapidly near room temperature. Heating on a hotplate is required to volatilize products, which have a low vapor pressure at room temperature.

PPC is an attractive sacrificial material for microelectronics because it decomposes cleanly into low molecular weight products with little residue in inert and oxygen-rich atmospheres. PPC is patterned by reactive ion etching or photopatterning with ultraviolet (UV) radiation when a photo-acid generator (PAG) is mixed with the PPC. The acid catalyzes the decomposition of the PPC at temperatures below that of pure PPC [7-8, 44-45]. The PPC pattern can be overcoated with Avatrel, polyimide, SU8, spin-on glass, or plasma enhanced vapor deposited (PECVD) SiO_2. Air cavities are formed by decomposing the PPC patterns and letting the products diffuse through the overcoat, leaving a gaseous void. Because PPC has a low decomposition temperature (180˚C), air cavities can be built on tetrabromo bisphenol A (FR4), bismaleimide triazine (BT), and other thermoset epoxy-fiberglass substrates and printed circuit boards (PCBs).

Acid catalyzed decomposition of PPC enables low temperature selective patterning, leaving unexposed regions on the substrate while decomposition products in the exposed regions evaporate from the surface at temperatures as low as 60˚C[40, 77]. Photosensitive PPC requires fewer processing steps for patterning and etching. However, film softening above the glass transition temperature and photoacid diffusion may distort patterns, limiting feature sizes and component density. Decomposition characteristics of PPC will depend on interactions between PPC, casting solvent, and concentration of contaminants.

Efforts to improve thermal stability of PPC have investigated increasing molecular weight[25], backbone structure[26, 52, 57, 73], cross-linking[53, 90], and low concentration additives prevent decomposition. Thermal stability enhancement of PPC has been reported by end-capping chain terminations[27, 29-30, 32] or hydrogen bonding to carbonyl oxygens[28, 33-36, 72, 75]. The most successful attempts to improve thermal stability have attempted to inhibit initiation and propagation of the decomposition

reaction. Phosphorus oxychloride, acetic anhydride, ethylsilicate, benzoyl chloride and maleic anhydride increase PPC thermal stability by end-capping terminal alcohols and preventing reaction initiation[27]. Alternatively, structures capable of suppressing unzipping have been used to hydrogen bond to the carbonyl oxygen and thus prevent propagation of the decomposition. These include octadecanoic acid [34], calcium stearate[33], montmorillonite[65, 75] and organoclays[35].

Copper dissolution into polymer and dielectric films has previously been reported for numerous other polymers but not for PPC and not as a technique for photopatterning. Low concentrations of copper compounds have been reported to decrease polymer stability in nearly all blends of polymers and accelerate both oxidative and non-oxidative decomposition [91]. The cuprous/cupric oxide mixture acts as an effective oxidation/reduction couple. Low concentrations of copper trifluoromethanesulfonate suppress decomposition of cyclic propylene carbonate under bias[92] but PPC has not been studied. Copper uptake into methylene chloride has also been reported[93]. Copper interaction with PAGs including diaryliodonium salts such as FABA occur by copper(II) oxidizing an alcohol to a ketone and reducing to copper(I) [94]. Copper(I) interacts with diaryliodonium salts to form a short-lived organocopper intermediate with both radical and ionic properties. In the presence of nucleophilic species, cationic polymerization may occur. Copper was unique in interacting with diphenyliodonium salts, as no effect was seen with salts of Ni(II), Cr(III), Fe(II), Ag(I), Co(II), Mn(III), or Pd(II).

In this paper, PPC patterns encapsulating copper traces are described which are patterned without the use of a mask or alignment procedure. The decomposition characteristics of solvent-cast, photosensitive PPC films containing trace levels of copper ions are reported. Copper ions are shown to interfere with the thermal and acid-activated decomposition of PPC resulting in higher decomposition temperatures. The quantity of copper needed to alter the PPC decomposition temperature is evaluated along the effect

on patterning characteristics. Copper appears to stabilize the carboxylic acid terminations of the PPC backbone and inhibit decomposition through the unzipping mechanism.

5.3. Experimental

Polymer solutions were prepared by mixing PPC, PAG, and solvent. High molecular weight poly(propylene carbonate) (MW=218,000 g/mol) was obtained from Novomer (Waltham, MA). Rhodorsil-FABA PAG (FABA) was obtained from Rhodia (Boulogne-Billancourt, France). TCE, MeCl, and GBL were obtained from Sigma-Aldrich (St. Louis, MO). 20 wt.% PPC was dissolved in solvent with 0.400 wt.% PAG (2.00 wt.% relative to solid polymer) and mixed for 24 hours on a bottle roller.

Copper was deposited on silicon wafers with a CVC DC sputterer using titanium as an adhesion layer. Silicon wafers were coated with a 200 Å thick layer of titanium followed by a 2500 Å layer of copper. Prior to coating copper substrate samples with PPC solution, the wafer was rinsed in a solution of dilute sulfuric acid (10% H_2SO_4 by volume). Silicon wafers were also rinsed in the dilute sulfuric acid bath to ensure fair comparison between substrates. No additional treatment of the silicon wafers was performed, such as removal of the surface oxide with HF. Surface oxide was cleaned from one wafer to test a bare silicon, but no difference between bare and oxidized surfaces was observed.

Copper patterns for diffusion effects and copper uptake measurements were patterned by sputtering a seed layer and electroplating lines to desired thickness. Pattern extension lengths were measured by profilometry and optical microscopy. Copper removal was estimated by profiling copper line surface before coating with PPC and after stripping PPC. The difference in surface profiles was calculated as the copper thickness removed. PPC films were dried for 2 hours in ambient air before stripping with acetone.

Films for analysis in TGA experiments were dispensed on wafers using a CEE spincoater and then soft-baked on a hotplate at 70 ˚C for 20 minutes. Following soft-

bake, sections of polymer film were removed from the wafer surface with a razor blade and tweezers and loaded into the TGA tin. Dynamic TGA scans were performed using a Q50 thermogravimetric analyzer from TA Instruments (New Castle, DE). PPC films were decomposed on a platinum tin in a chamber purged with 20 mL/min of nitrogen at a ramp rate of 0.5 ˚C/min. The microbalance was rezeroed prior to each experiment.

PPC films containing copper were analyzed by ICP-OES by first spincoating polymer solution on a copper coated wafer, soft baking for 10 minutes at 110 ˚C, redissolving PPC in GBL and pipetting from the surface. This process was repeated for PPC with 2.00 wt.% Rhodorsil-FABA on copper and silicon and for PPC with 2.0 wt.% H_2SO_4 on copper. To compare copper uptake by solvent alone, GBLwas heated at 110 ˚C on a copper coated wafer for 10 minutes and pipetted off the wafer surface for analysis. Solutions from the dissolved films were analyzed in a Teledyne Leeman Prodigy ICP-OES System, where samples were diluted 10:1 in dimethylacetamide for analysis. Calibration was performed prior to analysis with 1, 3, 5, 20, 50, and 100 ppb standards.

Films analyzed by FTIR were analyzed in a Nicolet Magna 560 Spectrometer. Prior to collecting each spectra, a background spectra was taken through a clean KBr disk in a nitrogen filled chamber purged at 50 mL/min for one hour after sample loading. After background collection, a polymer film was coated onto KBr via pipette, dried for 20 minutes on a hotplate at 110 ˚C, loaded into the chamber, and the chamber purged for one hour with nitrogen. Spectra were collected at a spacing of 2 cm^{-1} and averaged over 512 scans. PPC dissolved in GBL with 2.00 wt.% Rhodorsil-FABA PAG was dispensed directly onto the KBr disk. Copper-doped films were cast from PPC redissolved in GBL from a copper wafer surface as described for ICP-OES analysis. After 72 hours, the "copper rich" portion of solution segregated into a blue phase, which was pipetted and dispensed on a KBr film in the same manner as other FTIR samples.

5.4. Results

PPC patterns on copper lines were created by blanket exposing (i.e. no lithographic mask) solvent cast photosensitive PPC on silicon wafers. Copper dissolved into the PPC during solvent soft-bake and post-exposure bake, forming a copper-rich PPC layer which inhibits acid-catalyzed decomposition of the PPC. This process is summarized in Figure 5.1, which shows the maskless patterning of PPC on copper lines. The cross-section build-up process starts with a copper line on a silicon wafer or epoxy-fiber glass substrate. The copper line is then coated with PPC dissolved in solvent. The solvent was evaporated by heating the sample on a hotplate to 100˚C. During spincoating and heating, copper is oxidized and dissolved from the copper surface and taken up into the solvent/PPC/PAG film. The copper-rich PPC layer remains because it decomposes much more slowly than the copper-free regions of PPC. The pattern can then be encapsulated with overcoat support materials and ground conductors to build electrical lines. The self-patterning capability of photosensitive PPC is valuable because it eliminates masking and alignment steps and simplifies processing, potentially improving yield.

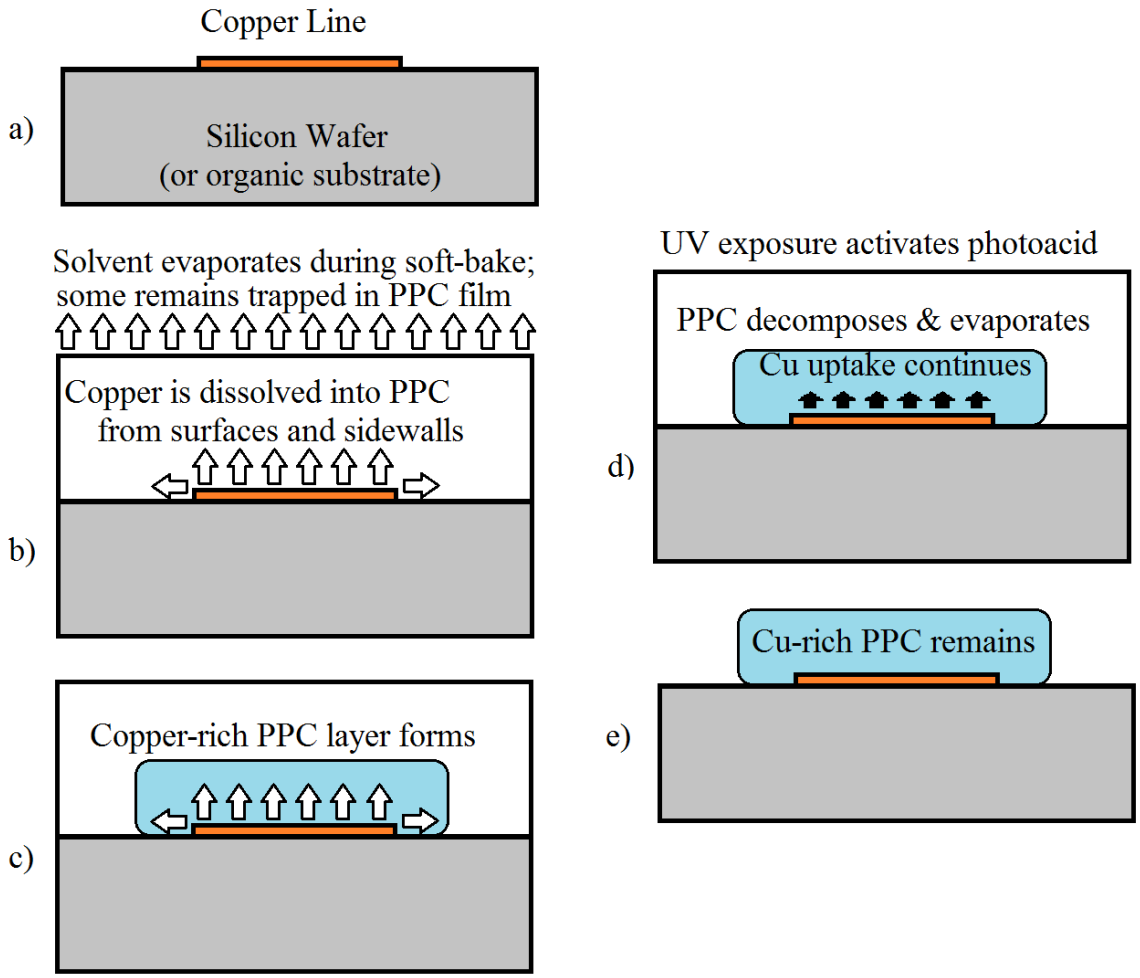

Figure 5.1 Process summary of maskless patterning of PPC on copper lines. The cross-section build-up process shows a) a copper line on a substrate which is coated with PPC dissolved in solvent which is heated on a hotplate to ca. 100 ˚C, b) evaporating solvent and dissolving copper from the line surface and edges into PPC where c) copper diffuses into PPC forming a copper rich layer which d) continues to uptake copper and does not decompose when the film is UV exposed, e) leaving a copper rich PPC layer encapsulating the line.

PPC film thickness before and after developing and lateral extension of PPC features were measured by surface profilometry and optical microscopy and are shown in Table 5.1. All films were initially 10 µm thick, decomposed completely on silicon, and partially decomposed on copper. Films cast from MeCl were developed at 78˚C for 70 minutes and 98˚C for 3 minutes. Films cast from TCE were developed at 80˚C for 41 minutes and 100˚C for 3 minutes. Both films cast from GBL were both developed at

115˚C for 3 minutes. Copper line thickness was ca. 250 nm for all films except one PPC film cast from GBL on a 17 µm thick electroplated copper line. Figure 5.2 shows a plane-view optical microscope image of PPC lateral extension when cast from GBL on a 17 µm thick copper line. PPC remains intact on the silicon surface with a lateral extension of 31.7 µm from the copper line edge. Regions labeled silicon wafer surface, PPC lateral extension, and copper in Figure 5.2 are the same in subsequent images. Figure 5.3 shows a plane-view optical microscope image of PPC cast from MeCl at the edge of 250 nm copper after 70 minutes development at 78 ˚C. Lateral extension is 9.8 µm. Figure 5.4 shows MeCl after 3 minutes of development at 98 ˚C where lateral extension decreased to 3.9 µm although a partially decomposed region extends almost 10 µm from the copper line edge. A plane-view optical microscope image of PPC cast from TCE and developed for 41 minutes at 80 ˚C is shown in Figure 5.5 with a lateral extension of 4.8 µm. Figure 5.6 shows a plane-view image of PPC cast from TCE and developed at 100 ˚C for 3 minutes. No lateral extension is observed but rather retraction of PPC up to 21.2 µm from the copper line edge.

Solvent	Initial PPC Film Thickness (µm)	PPC Thickness After Patterning (µm)	Lateral Spreading from Copper Edge (µm)	Develop Time (min)	Develop Temperature (˚C)
MeCl	10.8	7.4	9.8	70	78
TCE	10.0	5.6	4.8	41	80
MeCl	10.8	6.7	3.9	3.0	98
TCE	10.0	5.4	- [a]	3.0	100
GBL	9.8	8.1	3.0	3.0	115
GBL [b]	10.2	9.1	31.7 [c]	3.1	115

Table 5.1 PPC film thickness before and after patterning and lateral spreading of PPC line edge from copper edge after patterning. Increased pattern develop temperature reduces line edge spreading. a) Retraction of PPC from copper line edge of up to 23 µm; see Figure 5.6. Copper line was electroplated 17 µm thick. c) Increased lateral spreading is due to higher copper uptake from 17 µm thick copper line.

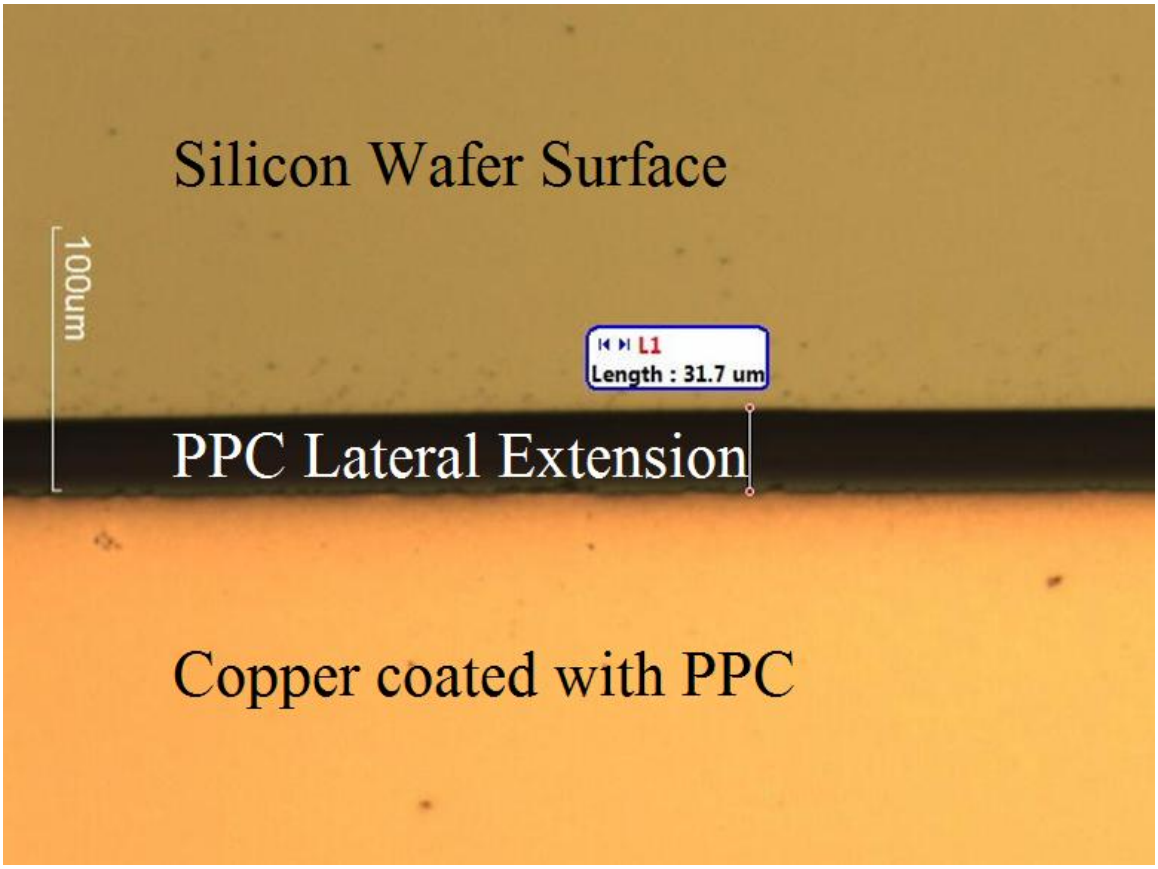

Figure 5.2: Plane-view optical microscope image of 31.7 µm PPC lateral extension from copper line edge for PPC film cast from GBL after 3.1 minute post-exposure bake at 115 °C. The copper line is 17 µm thick on silicon and allows copper uptake from the sidewall into PPC.

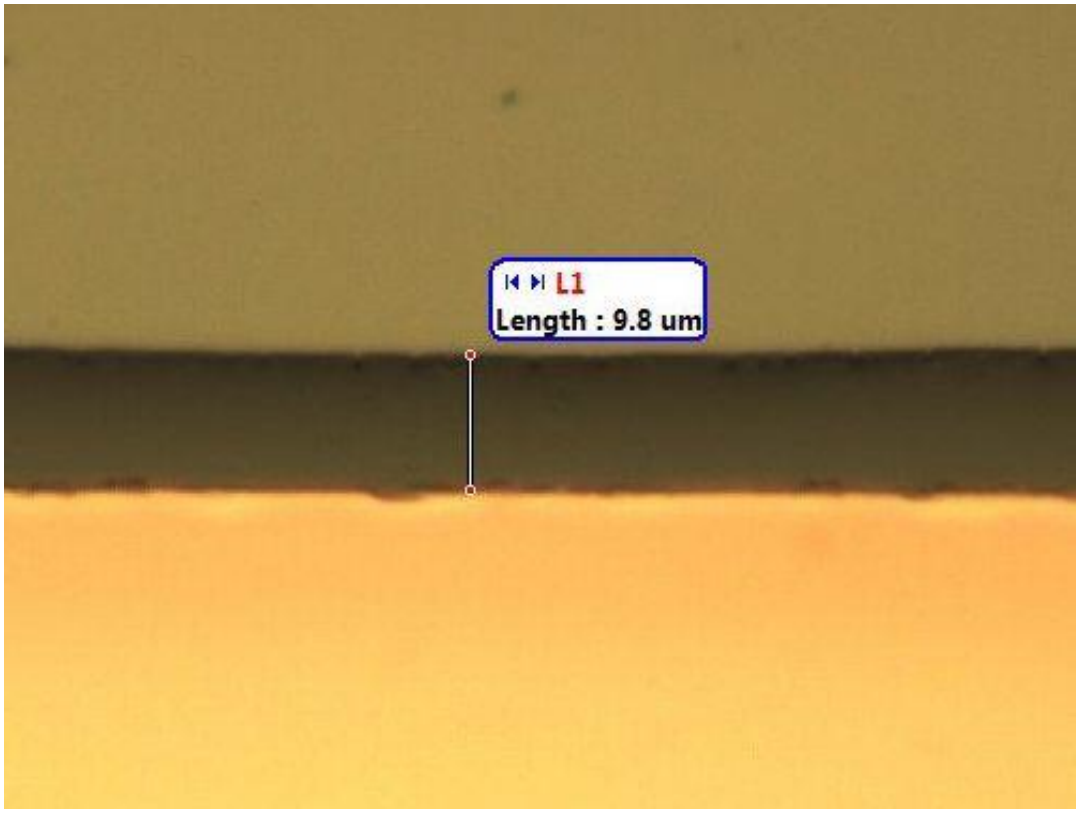

Figure 5.3: Plane-view optical microscope image of 9.8 µm PPC lateral extension from copper line edge for PPC film cast from MeCl after 70 minute post-exposure bake at 78 °C.

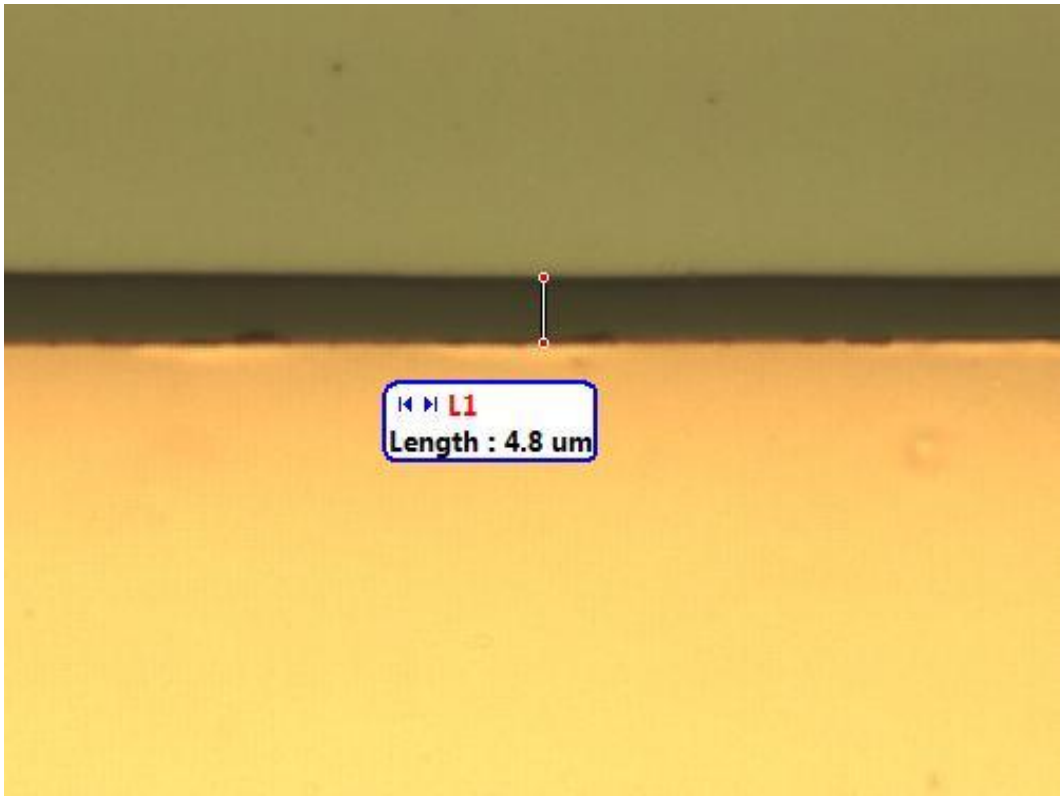

Figure 5.4: Plane-view optical microscope image of 4.8 µm PPC lateral extension from copper line edge for PPC film cast from TCE after 41 minute post-exposure bake at 80 °C.

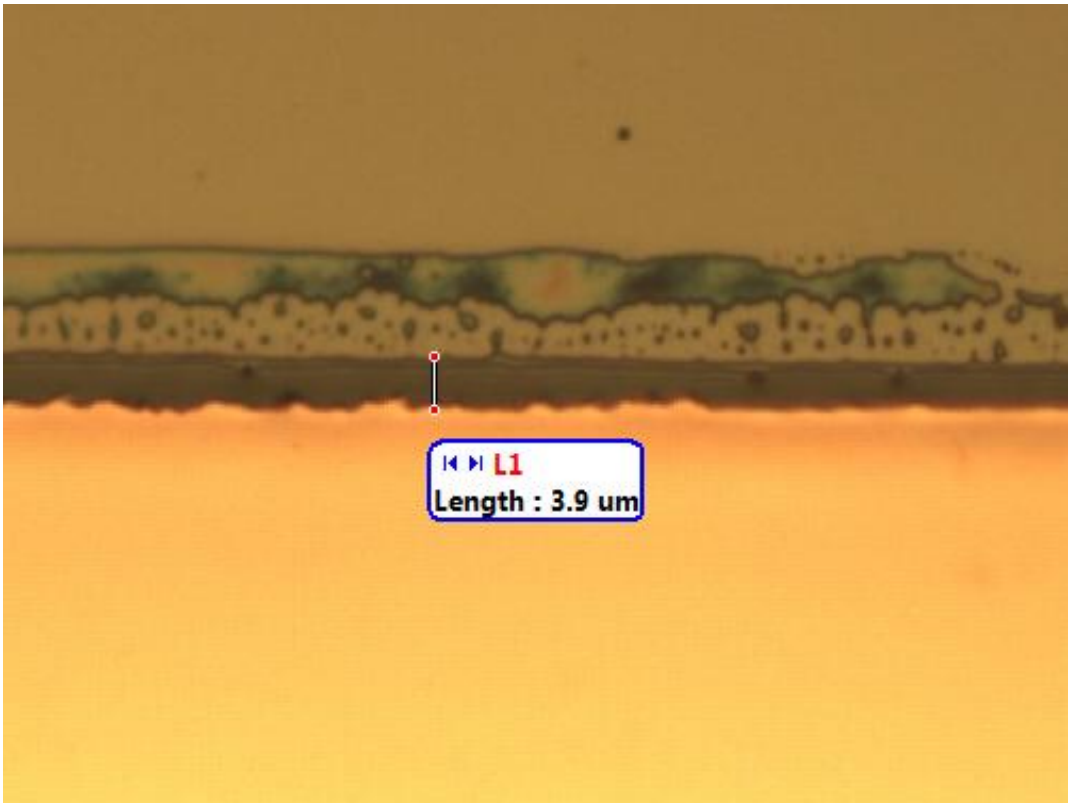

Figure 5.5: Plane-view optical microscope image of 3.9 μm PPC lateral extension from copper line edge for PPC film cast from MeCl after 3.0 minute post-exposure bake at 98 °C. Residue due to incomplete decomposition extends 10 μm from copper line edge.

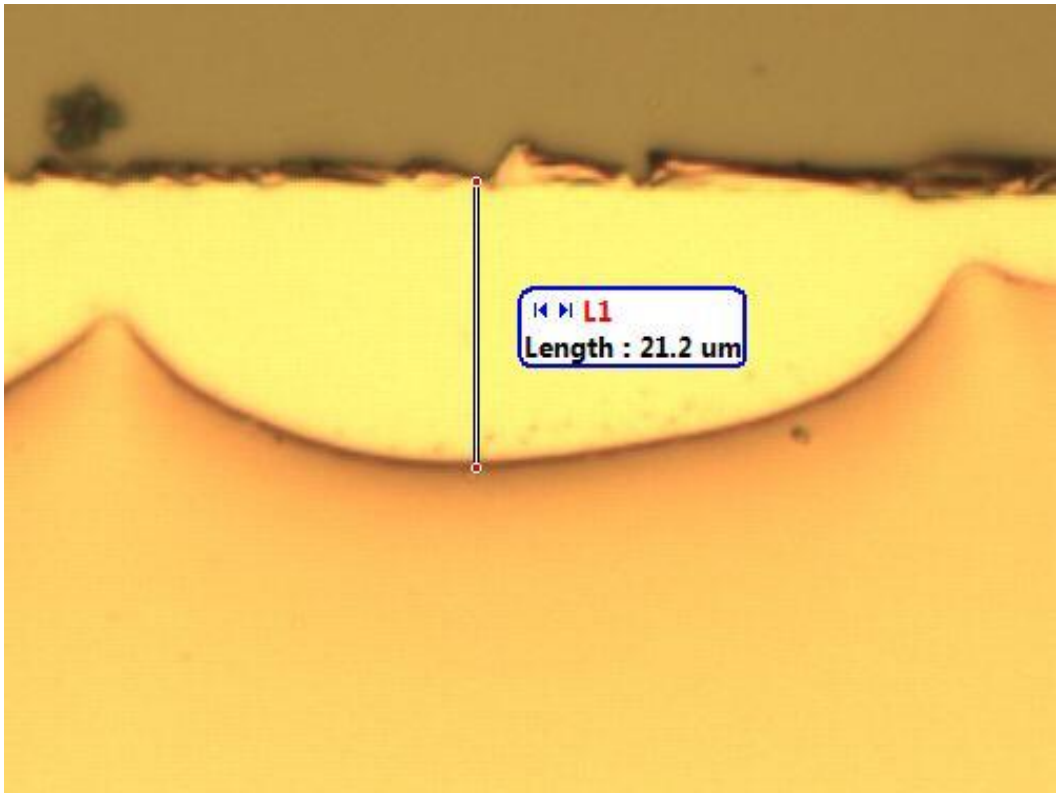

Figure 5.6: Plane-view optical microscope image of 21.2 µm PPC retraction from copper line edge for PPC film cast from TCE after 3.0 minute post-exposure bake at 100 °C.

The thickness of copper removed from the copper line surface was measured using surface profilometry. The surface profile scans of a copper line before PPC coating and after PPC coating and stripping are shown in Figure 5.7. Average copper thickness decreased by 67 Å across the top of the line surface. Copper removed from sidewalls was not measured. The decreased thickness is primarily due to oxidation and dissolution of copper ions into PPC. However, part of the decrease may have occurred when PPC was dissolved in acetone.

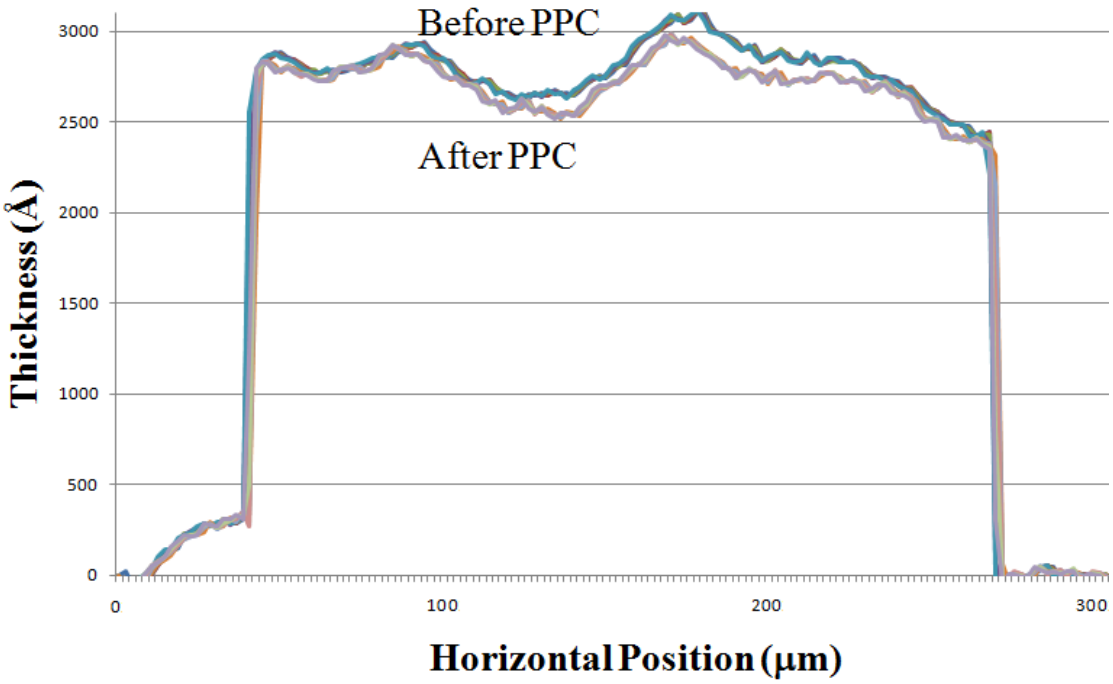

Figure 5.7: Copper removed from line surface by copper. Shown are surface profiles of a copper line before coating with PPC and after stripping PPC. The average thickness removed from the copper line surface between 50 μm and 270 μm was 67 Å and is used for calculations shown in Table 1.1.

Copper uptake into the PPC film was estimated based on PPC and copper thickness removed from the line surface were measured by profilometry. The material properties and summary calculations are shown in Table 5.2. Calculations are shown for mass, moles, molecules, and carbonyl group per film area. PPC density (1.3 g/cm^3[31, 60-61, 68]) and copper density (8.96 g/cm^3) are based on bulk properties and were not measured. Calculations of carbonyl concentrations are based on the molecular weight of one monomer of propylene carbonate (MW=104 g/mol) in the PPC backbone (~2100 monomers for 218,000 g/mol). The mass fraction of copper relative to PPC is 0.006. The atomic concentration ratio is approximately 1 copper atoms per 100 monomer units.

	Symbol	PPC	Copper	Units
Layer thickness	t	10	0.0067	μm
Density	ρ	0.0013	0.00896	$ng/\mu m^3$
Mass per area	t·ρ	0.013	0.00006	$ng/\mu m^2$
Molecular Weight	MW	$2.18 \cdot 10^{14}$	$6.35 \cdot 10^{10}$	ng/mol
Moles per area	t·ρ/MW	$5.96 \cdot 10^{-17}$	$9.45 \cdot 10^{-16}$	$mol/\mu m^2$
Molecules per area	$N_A \cdot t \cdot \rho/MW$	$3.59 \cdot 10^{7}$	$5.69 \cdot 10^{8}$	$molecule/\mu m^2$
Monomers per area	$N_A \cdot t \cdot \rho/MW^a$	$7.53 \cdot 10^{10}$	-	$C=O/\mu m^2$

Table 5.2 Material properties and calculations for estimating copper uptake concentration. a) Monomer/carbonyl concentration based on molecular weight of one mer of propylene carbonate (MW=104 g/mol) in the PPC backbone

Dynamic TGA curves ramped at 0.5˚C/min for the unexposed PPC films cast with TCE, MeCl, and GBL solvents on silicon and copper are shown in Figure 5.8. Films were decomposed at temperatures between 160˚C and 200˚C. PPC cast from MeCl on copper shows a slightly faster decomposition rate initially, but the final decomposition occurred at a temperature close to other films. PPC cast from GBL on copper showed a much higher decomposition temperature, decomposing completely ca. 230˚C.

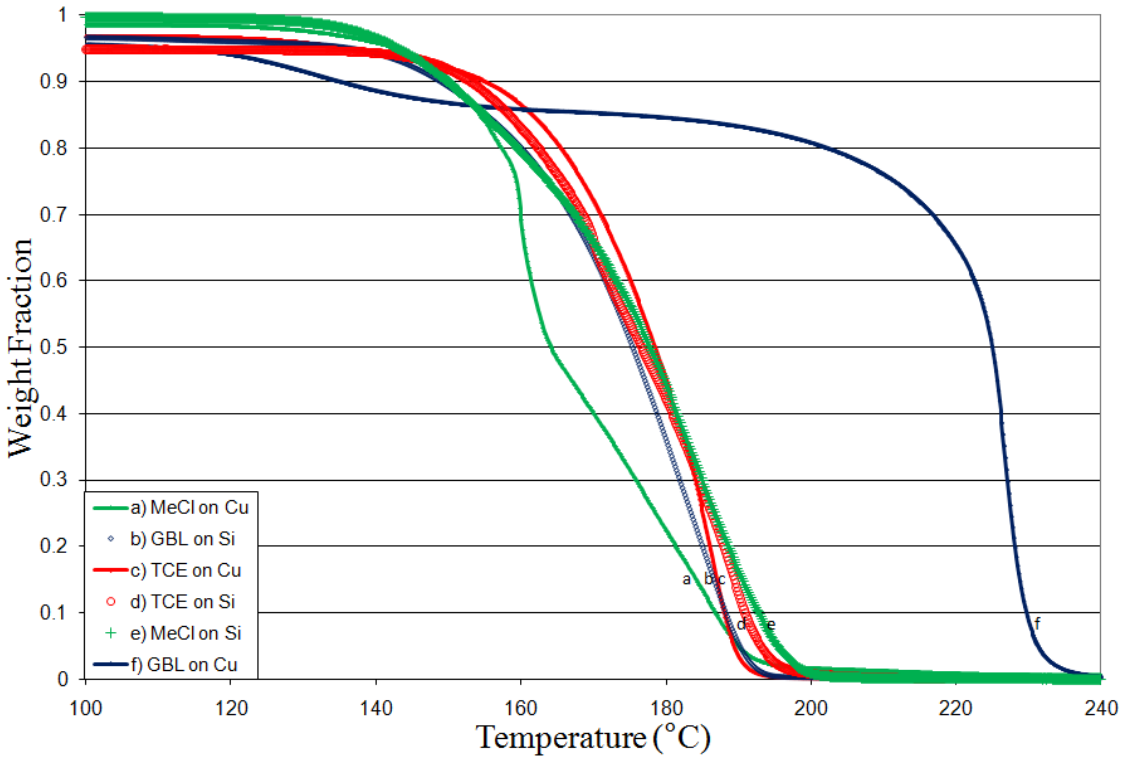

Figure 5.8 Dynamic TGA plots for PPC films on copper and silicon substrates cast from solutions dissolved in MeCl, TCE, and GBL. All samples contained 2.00 weight percent FABA relative to PPC. Films cast from GBL on copper (f) show the greatest thermal stability.

Dynamic TGA curves ramped at 0.5˚C/min for UV-exposed PPC films cast on silicon and copper with TCE, MeCl, and GBL are shown in Figure 5.9. All films were exposed to a UV dose of 1 J/cm^2 (λ=248 nm). A majority of the decomposition occurred between 60˚C and 90˚C. However, PPC cast from GBL on copper decomposed between 60˚C and 120˚C. The samples were removed from the copper coated silicon wafer by peeling the film from the copper. The sample in Figure 5.9(f) was removed from the silicon wafer surface and placed in the TGA tin with a copper flake to provide a copper source for continuous copper uptake during heating. Initially, decomposition proceeds similar to other films, but then slows dramatically, presumably due to copper uptake.

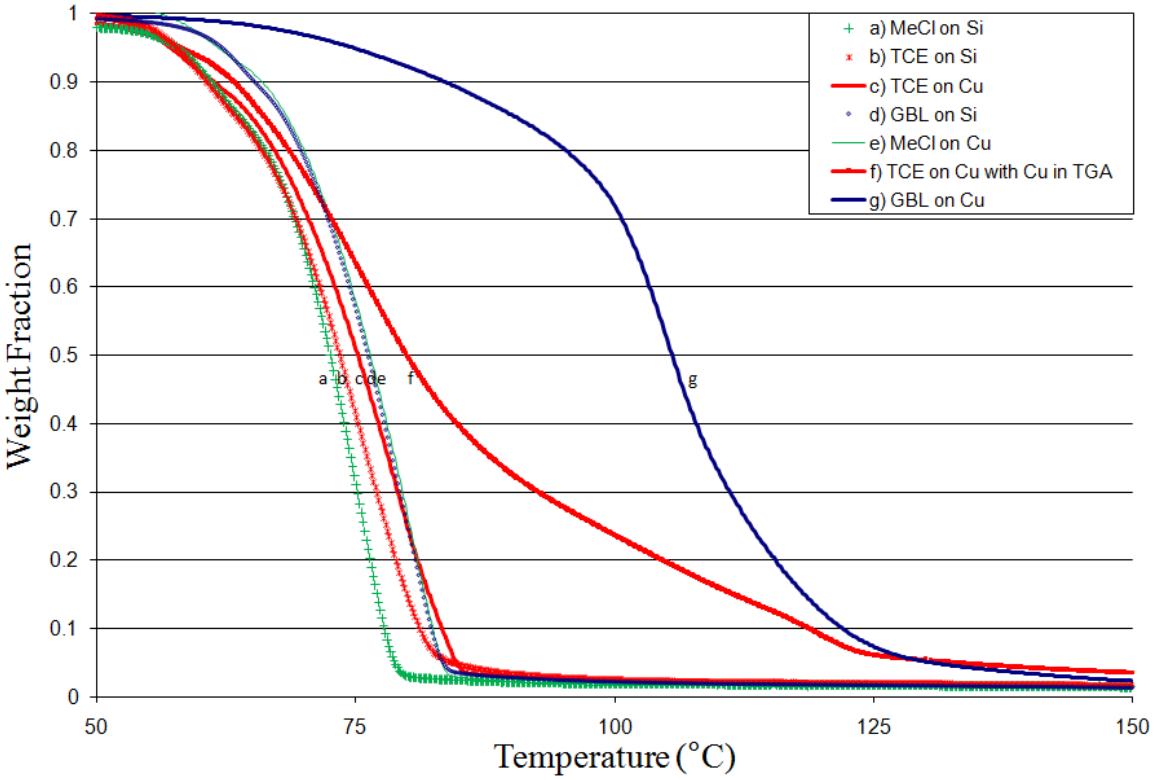

Figure 5.9 Dynamic TGA plots for exposed PPC films on copper and silicon substrates cast from solutions dissolved in MeCl, TCE, and GBL. All samples were exposed to 1 J/cm^2 UV exposure at λ=248 nm and decomposed in nitrogen at a heating rate of 0.5 ˚C/min. Films cast from GBL on copper (g) show the greatest thermal stability. Films cast from TCE on silicon and placed in the TGA tin with a copper flake (f) allowed copper uptake to continue during heating.

Isothermal decomposition TGA data are shown in Figure 5.10 for GBL-dissolved PPC films cast on silicon and on copper after UV exposure. Samples were heated at a ramp rate of 100˚C/min to 105˚C and held at that temperature while the mass was monitored. Films cast on silicon show an immediate weight loss followed by a period of time where decomposition occurred at a constant rate. Complete decomposition occurred in 15 minutes. Films on copper initially lost a small weight fraction, which may be due to residual solvent. Decomposition began about 20 minutes after achieving the dwell temperature.

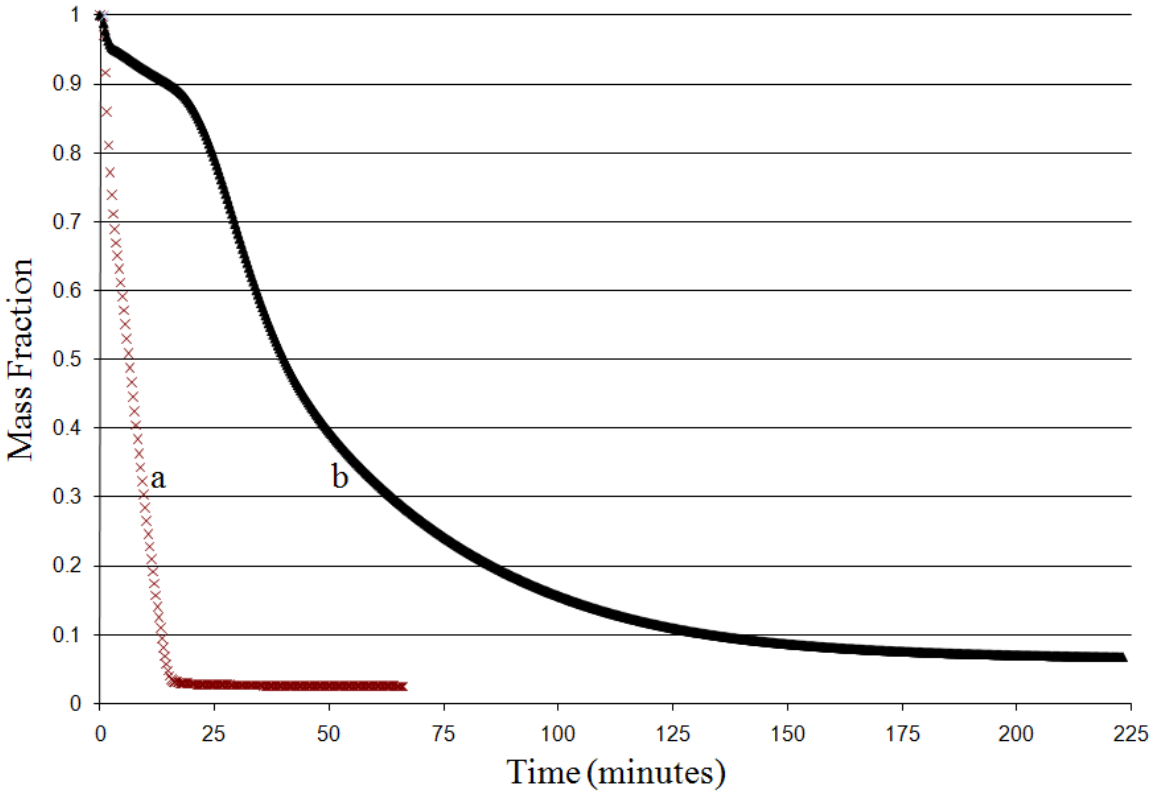

Figure 5.10 Isothermal TGA curve at 105 ˚C showing mass fraction versus time for PPC films cast from GBL dissolved PPC with 2.00 wt.% FABA on a) silicon and b) copper.

ICP-OES data are shown in Table 5.3 for GBL on copper, PPC cast from GBL on copper, PPC cast from GBL with PAG on copper, PPC cast from GBL with H_2SO_4 on copper, and PPC cast from GBL with PAG on silicon. Copper content is highest in the acid containing samples. The boron content is due to the PAG. Metal impurities such as nickel, chrome, and zinc are likely from impurities in the electroplated copper.

Solvent	Initial PPC Film Thickness (μm)	PPC Thickness After Patterning (μm)	Lateral Spreading from Copper Edge (μm)	Develop Time (min)	Develop Temperature (˚C)
MeCl	10.8	7.4	9.8	70	78
TCE	10.0	5.6	4.8	41	80
MeCl	10.8	6.7	3.9	3.0	98
TCE	10.0	5.4	- [a]	3.0	100
GBL	9.8	8.1	3.0	3.0	115
GBL [b]	10.2	9.1	31.7 [c]	3.1	115

Table 5.3 Metals content by ICP-OES for solutions of 1) GBL; 2) PPC dissolved in GBL; 3) PPC dissolved in GBL with 2.00 wt.% FABA PAG deposited on silicon, 4) PPC dissolved in GBL with 2.00 wt.% Rhodorsil FABA PAG deposited on copper; 5) PPC dissolved in GBL with 2.0 wt.% sulfuric acid deposited on copper.

The FTIR spectra for the PPC films dissolved in GBL are shown in Figure 5.11. No significant difference is observed between the film containing 2.00 wt.% FABA and the film without PAG. The spectrum for copper-containing PPC shows a decrease in the height of the peaks attributable to the terminal alcohols (at 3000 cm^{-1} and 1120 cm^{-1}). The peak at 1120 cm^{-1} is indicative of a secondary alcohol. This appears to be the interaction of the terminal carboxylic acid groups with copper. FTIR spectra for the PPC films cast in methylene chloride or TCE do not shown this difference[88].

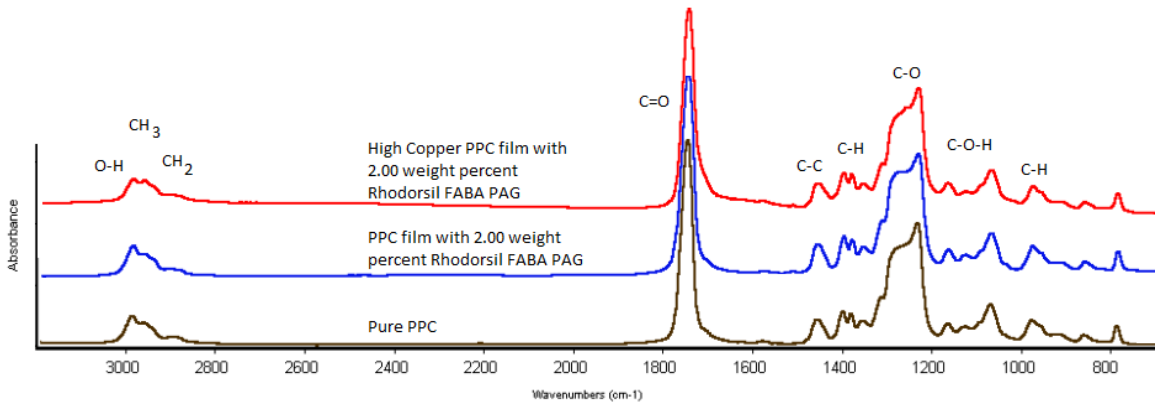

Figure 5.11 FTIR spectra for PPC films dissolved in GBL containing 2.00 wt% FABA PAG. Peaks ca. 1750 cm^{-1} (C=O) and ca. 1250 cm^{-1} (C-O) are attributable to carbonate units. Peaks ca. 2980 cm^{-1} (CH_3), 2900 cm^{-1} (CH_2), 1450 cm^{-1} (C-C), 1350 cm^{-1} and 980 cm^{-1} (CH) are attributable to propylene units. Peaks ca. 2980 cm^{-1} (O-H) and ca. 1120 cm^{-1} (C-O-H) are attributable to terminal carboxylic acid and show decreased intensity in copper-rich PPC.

Self-patterning of PPC around copper is a valuable processing step if properly integrated into a process flow. Copper lines connected by vias into the substrate may easily be encapsulated with self-patterning PPC but build-up processes require windows in PPC for electrical connection. This is illustrated in Figure 5.12 where self-patterned PPC is shown compared with masked PPC. In the self-patterned region, lateral extension from the copper edges is seen. In the masked PPC region, the dark region of "lateral extension" is actually the rounding of the pattern edge due to low contrast. The rounding of features is present in both regions, but the self-patterned region is broader due to the uptake of copper.

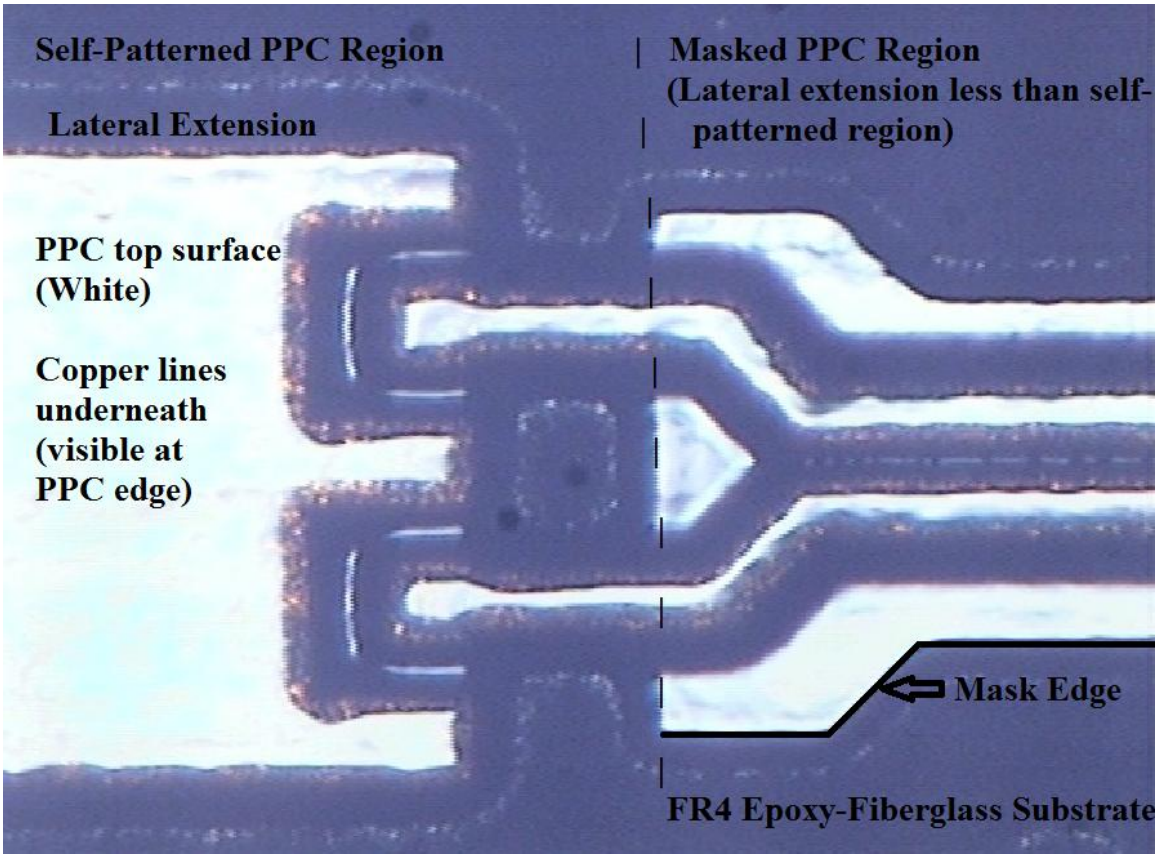

Figure 5.12 Optical microscope image of self-patterned PPC and masked PPC on copper probe pads on an FR4 epoxy-fiberglass substrate. PPC is clear but appears white in this image due to reflectance of light and clear at the edges. PPC on the left self patterns around the copper surface. PPC on the right was patterned through a mask and shows slight lateral extension (due to feature softening above the glass transition temperature). Lateral extension is more pronounced from the line edge in the self-patterned region because copper from the sidewall diffuses into and stabilizes PPC.

Shown in Figure 5.13 is an identical structure to Figure 5.12 except the probe pads on the left side of the image are protected by a 200 Å thick layer of titanium to prevent copper interaction with PPC. Complete decomposition of PPC from the probe pad surface is observed. At the boundary of the titanium layer and the photomask pattern PPC extends on copper slightly, apparently due to misalignment, although this may be due to lateral diffusion of copper.

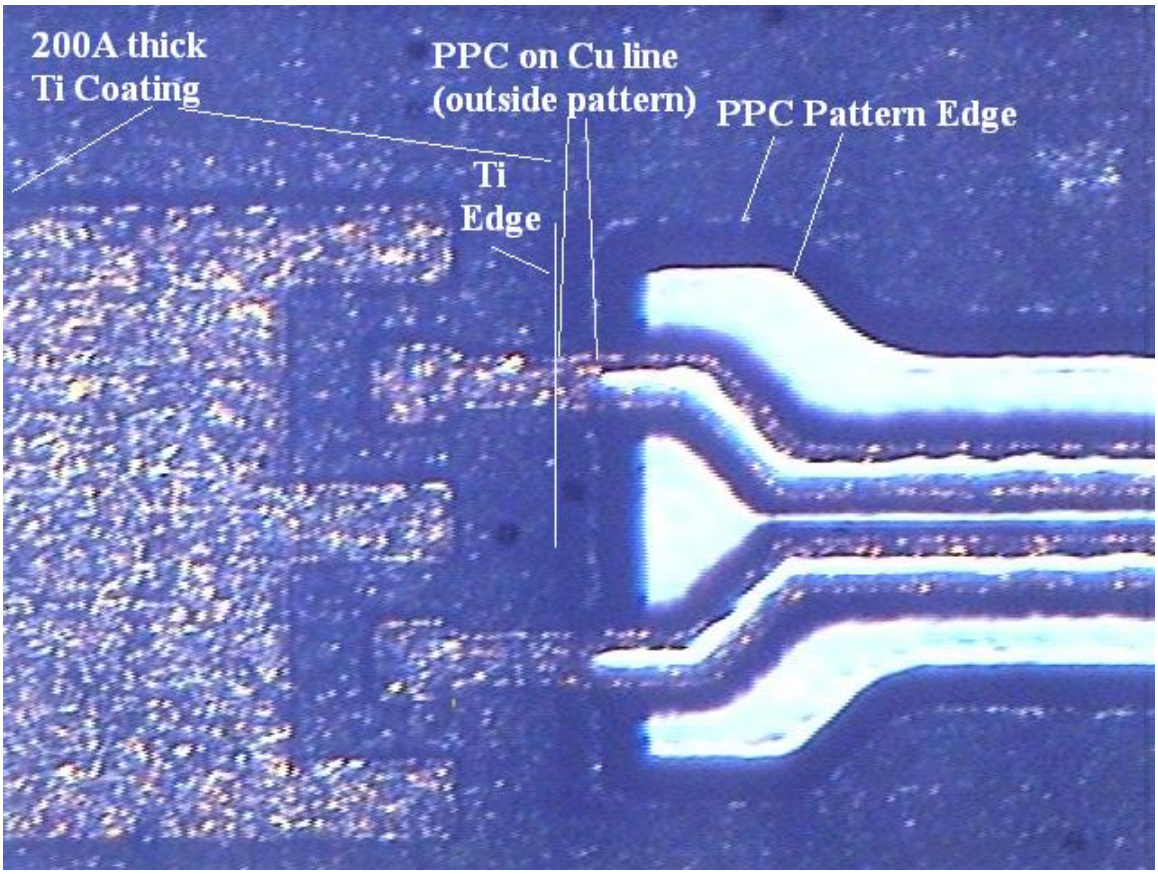

Figure 5.13 Optical microscope image of copper probe pads coated with titanium to prevent PPC self-patterning. The titanium barrier layer prevents uptake of copper into PPC, disabling the self-patterning characteristics. As in Figure 12, the white region is PPC and is masked to form the dogbone shape encapsulating the copper lines. The copper on the left side of the image has been coated with 200 Å of Ti prior to PPC spincoating and patterning.

5.5. Discussion

Copper uptake from the copper surface into the solvent-cast PPC films was evident from surface profiles and metals analysis and the color change in the PPC film. The mechanism of copper uptake is assumed to be from air oxidation of copper in the acid-laden PPC film followed by dissolution. When PPC was thermally decomposed using the higher decomposition temperature of the copper-loaded region as the means of self-patterning, a PPC film on the copper remained with some extension of the PPC to

regions outside the copper pattern. The extent of the lateral extension of the PPC from the edge of the copper line depended on solvent selection, soft-bake temperatures and times, and copper layer thickness as seen in Table 5.1.

Higher interaction time between the copper metal and PPC film allows for a longer diffusion and reaction time while higher temperature helps accelerate the reaction. The influence of temperature is most clearly viewed by comparing Figure 5.3 to Figure 5.4 and Figure 5.5 to Figure 5.6. Lateral extension is uniformly about 10 μm from the copper line edge for MeCl-cast PPC in Figure 5.3 when develop temperature was 78 ˚C. Increasing develop temperature to 98 ˚C decreases lateral extension in Figure 5.4 to less than 4 μm but a partially decomposed region about 10 μm from the edge is clearly visible. This may be PPC film that initially had low concentrations of copper but insufficient amounts to suppress decomposition. Slower reaction rates at lower temperature enable copper to diffuse from the higher concentration region to stabilize the boundary region before the film decomposes. The change from Figure 5.5 to Figure 5.6 is even more dramatic. Lateral extension for TCE-cast films of 4.8 μm at 80 ˚C becomes retraction from the copper line edge of up to 21.2 μm at 100 ˚C, indicating copper concentration at the edge of the film was inadequate to suppress decomposition. This illustrates the lower uptake rate of copper into PPC films cast from TCE. Lower temperature development and longer interaction time increase copper uptake as evidenced from these images as well as the TGA data in Figure 5.9(f).

Interaction time and diffusion effects are evident not only from lateral extension but also film thickness after patterning on copper shown in Table 5.1. GBL films retained the largest fraction of initial film thickness (greater than 80 percent), followed by films

cast from MeCl and TCE. The reason for this difference is unclear. Decreasing the develop temperature increased the remaining film thickness, suggesting the longer develop time allows copper to migrate from the metal surface further into the PPC film.

Diffusion coefficient of copper ions dissolved in PPC have not been studied here due to the complexity of solvent evaporation rates, temperature, and variability of film characteristics. However, the importance of these variables is clear from the results in Table 5.1 and Figures 5.2 to 5.6. PPC films cast using GBL require longer post exposure bake times and higher temperatures because GBL has a lower vapor pressure than MeCl or TCE. Higher levels of dissolved oxygen may enhance the copper uptake reaction by oxidizing copper for removal from the surface. GBL is also a good electrolyte and may assist copper ion transport in evenly distributing copper in the film and enhancing thermal stability. No effort was made to measure lateral extension for PPC cast from TCE or MeCl on thick copper lines but would be required for more detailed analysis of copper diffusion into PPC.

TGA measurements show that copper-rich films have greater thermal stability than films cast on other substrates. Slight increases in decomposition temperature were observed for MeCl and TCE, but GBL was the largest with more than 30 ˚C increase in thermal stability when cast on copper rather than silicon. Especially important is the isothermal decomposition plotted in Figure 5.6 for PPC films cast from GBL on silicon and copper. PPC films used in this study were approximately 10 μm thick, which means that a 10 percent change in weight (0.1 in weight fraction) correlates to a 1 μm change in thickness. Thus, nearly the full thickness of a 10 μm PPC film on bare silicon completely

decomposes in 15 minutes while 9 μm of PPC remain on copper. This thermal selectivity enables maskless photopatterning of the PPC features.

ICP-OES results showed elevated copper levels in films cast on copper compared with silicon. Some copper uptake was observed for the GBL solvent alone and PPC with GBL in the absence of PAG, but the concentrations of copper in acid containing samples are orders of magnitude larger than PPC films on bare silicon. Comparison of metals content shows the copper concentration is in excess of boron, a component of the PAG.

PPC patterns did not interact with substrates of silicon, silicon dioxide, epoxy-fiberglass boards, Avatrel, gold, silver, zinc, aluminum, chrome, platinum, titanium, and native (thick) copper oxide. PPC films were also cast onto pre-oxidized copper (via etching with hydrogen peroxide) and patterned, however, the patterning was not as sharp as that from a pure copper surface. The difference in patterning characteristics suggests an elemental copper surface is required to achieve oxidation and dissolution of the copper ions into the PPC film. The ease of oxidation and solubility of copper ions in PPC also makes it unique in this effect, which accounts for the lack of response with the other metals. The importance of copper uptake into the film is clearly illustrated in Table 5.3.

FTIR results suggest the increased thermal stability may be due to coordination with one or more terminal carboxylic acid groups. The decreased intensity of the peak at 3000 cm^{-1} associated with an OH bond and at 1120 cm^{-1} associated with a secondary alcohol both suggest an alteration of the chemical structure of the terminal carboxylic acid groups. These units may be chelating copper to immobilize the end-groups, or may even coordinate end-groups to crosslink chains, although no attempts have been made to measure changes in molecular weight. Alternatively, copper may be interacting with

carbonyl oxygens but no change in peak intensity at 1750 cm^{-1} is observed because the concentration of copper relative to carbonyl oxygens (1:100) is so low.

Techniques to prevent copper uptake into PPC as seen in Figure 5.12 and Figure 5.13 may be integrated synergistically into some process flows. Thin film dielectrics may be required with air cavities to provide confining stress and prevent surface diffusion of copper due to electromigration[95]. Plasma enhanced vapor deposition (PECVD) coating of SiO_2 or other thin film dielectric may be used to protect PPC from copper interaction. Similarly, metal barrier layers for subsequent process steps may be required on metal contacts to prevent formation of oxides or brittle intermetallics during processing.

5.6. Conclusions

Self-patterned PPC can be used to encapsulate copper lines on silicon and epoxy-fiberglass substrates by copper uptake into the PPC film to alter decomposition characteristics after UV exposure. Thermal stability increases for PPC films cast from GBL, TCE, and MeCl on copper substrates, allowing selective patterning around traces on a substrate using all three solvents. Patterning characteristics depend on copper line geometry and processing temperatures and recipes. The self-patterning capability is valuable for creating air-cavity electrical interconnects with fewer process steps and at lower cost.

Although self-patterning PPC is potentially advantageous for many applications, careful design is required to minimize process steps and barrier layers. Detailed analysis of diffusion rate, concentration profiles, patterning resolution and feature size, and temperature effects on film drying will be required for process integration. Understanding

of the mechanism and kinetics of copper uptake will also be required for process modeling.

Concentration is clearly important as GBL films showed the highest thermal stability when the copper concentration was the highest. Measurements of lateral diffusion and TGA results emphasized the differences in decomposition rates due to copper concentration and availability. PPC films removed from copper also exhibit a light blue-green color not seen in other films, which may be indicative of elevated copper levels. For many consumer and optical applications this shading may be an undesirable effect but discoloration is acceptable in sacrificial applications for microelectronics as long as residue does not interfere with electrical performance.

6. PHOTODEFINABLE INORGANIC-ORGANIC HYBRID GLASSES FOR AIR CAVITY PACKAGING OF MICROELECTRONICS AND MICROELECTROMECHANICAL DEVICES

6.1. Introduction

Energy efficient electrical signal wires transmitting large data rates are required for future generations of microprocessors and microelectronic packages. Low-loss interconnects require low resistance conductors (e.g. copper) and low capacitance dielectrics (e.g. air) to meet the requirements at the end of the International Technology Roadmap for Semiconductors[96]. The ideal low-k dielectric is a gaseous cavity but structural support layers are needed for buildup processes and confinement of surface copper to prevent electromigration[95]. Support materials must have high modulus, low dielectric constant and loss tangent, and high permeability to decomposition products during cure but low permeability to gaseous species (primarily N_2, O_2, and H_2O) during operation to maintain an inert environment inside the cavity.

Air cavity overcoats include SiO_2 deposited by plasma enhanced chemical vapor deposition (PECVD), polynorbornenes, and polyimides. Thin overcoats are preferred due to aspect ratio limitations for patterning and metallization. However, thin polymer overcoats may deform during decomposition of the sacrificial material yielding irregular dimensions or channel collapse. Improved reliability is achieved with an SiO_2 barrier layer between sacrificial material but requires additional processing. Air-gaps formed by sacrificial polymers encapsulated with an overcoat have been used for on-chip[97-98] and off-chip[44] low-k dielectrics, microfluidic channels[6-7, 42], and resonator packaging[8, 45].

Inorganic-organic hybrid “glasses” are uniquely suited for air-gap overcoats because they have high strength, low gas diffusivity, low solubility at operating temperatures, high permeability at processing temperatures, and low dielectric constants and loss tangents. Inorganic-organic hybrid “glasses” containing carbon and an inorganic atom, typically silicon or [99]. Hybrid glass benefits include greater thermal and chemical stability than organic polymers and due to the dual nature of the backbone. Highly cross-linked inorganic-organic hybrids provide mechanically robust film with easier processing than plasma-deposited SiCOH films. Hybrid glasses’ unique properties have been used in low-k dielectric layers[100], optical data storage [101-104], heat sensitive coatings, fuel cell membranes [105-106], and paper release layers [107].

Hybrid glass monomers, initiators, and diluents control properties of films formed by epoxide ring opening [108] or hydrolysis of oxysilane groups. Physical blends of inorganic and organic polymers fail due to phase segregation[108],[109] and brittle films[110], especially with diluents[108],[111]. Monomers such as 1,3-bis[2-(3,4-epoxycyclohexyl)ethyl]-1,1,3,3-tetramethyldisiloxane (BECHETS), (2,3)-epoxy,4-cyclohexylethyltrimethoxysilane (ECHETS), 3-glycidopropyltrimethoxysilane (3-GPTMS), methylsilsesquioxane (MSQ), and hydrogen silsesquioxane (HSQ)[112] are chosen as starting monomers because they undergo condensation reactions to form di-mers, tri-mers, and ultimately longer chain molecules which become rigid due to increasing cross-link density. To reduce film stress and cracking due to brittle homopolymer films [113], flexible linkages (ethers, esthers, alkanes, etc.) are introduced to add rubbery characteristics. Difunctional cyclohexyl silicon based epoxies like BECHETS are excellent cross-linkers because epoxide rings can be activated with

PAG[114], and are more reactive [115] with better photodefinability [116] than organic analogs.

Photodefinable epoxies offer benefits over spin-on glasses like HSQ and MSQ because they don't require separate patterning layers and can be used for thick films. Acid activation of epoxies initiates polymerization via an onium salt PAG sensitive to ultraviolet (UV) light. Upon UV exposure, the PAG dissociates to forming a strong conjugate acid of the basic anion. Protonation extends oxirane bond lengths, permitting nucleophilic attack [113] and converting the epoxy as rapidly as 3 seconds[103]. Photodefinable epoxies minimize process complexity but PAG residue may offset the benefits of fewer processing steps. Fragments from PAG decomposition impact mechanical properties of cured films by increasing brittleness, lowering T_g[114, 117], and increasing oxidation[118]. Because of these undesirable effects, photoinitiator concentration should be minimized.

In this work, BECHETS (shown in Figure 6.1) was investigated as an overcoat for air-gap structures. PAG was added to monomer and activated with UV light to polymerize epoxy groups. Curing properties were studied with differential scanning calorimetry (DSC) and Fourier transform infrared spectroscopy (FTIR). Blending with the tetrafunctional monomer ECHETS (shown in Figure 6.2) increased modulus and hardness. Concentrations between 0.066 wt.% and 2.00 wt.% of PAG in monomer were studied in pure species, diluted in isopropanol, and in blends of difunctional and tetrafunctional monomers.

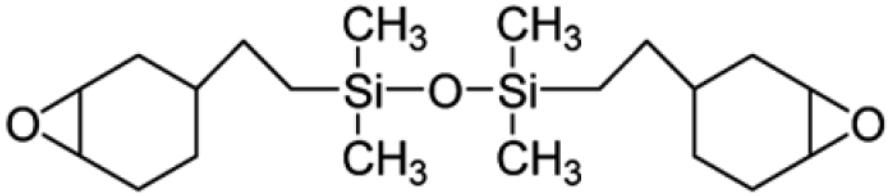

Figure 6.1 Chemical structure of 1,3-bis[2-(3,4-epoxycyclohexyl)ethyl]-1,1,3,3-tetramethyldisiloxane

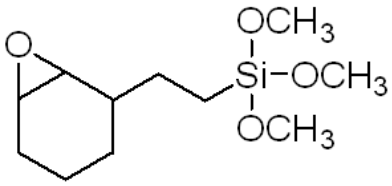

Figure 6.2 Chemical structure of (2,3)-epoxy,4-cyclohexylethyltrimethoxysilane

BECHETS films investigated by nanoindentation had lower modulus and hardness than blends with ECHETS. Curing in nitrogen increased modulus and hardness, but films cracked and flaked at ECHETS concentrations greater than 50%. Low concentrations of PAG and alcohol-diluted monomers yielded flaky films. DSC results used to study degree of curing indicated an additional exotherm when PAG is added to monomer. Exposure to increasing UV dose eliminates this exotherm. Exposure doses of 2 J/cm^2 shows no difference from a dose of 1 J/cm^2, indicating full activation after 1 J/cm^2 exposure. All DSC scans exhibit a sharp endotherm ca. 252 °C, likely due to crystalline rearrangement of the cyclohexyl ring. Photosensitive films encapsulating the sacrificial polymer poly(propylene carbonate) (PPC) collapsed during air cavity formation due to overcoat sagging. Air cavity collapse, the brittle nature of ECHETS blends, and the

inability to tune film thickness limits applications of BECHETS in microelectronics packaging.

6.2. Experimental

All materials were used as received from the suppliers. Reactants were mixed in a bottle roller for at least 24 hours prior to use. Hybrid glass films were observed qualitatively by curing on glass slides, silicon wafers, and FR4 boards. Films studied in differential scanning calorimetry (DSC) experiments were UV exposed in aluminum tins and immediately covered with aluminum caps prior to curing. Films used in Fourier transform infrared spectroscopy (FTIR) were cured on KBr crystals in a well-purged nitrogen environment in a quartz tube furnace for two hours prior to analysis. Films analyzed by nanoindentation were cured on silicon wafers at 180 C for two hours in a nitrogen purged tube furnace.

6.2.1. Materials

The monomer reactants BECHETS, ECHETS, and 3-GPTMS were obtained from Gelest (Morrisville, PA). FABA PAG was obtained from Rhodia (Boulogne-Billancourt, France). Bis(4-tert-butylphenyl)iodonium tris(perfluoromethanesulfonyl)methide (3M-Methide) was obtained from 3M (Minneapolis, MN). Bis(4-tert-butylphenyl)iodonium p-toluenesulfonate, diphenyliodomium 9,10-dimethoxyanthracene-2-sulfonate, and bis(4-tert-butylphenyl)iodonium triflate were obtained from Sigma-Aldrich (St. Louis, MO).

The chemical structure of FABA is shown in Figure 6.3. Chemical structures for additional PAGs are not included here because DSC and FTIR data reported here are based on polymerization using the FABA PAG.

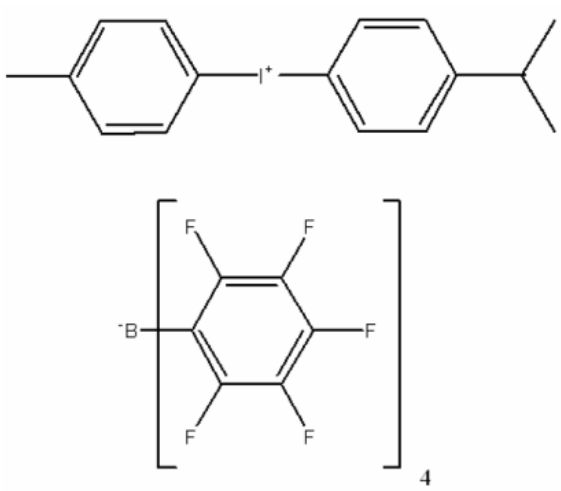

Figure 6.3 Chemical structure of photoacid generator 4-methylphenyl[4-(1-methylethyl)phenyl] iodonium tetrakis(pentafluorophenyl)borate.

2.0 wt.% 4-methylphenyl[4-(1-methylethyl)phenyl] iodonium tetrakis (pentafluorophenyl)borate from was dissolved in BECHETS. An equivalent molar concentration was made using Bis(4-tert-butylphenyl)iodonium tris(perfluoromethanesulfonyl)methide (1.60 wt%). Equivalent molar concentrations were also prepared using (bis(4-tert-butylphenyl)iodonium p-toluenesulfonate (1.11 wt.%) and bis(4-tert-butylphenyl)iodonium triflate (which showed essentially no solubility and no effect of UV radiation, and bis(4-tert-butylphenyl)iodonium triflate from Sigma-Aldrich (1.07 wt.%), which dissolved but showed no reactivity or degree of curing after UV radiation.

6.2.2. Differential Scanning Calorimetry (DSC)

Differential scanning calorimetry (DSC) were performed on a Seiko Instruments DSC220C system. Calibration was first performed using the aluminum tin used in the experiment. Photosensitive formulations of BECHETS were transferred into aluminum tins via glass pipette. Solutions were UV exposed, loaded into the DSC chamber uncapped, and purged with nitrogen for 10 minutes at a flowrate of 50 mL/min prior to

the start of the scan. Scan rates of 0.5 ˚C/min, 2 ˚C/min, 5 ˚C/min, and 10 ˚C/min were used in this study, although not all scan rates were performed for all UV exposure doses.

6.2.3. Fourier Transform Infrared Spectroscopy (FTIR)

Fourier transform infrared spectroscopy (FTIR) was performed on a Nicolet Magna 560 spectrometer in transmission mode through a hybrid glass film cured on a KBr crystal. A background sample for calibration was taken before each film. The chamber was purged in nitrogen for 30 minutes at a flowrate of 100 mL/min prior to analysis to eliminate the effects of trace gases. The scan resolution was 0.5 cm^{-1} and all results are the average of 512 scans.

6.2.4. Nanoindentation

Nanoindentation results are reported for quasistatic nanoindentation using a Hysitron Triboindenter. A Berkovich tip (three sided pyramid) was used to vary the load from 250 μN to 7500 μN over a grid of 25 points per sample. The reduced modulus and hardness results are based on the Oliver-Pharr model. The hardness reported here is defined as the applied load per unit area. These techniques have previously been detailed for polynorbornene based epoxies [119].

6.2.5. Photopatterning and Plasma Etching

The ability to photopattern fine features and resist plasma etching are critical properties required of inorganic-organic hybrid glasses. Photopatterning of the material was achieved by UV exposure (λ=248 nm) of a film of photosensitive BECHETS through a quartz mask. Following UV exposure, samples were rinsed with isopropyl alcohol to remove the unreacted monomer, leaving features on the wafer surface.

Plasma etch resistance was analyzed using a Plasma-Therm Reactive Ion Etcher with an operating frequency of 13.56 MHz. The plasma power was 250 W and the chamber pressure was maintained at 310 mTorr with a gas flowrate of 90 cc/min of O_2 and 10 cc/min of CHF_3.

6.2.6. Air Cavity Formation

The sacrificial polymer poly(propylene carbonate) was photodefined with Rhodorsil FABA as has been previously described [6, 8, 40, 44]. The width of the sacrificial material in the test structures was 600 μm. Three different heights of sacrificial material were patterned: 10 μm, 20 μm, and 30 μm. These thicknesses were chosen because they are the approximate dimensions of interest for board-level microstrip lines and packaging of MEMS resonators. Patterns of this dimension have also been successfully fabricated in the past using polynorbornene and polyimide based overcoats, so inorganic-organic hybrids must perform at least as well to be viable replacements.

The sacrificial polymer was defined on a silicon wafer and overcoated with photocurable BECHETS loaded with 2.00 wt.% Rhodorsil-FABA. The film was exposed to 1 J/cm^2 of UV exposure dose. The film was then heated in a nitrogen purged Lindberg quartz tube furnace to 180 ˚C. The heating rate was 1 ˚C/min and the sample was held at temperature for 2 hours. The nitrogen flowrate was 10 L/min and the tube was purged for 15 minutes prior to heating.

6.3. Results and Discussion

Photopolymerization of BECHETS was achieved by addition of 2.00 wt.% the presence of ECHETS and exposure to UV light. Films diluted with isopropanol also formed films in some regions of the glass slide while other regions remained bare due to

phase segregation. Lower concentrations of PAG (0.66 % and 0.066%) also achieved polymerization but curing and mechanical properties were not investigated. Air cavities were formed by decomposing poly(propylene carbonate) with BECHETS. However, because the cavities collapsed at geometries where polynorbornene based dielectrics have succeeded at the same thickness, BECHETS is an unattractive overcoat material for air cavity encapsulation.

The general polymerization scheme for monomers of BECHETS only is shown in Figure 6.4. Highly regular straight chain polymers are formed as a result of the polymerization. The general polymerization scheme for monomer blends of BECHETS and ECHETS is shown in Figure 6.5. More rigid films result with increasing concentration of ECHETS because the tetrafunctional monomer can form cross-links

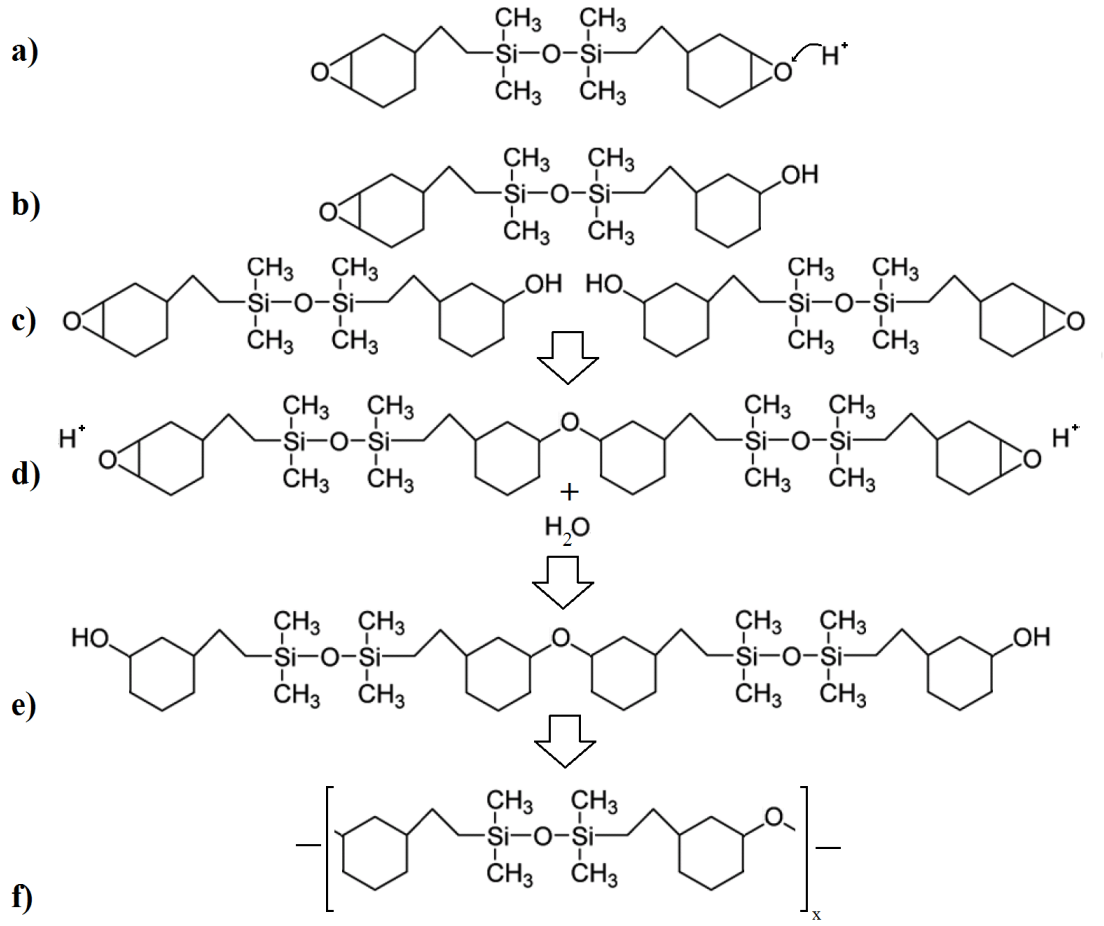

Figure 6.4 General polymerization scheme of acid activated monomers of 1,3-bis[2-(3,4-epoxycyclohexyl)ethyl]-1,1,3,3-tetramethyldisiloxane. a) Acid activation opens the epoxy ring on one end of the monomer; b) the ring opened monomer results in an alcohol termination; c) two alcohol terminated monomers react via a condensation reaction; d) an ether linkage results between the two cyclohexyl rings and a water molecule is generated; acid attack to ring open the additional epoxies may occur in this step or prior to condensation; e) a dimer with dual alcohol functionality results; f) subsequent condensation with other ring opened monomers, dimers, trimers, etc. results in a highly regular polymer with two cyclohexyl-ethyl linkages, a tetramethyl siloxane linkage, and an ether linkage.

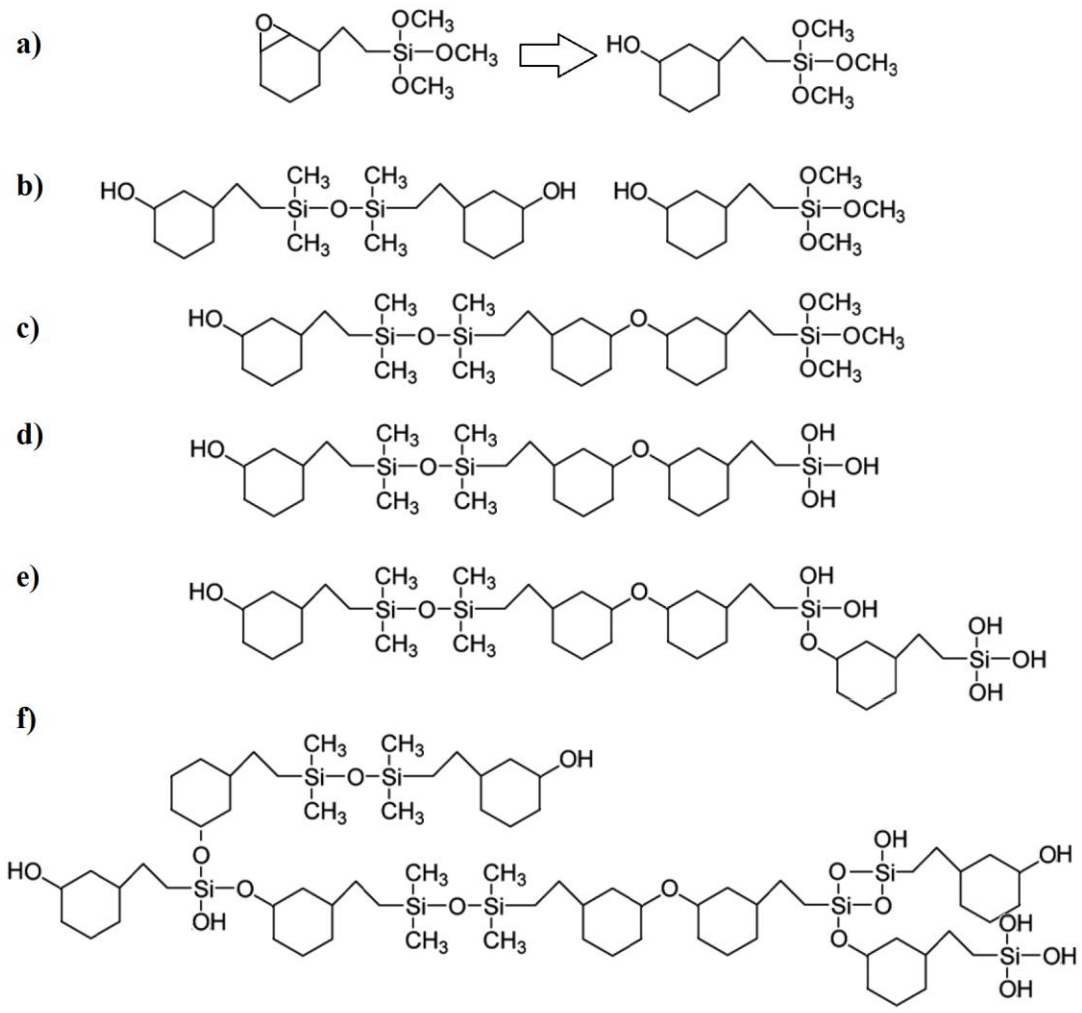

Figure 6.5. General co-polymerization scheme of 1,3-bis[2-(3,4-epoxycyclohexyl)ethyl]-1,1,3,3-tetramethyldisiloxane in the presence of (2,3)-epoxy,4-cyclohexyl ethyltrimethoxysilane. Numerous stereochemistries, varying local concentrations, and propagation schemes may occur depending on the mobility of monomers and reacted chains. The important aspect of the structure in **f)** is that increasing concentrations of (2,3)-epoxy,4-cyclohexyl ethyltrimethoxysilane will increase the density of SiO_2-like crosslinks in the material, which reduces backbone flexibility

6.3.1. Differential Scanning Calorimetry (DSC

Shown in Figure 6.6 is the DSC scan for the BECHETS in the absence of photoacid generator or diluents. Slower ramp rates of 0.5 ˚C/min and 2 ˚C/min show a gradual exotherm beginning at or above 150 ˚C while rapid heating at 10 ˚C/min resulted in a

sharp exotherm occurring at 200 ˚C. All samples exhibited a sharp crystallization peak at about 252 ˚C

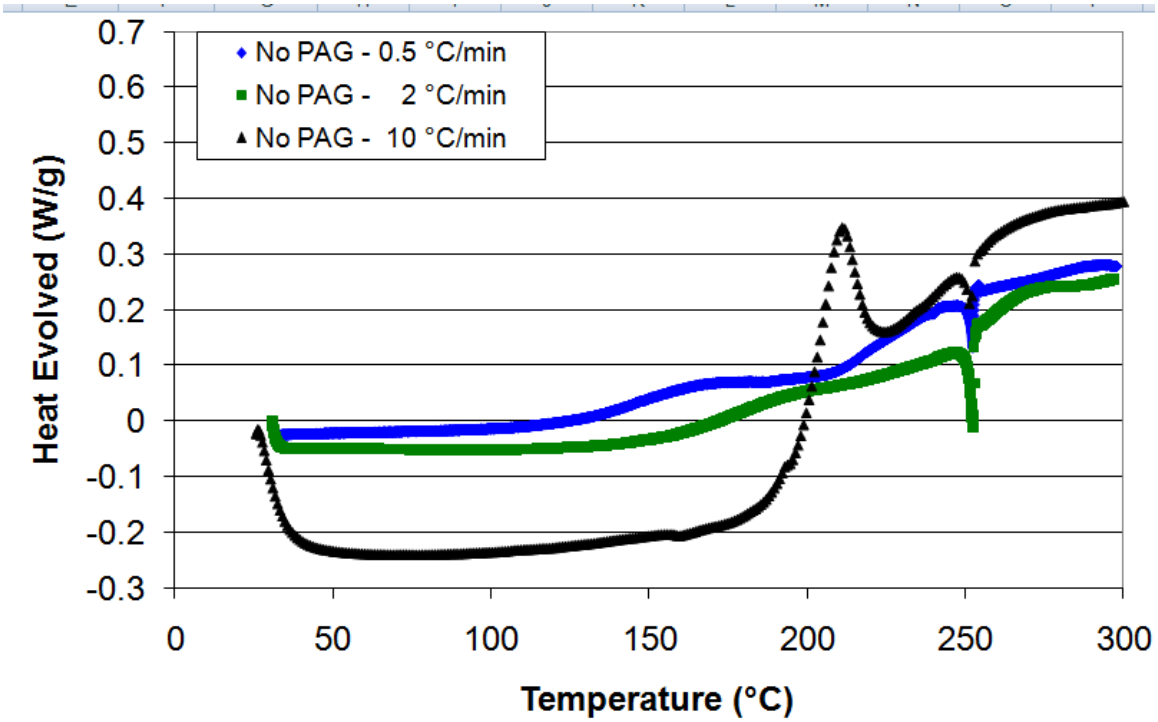

Figure 6.6. DSC scans of 1,3-bis[2-(3,4-epoxycyclohexyl)ethyl]-1,1,3,3-tetramethyldisiloxane at different heating rates. Slow heating shows the epoxy cure begins below 150 ˚C and is associated with a sharp exotherm when heated rapidly.

Shown in Figure 6.7 is the DSC scan for the BECHETS with 2.00 wt.% Rhodorsil-FABA photoacid generator. An additional exotherm is observed in these scans at about 80 ˚C at a scan rate of 0.5 ˚C/min. The exotherm at faster scan rates of 5 ˚C/min and 10 ˚C/min show a sharp exotherm near 140 ˚C. A more gradual exotherm is exhibited near 200 ˚C, similar in magnitude to the exotherms for the monomer only. All samples with PAG and no UV exposure also exhibited a sharp crystallization peak at about 252 ˚C.

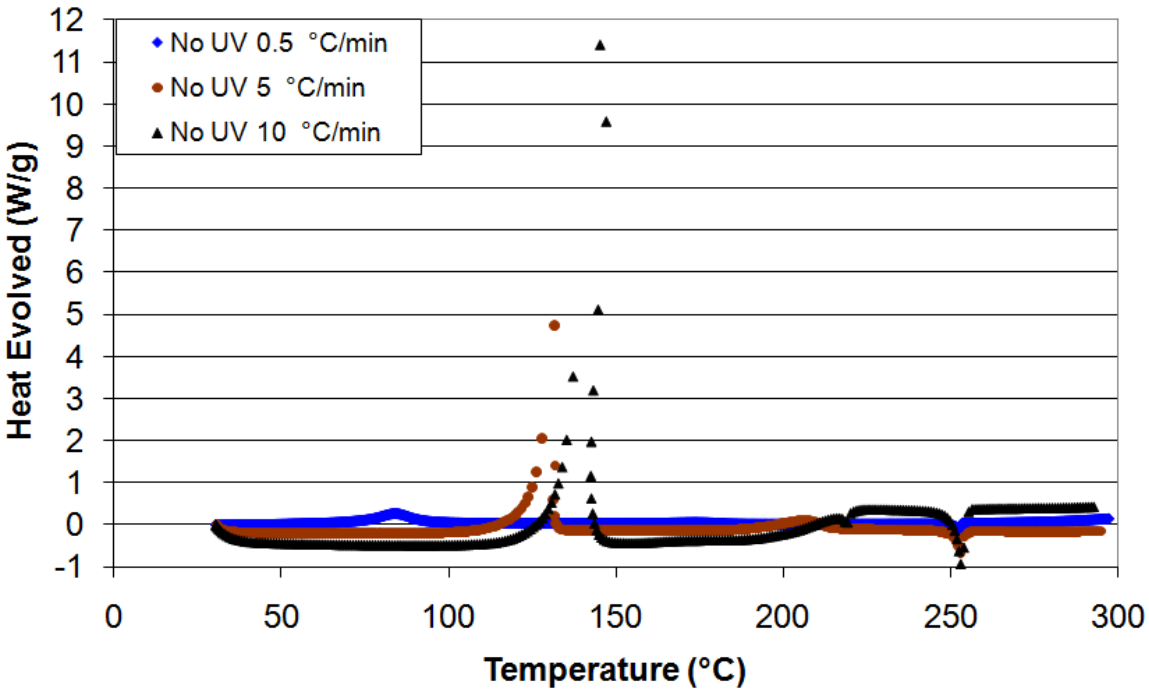

Figure 6.7. DSC scans of 1,3-bis[2-(3,4-epoxycyclohexyl)ethyl]-1,1,3,3-tetramethyldisiloxane at different heating rates. Slow heating shows the epoxy cure begins below 150 ˚C and is associated with a sharp exotherm when heated rapidly.

Shown in Figure 6.8 is the DSC scan for the BECHETS with 2.00 wt.% Rhodorsil-FABA photoacid generator irradiated with a UV exposure dose of 200 mJ/cm^2 at λ=248 nm. The amount of heat evolved at the peak of each of the lower temperature exotherms is diminished compared with the exotherm in the unexposed case. The downward slope to the curve after the low temperature exotherm is the result of open pan evaporation, likely water resulting from the condensation reaction. Samples exposed to 200 mJ/cm^2 exposure dose did not exhibit the sharp crystallization peak observed at 252 ˚C in the monomer or unexposed monomer with PAG.

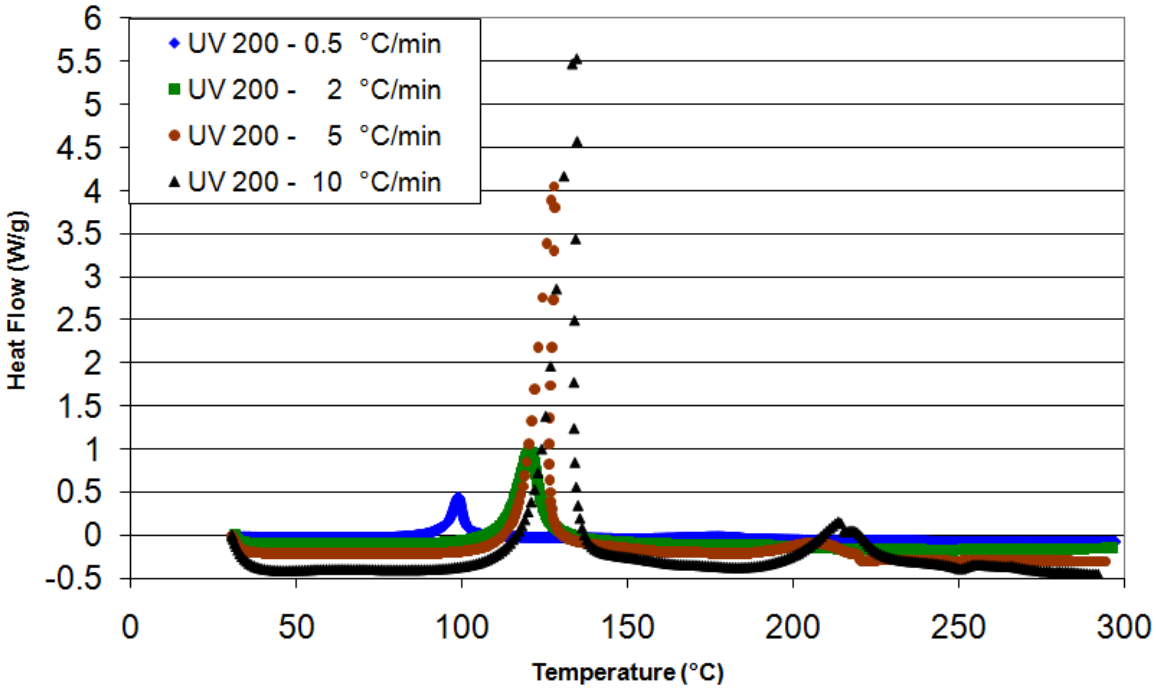

Figure 6.8. DSC scans of 1,3-bis[2-(3,4-epoxycyclohexyl)ethyl]-1,1,3,3-tetramethyldisiloxane at different heating rates. Slow heating shows the epoxy cure begins below 150 ˚C and is associated with a sharp exotherm when heated rapidly.

Shown in Figure 6.9 is the DSC scan for the 1,3-bis[2-(3,4-epoxycyclohexyl)ethyl]-1,1,3,3-tetramethyldisiloxane with 2.00 weight percent Rhodorsil-FABA photoacid generator irradiated with a UV exposure dose of 500 mJ/cm^2 at λ=248 nm. The lower temperature exotherms observed in Figures 6.7 and 6.8 for the unexposed and 200 mJ/cm^2 exposure doses is not observed at an exposure dose of 500 mJ/cm^2 at a heating rate of 0.5 ˚C/min. A slight exotherm is exhibited at higher ramp rates. An endotherm not exhibited at lower UV doses appears at the onset of the DSC scan. The downward slope is present throughout the entire curve, indicative of open pan evaporation and the crystallization peak observed at 252 ˚C reappears at this higher exposure dose. Shown in Figure 6.10 are DSC scans for 1000 mJ/cm^2, which shows nearly identical behavior to the curing of the 500 mJ/cm^2 samples.

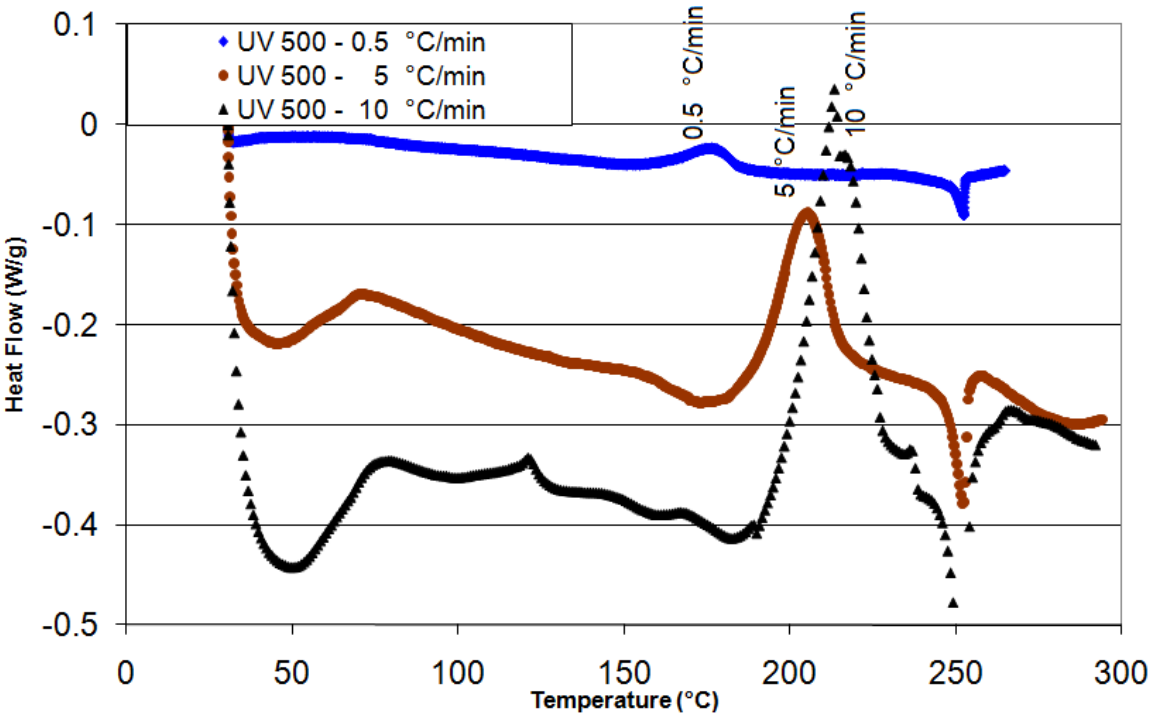

Figure 6.9. DSC scans of 1,3-bis[2-(3,4-epoxycyclohexyl)ethyl]-1,1,3,3-tetramethyldisiloxane at different heating rates. Slow heating shows the epoxy cure begins below 150 ˚C and is associated with a sharp exotherm when heated rapidly.

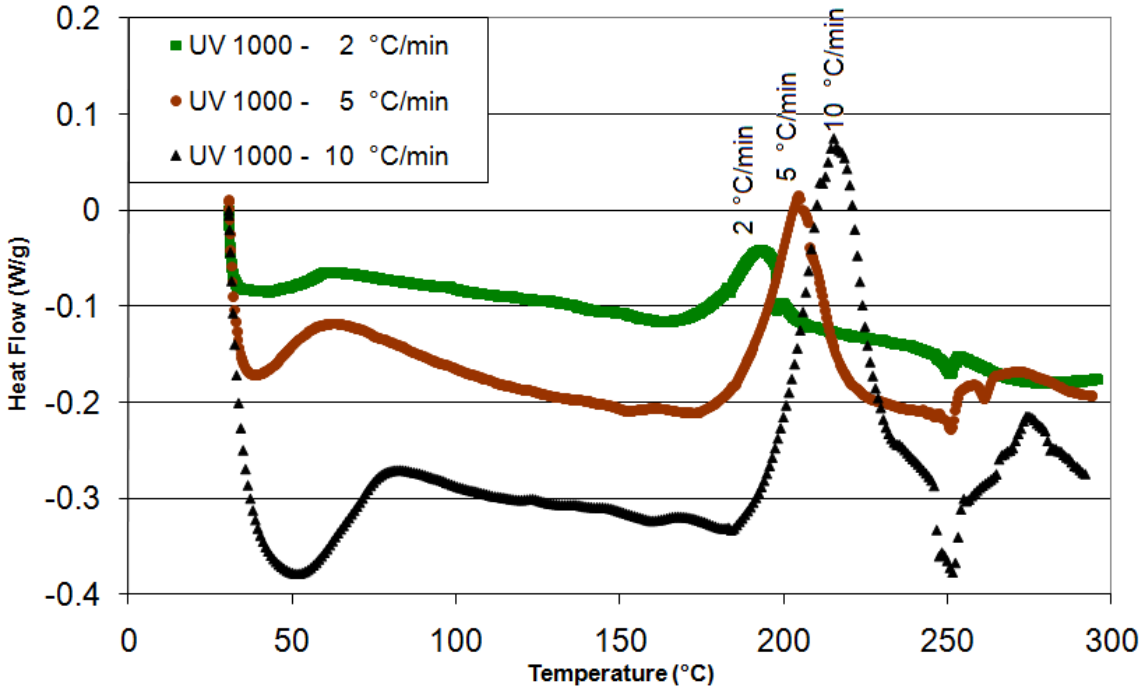

Figure 6.10. DSC scans for films of 1,3-bis[2-(3,4-epoxycyclohexyl)ethyl]-1,1,3,3-tetramethyldisiloxane for exposure doses of 1000 mJ/cm2 at increasing scan rates.

Shown in Figure 6.11 are DSC scans for the BECHETS showing the effect of increased UV dose. As was seen from comparing Figure 6.9 and 6.10, no additional change in DSC behavior was observed for UV exposure dose above 500 mJ/cm^2.

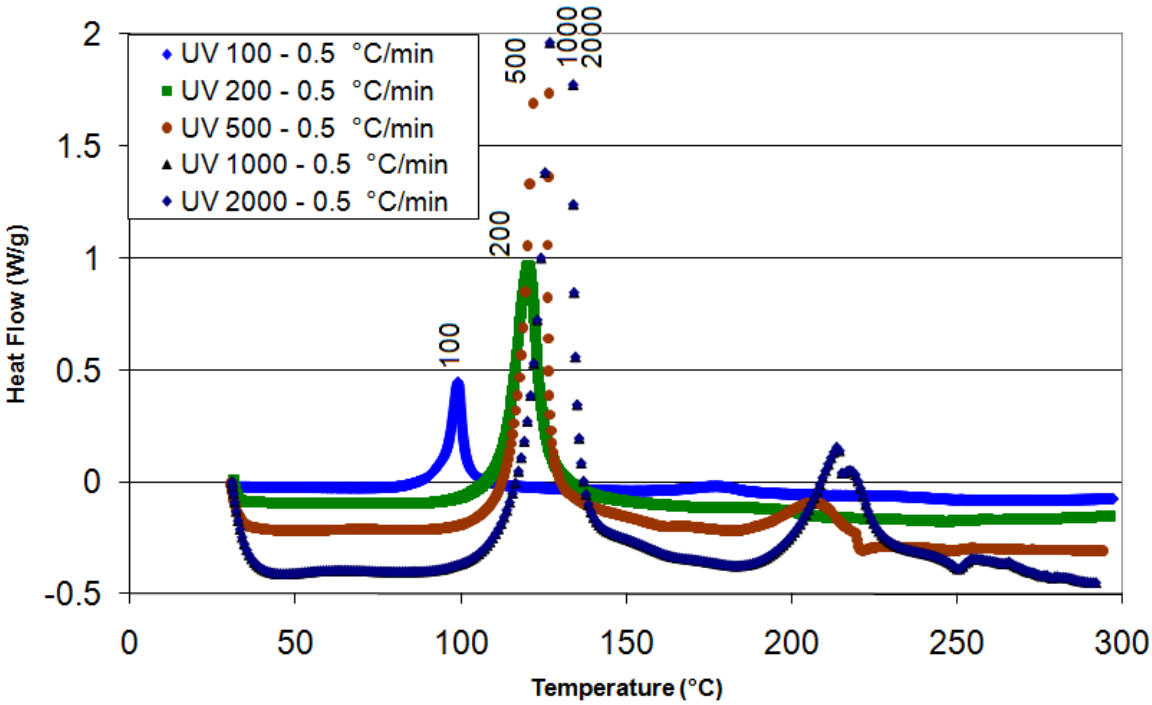

Figure 6.11. DSC scans for films of 1,3-bis[2-(3,4-epoxycyclohexyl)ethyl]-1,1,3,3-tetramethyldisiloxane for increasing exposure dose at a scan rate of 0.5 ˚C/minute.

6.3.2. Fourier Transform Infrared Spectroscopy (FTIR)

FTIR spectra for BECHETS with 2.00 wt.% Rhodorsil-FABA photoacid generator are shown in Figure 6.12. The unexposed liquid solution is compared with polymer films irradiated with ultraviolet light at λ=248 nm. Low dose (100 mJ/cm^2) and high dose (1 J/cm^2) exposures were compared before and after curing at 240 ˚C for 2 hours in a nitrogen purged quartz tube furnace.

The spectrum for the unexposed liquid exhibits an epoxide peak at 537 cm^{-1}. A slight decrease in this peak occurs after UV exposure to 100 mJ/cm^2. Curing at 240 ˚C after UV exposure eliminated the appearance of this peak. The spectrum of the higher UV exposure dose (1 J/cm^2) shows an even greater reduction in the epoxide peak but is

effectively unchanged. This suggests that with sufficient UV dose, the monomer solution is fully activated prior to heating.

6.3.3. Nanoindentation

The nanoindentation results for blends of BECHETS with ECHETS are shown in Table 6.1 and Table 6.2. The reduced modulus results averaged over three runs is shown in Table 6.1. The modulus of photopolymerized BECHETS decreases after a 2 hour cure in nitrogen at 180 ˚C. The modulus of blends with ECHETS showed a slight increase in modulus. Reduced modulus and hardness results are not available for blends of primarily ECHETS (1:2 and 0:1 B:E) because films flaked off the substrate during test. The hardness results are summarized in Table 6.2. The uncertainty reported is based on one standard deviation.

Ratio (**E) : (B)**	Run 1	Run 2	Run 3	**Average Reduced Modulus**	Uncertainty
After UV Exposure (1 J/cm^2)					
0 : 1	1.2	1.0	0.9	**1.03**	+/- 0.15
1 : 1	2.6	2.3	2.1	**2.33**	+/- 0.25
1 : 2	2.8	2.9	3.0	**2.90**	+/- 0.10
2 : 1	5.1	4.7	4.8	**4.87**	+/- 0.21
1 : 0	5.1	6.1	5.0	**5.40**	+/- 0.61
After UV Exposure (1 J/cm^2) + Cure at 180 ˚C for 2 hours in N_2					
1 : 2	0.60	0.60	0.60	**0.60**	+/- 0.00
2 : 1	2.8	2.9	2.8	**2.83**	+/- 0.15
1 : 0	3.1	3.1	3.1	**3.10**	+/- 0.00

Table 6.1: Reduced modulus for blends of photosensitive **(E)** (2,3)-epoxy,4-cyclohexyl ethyltrimethoxysilane with increasing concentration of **(B)** 1,3-bis[2-(3,4-epoxycyclohexyl)ethyl]-1,1,3,3-tetramethyldisiloxane. Each run represents an array of 25 points measured at indentation forces varying from 250 µN to 7500 µN. Uncertainty is based on one standard deviation. Blends of 0:1 and 1:1 **(E):(B)** were too brittle for measurement and flaked off the surface

Ratio (**E) : (B)**	Run 1	Run 2	Run 3	**Average Hardness**	Uncertainty
After UV Exposure (1 J/cm^2)					
0 : 1	0.04	0.03	0.03	**0.033**	+/- 0.0058
1 : 1	0.28	0.25	0.31	**0.28**	+/- 0.030
1 : 2	0.25	0.28	0.31	**0.28**	+/- 0.030
2 : 1	0.77	0.56	0.65	**0.66**	+/- 0.11
1 : 0	0.64	0.66	0.80	**0.70**	+/- 0.087
After UV Exposure (1 J/cm^2) + Cure at 180 ˚C for 2 hours in N_2					
1 : 0	0.03	0.03	0.03	**0.03**	+/- 0.00
2 : 1	0.48	0.51	0.46	**0.48**	+/- 0.025
1 : 2	0.51	0.48	0.46	**0.48**	+/- 0.025

Table 6.2: Hardness after UV exposure to 1 J/cm^2 reduced by the Oliver-Pharr method for blends of photosensitive **(E)** (2,3)-epoxy,4-cyclohexyl ethyltrimethoxysilane with increasing concentration of **(B)** 1,3-bis[2-(3,4-epoxycyclohexyl)ethyl]-1,1,3,3-tetramethyldisiloxane. Each run represents an array of 25 points measured at indentation forces varying from 250 µN to 7500 µN. Uncertainty is based on one standard deviation. Blends of 0:1 and 1:1 **(E):(B)** were too brittle for measurement and flaked off the surface

Ideal calibration materials should have a modulus and indentation depth near that of the sample under investigation. However, because the hybrid glass polymer blends investigated in this study ranged from rubbery to glassy in nature, all results are reported using a quartz standard for uniformity. A polymerized film of BECHETS was indented after calibration with a polycarbonate standard with a modulus of 3.1 GPa. This sample exhibited a slightly higher modulus (1.8 GPa) than observed with quartz calibration, but the drift rate was high, suggesting this may actually overestimate the reduced modulus of this material. More extensive study of polynorbornene based epoxies found that calibration with quartz overestimated the reduced modulus and hardness[119], so the values in Table 1.1 and Table 1.2 should be seen as upper limits at best and the true values of reduced modulus and hardness are likely somewhat less than reported here.

6.3.4. Photopatterning and Plasma Etching

Photopatterning of features as small as 80 μm by 120 μm was achieved by non-contact UV exposure of 1 J/cm^2 through a quartz mask. Smaller features were removed upon rinsing with isopropyl alcohol, suggesting inadequate adhesion to the substrate. Smaller feature sizes might be achievable by contact exposure or by increasing the UV dose, but may be limited by adhesion.

Plasma etching of photocured films of BECHETS exposed to 1 J/cm^2 showed widely varying etch rates. The etch rate was measured to be between 0.25 μm/min and 0.35 μm/min. However, attempts to more accurately measure this etch rate by using longer etch times failed because the film did not etch consistently. This is likely because the organic domains were etching faster than the inorganic domains due to the high oxygen content plasma. Higher concentrations of CHF_3 could improve the etch rate of the inorganic portion but were not attempted because high oxygen content plasmas are needed to remove organic sacrificial materials protected by the photodefined glass.

6.3.5. Air Cavity Formation

Attempts to decompose poly(propylene carbonate) overcoated with BECHETS were successful and the decomposition products were able to permeate through the overcoat. However, the resulting air cavities were collapsed because the overcoat was not rigid enough to support itself over the structure. Deformation of polynorbornene due to rapid volatilization of decomposition products from poly(propylene carbonate) has been documented during air cavity formation but can be eliminated by decreasing the heating rate. Given the slow heating rate employed to decompose the sacrificial material in this

study (1 ˚C/min), it is likely that no significant deformation occurred, but rather the overcoat was too soft and/or not thick enough to support itself over the air cavity.

6.3.6. Processing Variations

Additional processing techniques were attempted to form thin films of BECHETS. Increasing spin speed to decrease film thickness was unsuccessful because the droplets of monomer formed on the wafer surface, resulting in some regions with no polymer film. Dilution with isopropanol exacerbated this problem, especially at low monomer concentrations (8.00%). Solutions with 33.3% monomer concentrations formed thin films ~20 um thick when solvent was evaporated at room temperature. However, these films easily cracked and flaked off the wafer surface when heated. Dilution of base monomers may also terminate polymer chains by reacting with epoxy groups. Decreased polymerization rates have been reported for difunctional epoxies with diols [120], although this may depend on the initiator[113]. Ethoxy groups are also reactive in the presence of species with labile hydrogens, such as alcohols[121], which is likely also responsible for the brittle nature of dilute films of ECHETS.

The liquid nature of the monomer solution makes it undesirable for many microelectronic applications because a photomask cannot be placed in contact with the film. Cooling the monomer below 0 ˚C turned the solution milky white and resulted in an increased viscosity. Freezing the monomer was not possible due to experimental setup and is not viable for production applications. Although photocurable liquid solutions of inorganic-organic hybrid glasses are desirable for a variety of applications, they are of little interest for microelectronics applications because of the inability to put a mask into contact with the film.

6.4. Conclusions

Polymer films created from BECHETS photosensitized with 2.00 wt.% Rhodorsil-FABA photoinitiator were reported. The DSC data indicate the epoxide curing reaction is initiated with UV exposure and the exotherm peak temperature is lowered compared with the unexposed solution. The exotherm associated with the curing reaction is significantly reduced in intensity at higher doses because the reaction is nearly completed prior to heating. The exotherm in this case may occur prior to loading into the chamber and/or during nitrogen purging of the chamber.

FTIR data indicate alcohol peaks after UV exposure, consistent with the activation of epoxy functionalities. Following heating, the OH peaks decay and C=O peaks appear, suggesting that the epoxy cure is complete but that degradation of the backbone has also occurred. The source of the oxygen is unclear, but may come from dissolved oxygen in the matrix, residual oxygen in the DSC chamber, or result from the polymer itself. This degradation at 240 ˚C limits application for some air cavity processes because decomposition at or near these elevated temperatures is required for extended periods (one or two hours). The oxidative degradation with even mild heat (60 ˚C) after nitrogen cure also limits its application for optical applications.

The inability to tune the film thickness by increasing spin speed or diluting with isopropyl alcohol is a critical limitation photosensitive formulations of BECHETS for air-cavities in microelectronics. Improved performance of the material might be achieved by surface reaction with the sacrificial polymer. The photoacid used in this study is commonly used for photosensitive formulations of poly(propylene carbonate) and thus acid from the sacrificial material might be capable of activating and diffusing into a thin layer of the resultant glass. This would enable a barrier layer which is substantial thinner

and could be used as a chemical barrier layer, but the use might be limited, because additional layers would be required to provide structural support needed for larger air cavities.

The liquid nature of the BECHETS precludes its use with contact mask alignment, further limiting its applicability. Solid polymer films are required for these applications. Overcoat materials of inorganic-organic hybrids must be able to satisfy the requirements of solidification prior to photo exposure, ability to tune the spin speed thickness, and must be easily removed by plasma or chemical etchants. The superior etch resistance coupled with the failure to solidify or tune film thickness severely limit films of BECHETS. Inorganic-organic hybrids based on polyoctohedral silsesquioxane (POSS) will be preferable for microelectronics applications because they more closely match the needs for photopatterning and film thickness.

7. AIR CAVITY TRANSMISSION LINES FOR OFF-CHIP INTERCONNECTS CHARACTERIZED TO 40 GHZ

7.1. Introduction

Power consumption, bandwidth, and latency in microprocessors have become the critical metrics for evaluating design performance in both high performance (energy costs) and mobile applications (limited power budget). Multi-core designs minimize energy, waste heat, and delay. Chip stacking techniques such as memory-on-die are also attractive because of reduced wire length and delay. However, the number of cores and memory layers will be constrained by power delivery, via aspect ratio, wiring density, and thermal limitations[122]. Ultimately, the chip/stack must communicate with package level components.

External links are required for chip-to-memory, chip-to-chip, and chip-to-network communication. On-chip and off-chip I/O consume greater than half the chip power and this percentage is expected to increase at future technology nodes. The ITRS has singled out off-chip wires, stating, "a key bottleneck to the realization of high-performance microelectronic systems is the lack of low-latency, high-bandwidth, and high density off-chip interconnects. Some of the challenges in achieving high-bandwidth chip-to-chip communication using electrical interconnects include the high losses in the substrate dielectric, reflections and impedance discontinuities, and susceptibility to crosstalk [1]."

Off-chip wires represent a particular challenge due to long routing distances which are orders of magnitude longer than on-chip wires. The long pathway degrades the electrical field strength, requiring higher power transmission and/or receiving ends.

Optical interconnects are superior for longer distances (tens of meters) but electrical interconnects are preferred at the package level for electrical performance and ease of integration[123-125]. Package and board level interconnects must have high bandwidth, consume low power, and have low loss in the line and transmission circuitry.

7.1.1. Air gap interconnects

Air gaps have been reported to lower capacitance and reduce RC delay for on-chip interconnect applications. On-chip air-gaps have been reported previously by Kohl *et al*.[126] as well as numerous other researchers [16],[127-128]. Off-chip transmission lines with an air-gap have also been previously reported on fiberglass-epoxy[44] and semiconductor substrates[129-131].

This work describes an expansion and improvement over previously reports of air-gap transmission lines on organic substrates. [44] The current work describes air cavity lines with a homogenous air dielectric layer fabricated using a low residue sacrificial polymer and a higher modulus overcoat. A homogenous dielectric eliminates phase offset and allows true TEM operation. The photoacid generator, the primary residue after decomposition and the PAG concentration has been minimized to reduce residue after decomposition. The higher modulus overcoat improves structural integrity and allows sacrificial decomposition with less deformation in the overcoat.

The low-loss board-level signal lines with an air cavity dielectric presented here will be required for future package generations because of the need for high quality electrical pathways. Inclusion of the air cavity drastically reduces capacitance and loss tangent critical metrics in the evaluation of dielectric performance. S-parameter

measurements reported here include S_{21} loss of less than 10 dB at 40 GHz for a 5.8 cm line.

7.2. Background

Power consumption in off-chip interconnects is best understood by analyzing loss contributions in a signal line. The electric field decays with line length, operating frequency, and electrical characteristics of the line.

7.2.1. Electric field strength decay

The field strength of an electromagnetic wave propagating in the +z direction is expressed in Equation 7.1.

$$E|_{z+} = E_0 \cdot \exp(-\gamma \cdot l) \qquad 7.1$$

where E_0 is the initial electric field strength, γ is the decay factor, and l is the line length. For an off-chip interconnect, these are analogous to signaling voltage, electrical pathway characteristics, and data channel length.

7.2.2. RLGC distributed element model

While E_0 and l are constrained by electrical design and physical layout, γ depends on the material properties of the transmission line. Resistance (R) and inductance (L) depend on conductor properties while shunt conductance (G) and capacitance (C) depend on dielectric properties. These loss contributions may be visualized by a distributed element RLGC model, as shown in Figure 7.1. Low resistivity conductors (e.g. copper) are already in use, leaving G and C as the circuit elements in need of improvement (i.e. dielectric performance).

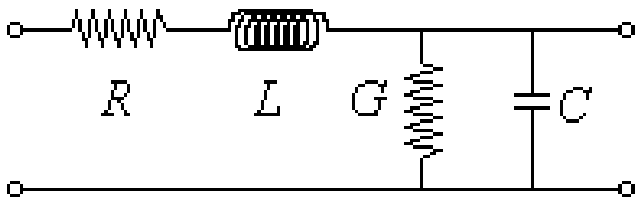

Figure 7.1 Distributed element representation of transmission line structure. Resistance (R) and inductance (L) depend on conductor properties while conductance (G) and capacitance (C) depend on dielectric properties.

The contributions of RLGC components in Figure 7.1 can be expressed for use in Equation 7.1 and separated into real and imaginary parts as shown in Equation 7.2.

$$\gamma = \sqrt{(R + j\omega L)(G + j\omega C)} = \alpha + j\beta \qquad 7.2$$

where R (W/m), L (H/m), G (S/m), and C (F/m) are the circuit elements, ω is the angular frequency ($2\pi \cdot$frequency), and j is $\sqrt{-1}$. α is the sum of attenuation due to conductor (α_c) and dielectric losses (α_d) and β is the phase constant.

For a parallel plate line, the conductor loss α_c (in Neper/m) is expressed in Equation 7.3.

$$\alpha_c = \frac{\sqrt{\frac{\omega \mu_0 \varepsilon_r}{2\sigma\mu_r}}}{\eta_0 d} \qquad 7.3$$

where μ_0 is the permeability of free space, ε_r is the relative permittivity, σ is the conductivity of the metal, μ_r is the relative permeability, η_0 is the characteristic impedance of free space (377 Ω), and d is the separation distance between conductors

(dielectric thickness). The relationships relating α_c to surface roughness can be expressed by

$$\alpha_c' = \alpha_c \cdot \left(1 + \frac{2}{\pi} \cdot \arctan 1.4 \left(\frac{\Delta_{rms}}{\delta} \right)^2 \right) \qquad 7.4$$

where δ is the skin depth in the conductor and Δ_{rms} is the root mean square surface roughness.

The dielectric loss α_d (in Neper/m) in a parallel plate line is expressed in Equation 7.5.

$$\alpha_d = \frac{\omega \sqrt{\mu_r \varepsilon_r} \tan \delta}{2c} \qquad 7.5$$

Where tan δ is the loss tangent of the dielectric and *c* is the speed of light *in vacuo*.

The phase loss in Equation 7.2 is expressed by the phase constant β (in rad/m) in Equation 7.6.

$$\beta = \frac{\omega \sqrt{\varepsilon_r}}{c} \qquad 7.6$$

Thus, by knowing the phase loss, a relative dielectric constant can be inferred using Equation 7.6.

Comparing Equations 7.3, 7.4, and 7.5 reveals a square root dependence on relative permittivity in all three loss mechanisms. Conductor loss (Equation 7.3) depends on square root of frequency while dielectric loss (Equation 7.4) varies linearly with frequency. Because of this relationship, dielectric loss becomes the dominant loss mechanism at multi-GHz frequencies and is strongly dependent on tan δ. Expressions for microstriplines and striplines show similar qualitative behavior.

7.2.3. Transmission line characterization

Two-port S-parameters are ideal for evaluating transmission line performance because S21 is the ratio of the output voltage (port 2) relative to the input (port 1). This is essentially the electric field decay as expressed in Equation 7.1. For a fixed line length, the slope of S21 vs. frequency indicates channel quality because it expresses the power penalty for higher frequency operation and/or wire length. Careful calibration is required to eliminate loss and reference plane shift from probe pads and cables[20]. Probe pad capacitances are not subtracted here because the lines are long and probe pad capacitance is a fraction of the total capacitance. The elements of the scattering matrix can also be converted into RLGC elements or the ABCD matrix for circuit modeling and energy per bit calculations [132].

Capacitance, loss tangent, and S-parameter measurements are used in this paper to characterize the performance of air-cavity transmission lines on FR4 substrates. Dielectric properties were evaluated using capacitance and loss tangent measurements during processing at 100 kHz. The capacitance measurement evaluates C, as shown in Figure 7.1, while the loss tangent measurement evaluates G. S-parameters measure the decay of the signal expressed in Equation 7.1 and show line performance as a function of operating frequency.

7.3. Board Fabrication Process

Transmission lines separated only by an air dielectric were fabricated on FR-4 substrates. The process flow for air cavity formation is summarized in Figure 7.2. A seed layer was sputtered and electroplated to pattern ground line structures. The sacrificial polymer was photopatterned to define the air cavity region. Signal lines were sputtered

and electroplated on top of the sacrificial polymer. The structure was encapsulated with an overcoat polymer. In the final step, the structure was heated to 220 ˚C, decomposing the sacrificial material and generating the air cavity.

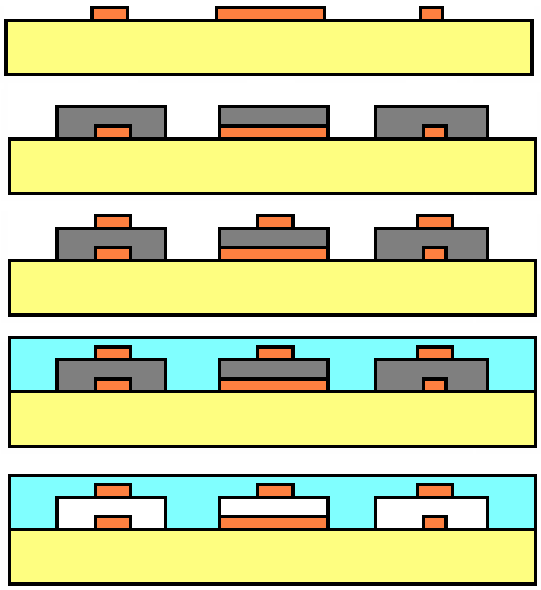

Figure 7.2 Flow diagram of air-cavity line buildup process. Ground lines are patterned on an FR4 substrate. The sacrificial polymer is patterned over the ground line. The signal line is built on the sacrificial layer. The structure is overcoated with a rigid polymer. The sacrificial material is decomposed.

The as-received substrates from Isola were pre-clad in 1 oz. copper (35 μm thick) on both sides of the board. The pre-clad copper was etched with a solution of sulfuric acid and hydrogen peroxide to remove all exposed copper. The bare substrate remained for the air-cavity transmission line buildup process.

An electroplating seed layer of Ti/Cu/Ti was deposited by sputtering in a CVC DC sputterer. The Ti layers were added to promote adhesion of copper to the substrate (bottom Ti layer) and photoresist to the seed layer (top Ti layer). The Ti layers were 200 Å thick while the Cu layer was 500 Å thick.

The electroplating pattern for ground lines was defined by spincoating AZ4620 photoresist to a thickness of 10 μm and photopatterning by UV exposure at λ=365 nm. After photoresist patterning of the Ti adhesion layer was removed with buffered oxide etch (6:1 NH_4OH:HF) to expose the copper surface for electroplating.

The ground line was electroplated in a bath of 60 g of copper sulfate, 60 mL of sulfuric acid, 1000 mL deionized water, 0.25 g of bis-sodium sulfopropyl disulfide (SPS), and 0.25 g of polyethylene glycol (molecular weight 4,000 g/mol). The bath was well stirred and nitrogen was bubbled into the bottom of the bath to promote hydrogen desorption (formed during the plating process). The board surface was plated at a current density of 10 mA/cm^2 (based on open area in electroplating mask). A large, high purity copper anode was used as the source and an electrode was attached to the seed layer at the edge of the board. Ground lines were electroplated to a thickness of between 10 μm to 12 μm as there was variation across the board surface due to the single electroplating contact. 4-point probe measurements showed the resistivity close to bulk copper. After electroplating, the photoresist and seed layers were stripped.

The sacrificial polymer poly(propylene carbonate) (PPC) was spincoated to a thickness of 40 μm was sensitized with 2.0 wt.% Rhodorsil-FABA photoacid generator, capable of photopatterning PPC cleanly but leaving low residue after decomposition. The sacrificial layer was photopatterned using a dry develop technique[8].

The signal lines were patterned by sputtering a seed layer over the PPC and connecting to the probe pad. The lines were electroplated using AZ4620 as the electroplating mask and the same plating conditions as the ground line. Signal line thickness varied between 10 μm and 12 μm thick on the PPC. Initial measurements of

capacitance and loss tangent were taken at this point.

The overcoat polymer was a functionalized polynorbornene, Avatrel 8000P. The overcoat was spincoated over the structures and photopatterned to expose probe pads. The overcoat influence on loss tangent and capacitance was measured at this point. The final Avatrel film thickness was approximately 85 μm on the board and 60 μm over the sacrificial polymer and signal lines. The elastic modulus of the Avatrel 8000P was approximately 3.0 GPa after cross-linking, compared with the lower modulus of Avatrel 2000P (1.0 GPa), which was used as an overcoat material in Chapter 4.

In the final process step, the sample was decomposed at 220˚C in a 6" diameter quartz tube oven purged with nitrogen at a flowrate of 10 L/min. The sample was heated at 3˚C/min to 150˚C and held for 30 minutes prior to ramping at 1˚C/min to 220˚C and a dwell of 2 hours. The sample was cooled back to room temperature and then analyzed by capacitance, loss tangent, and S-parameters.

7.4. Measurements

Capacitance measurements at 100 kHz were taken at different points during manufacture using an HP4263A LCR meter with 2 μm tungsten probe tips. Capacitance between signal and ground was measured before overcoat, after overcoat, and after decomposition of the sacrificial polymer. Loss tangent was also measured during processing as it can be related to shunt conductance G.

S-parameters were measured using an Agilent e8363b PNA series network analyzer using Cascade Microtech ACP-50 GSG probes with 250 μm pitch. Data were measured from 10 MHz to 40 GHz with 25 MHz spacing over a total of 1601 scans. An SOLT calibration was performed prior to measurement.

7.5. Results

Air cavity transmission lines with various ground plane widths were fabricated, electrically characterized, cross-sectioned and imaged. Figure 7.3 shows a labeled cross-section of an air cavity line with 150 μm wide ground line. The labeled components include the fiberglass-epoxy board, the Avatrel overcoat, the air cavity region, and the ground and signal lines.

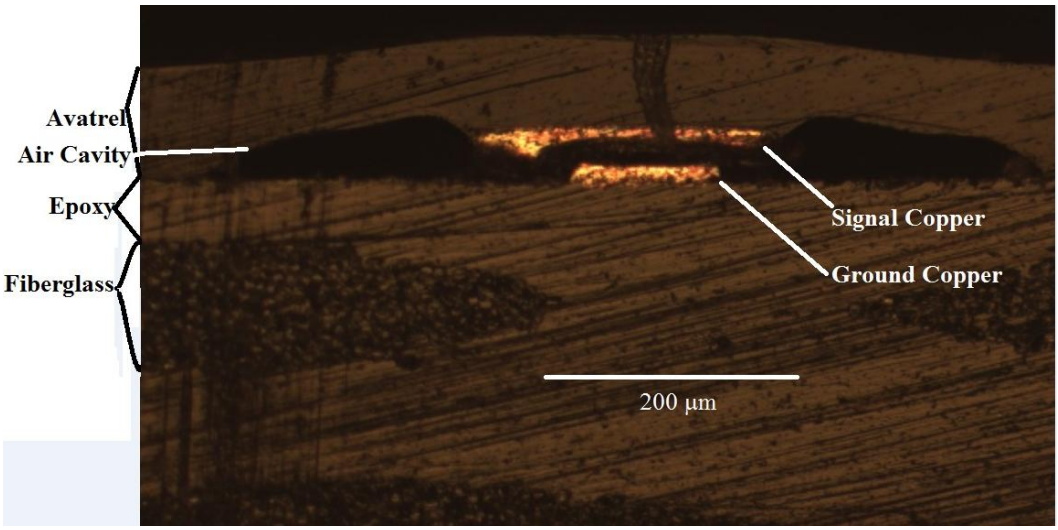

Figure 7.3 Chemical structure of 1,3-bis[2-(3,4-epoxycyclohexyl)ethyl]-1,1,3,3-tetramethyldisiloxane

Figure 7.4 shows an unlabeled cross-section of a second 150 μm wide ground line. Figure 7.5 shows a cross-section of an air cavity parallel plate line with 220 μm wide ground line. Figure 7.6 shows a cross-section of an air cavity line with 650 μm wide ground line. The ground on the right side was removed by the cross-section process but extends the full width of the cavity in the structures.

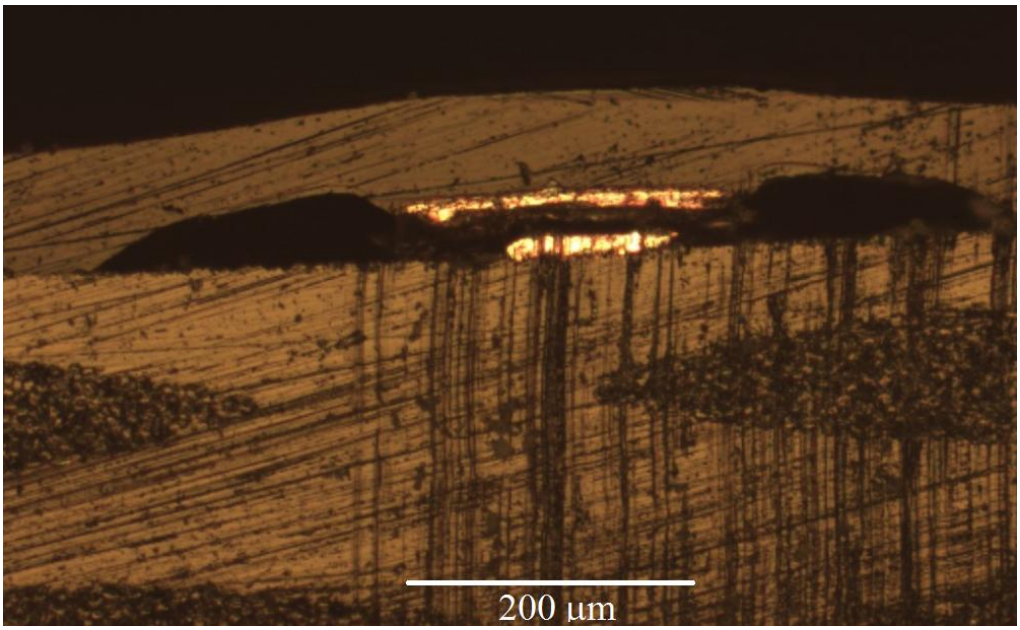

Figure 7.4 Chemical structure of 1,3-bis[2-(3,4-epoxycyclohexyl)ethyl]-1,1,3,3-tetramethyldisiloxane

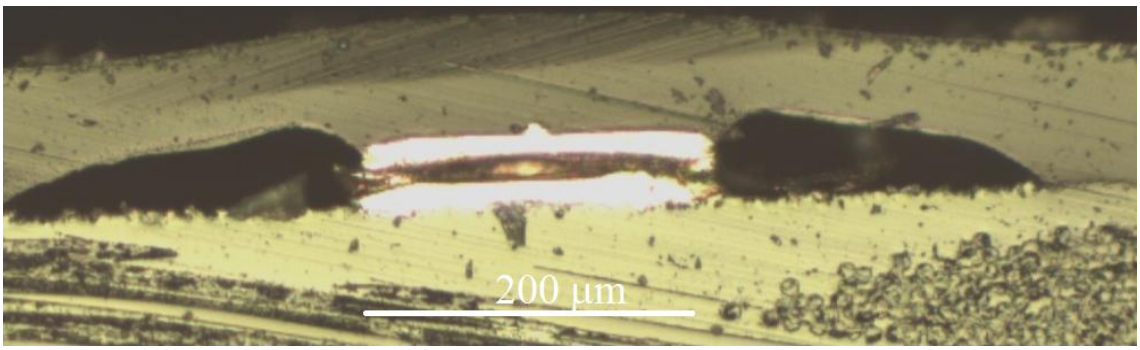

Figure 7.5 Optical microscope image of 220 µm wide ground line

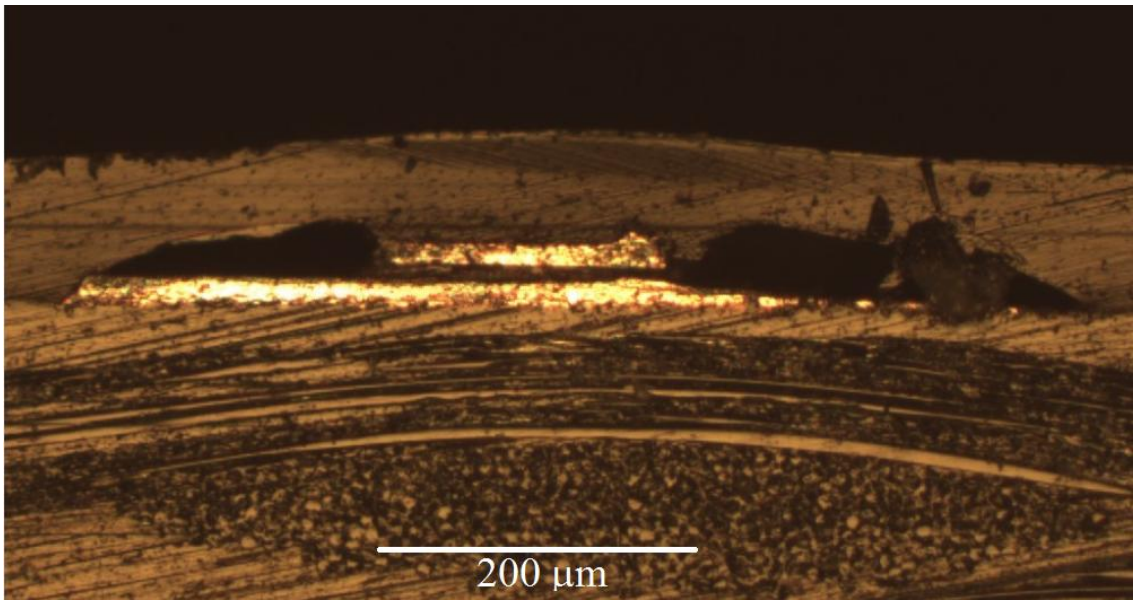

Figure 7.6 Optical microscope image of 650 μm wide ground line. Part of the ground on the right side is obscured by a dicing defect.

The capacitance measurements at 100 kHz for the different processing stages are given in Table 7.1. The wide ground structures gave the highest capacitance at all stages of fabrication. The capacitance increased after Avatrel overcoat because the microstripline now has Avatrel over top rather than air. After overcoat, the capacitance is higher, like that of a buried line, because it is surrounded by higher permittivity materials. Following air cavity formation, the capacitance was reduced to near or below the initial value before overcoat.

Ground Line Width (μm)	Before Overcoat (pF)	After Overcoat (pF)	After Sacrificial Decomposition (pF)
650	10.23	15.03	10.07
	10.25	15.20	12.81
	10.25	15.16	10.75
220	9.02	12.83	8.38
	9.14	13.06	10.32
	8.93	12.88	9.41
	9.07	13.07	9.11
150	6.84	9.30	6.55
	6.93	9.11	5.82
	6.96	9.11	5.91
	7.09	9.21	7.75
	7.11	9.19	7.20

Table 7.1 Capacitance measurements during processing at 100 kHz.

The loss tangent measurements at 100 kHz at points throughout processing are given in Table 7.2. Measurements show the same general trend as the capacitance during processing. An important feature of Table 7.2 is the loss tangent after decomposition is only 10% of the value for the overcoated line. This is due to the presence of the air cavity rather than polymer. Air has essentially zero loss tangent, which greatly reduces the contribution of α_d defined in Equation 7.4.

Ground Line Width (μm)	tan δ Before Overcoat	tan δ After Overcoat	tan δ After Sacrificial Decomposition
650	0.0176	0.0487	0.0077
	0.0183	0.0496	1.3724
	0.0187	0.0503	0.0087
220	0.0187	0.0495	0.0064
	0.0187	0.0494	0.0061
	0.0196	0.0504	0.0059
	0.0193	0.0498	0.0057
150	0.0553	-	0.0146
	0.0229	0.0444	0.0063
	0.0193	0.0438	0.0057
	0.0188	0.0423	0.2356
	0.0197	0.0418	0.1647

Table 7.2 Loss tangent measurements during processing. All measurements taken at 100 kHz.

The values of S21 for the 150 μm wide ground lines are shown in Figure 7.7. Lines with lower capacitance show lower loss across the entire frequency range. Figure 10 shows the measured values for S11 for the 150 μm wide ground lines. The resonance is due to waveguide length being equal to multiples of λ/2 at each resonant wavelength.

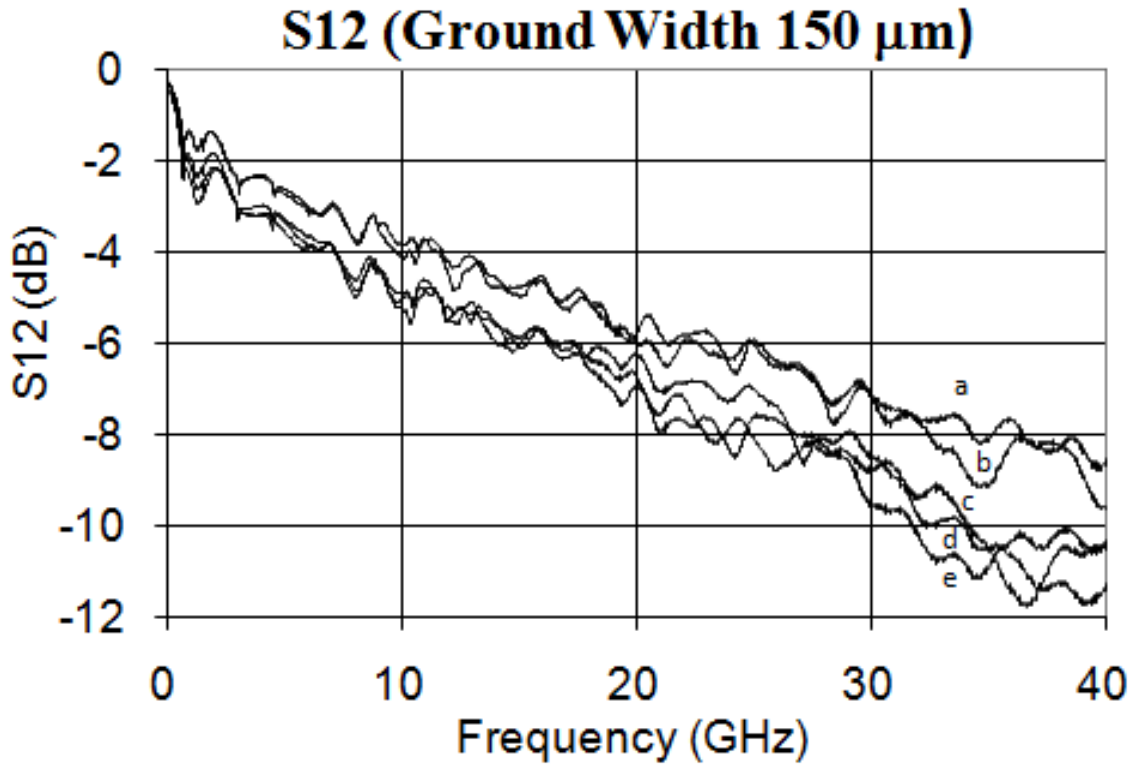

Figure 7.7 S21measurements for 150 µm wide ground lines

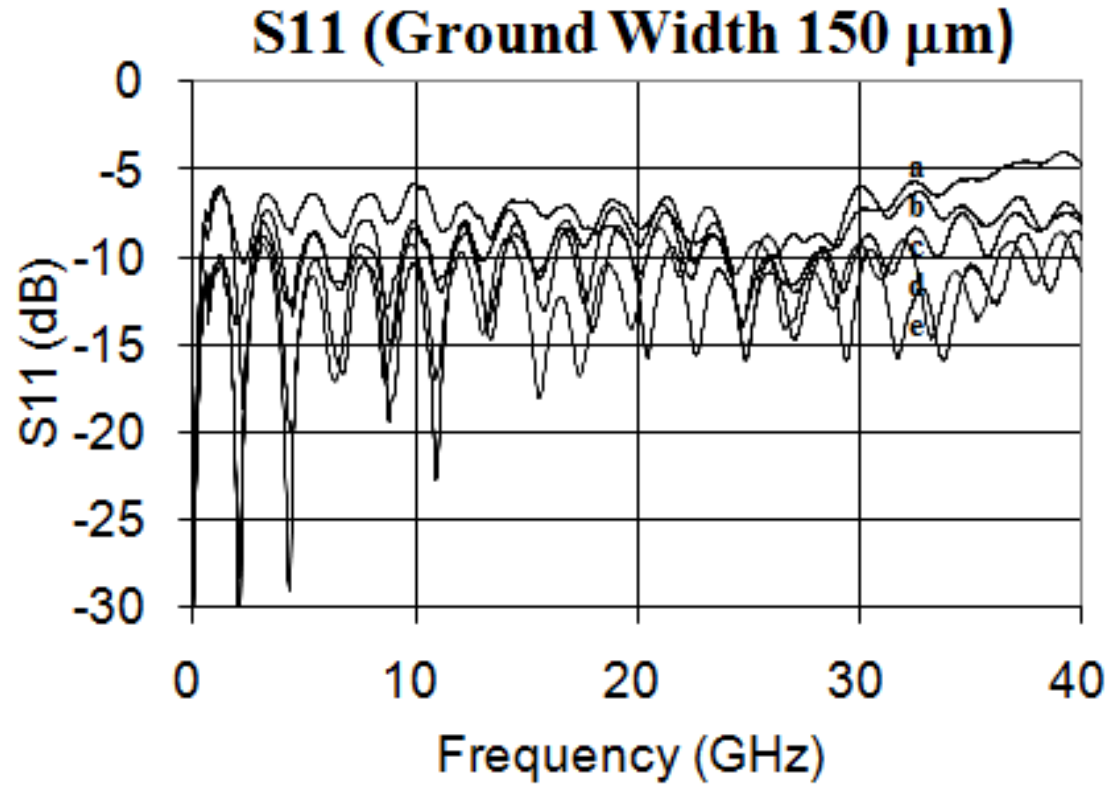

Figure 7.8 S11measurements for 150 µm wide ground lines

The measured values of S21 for parallel plate lines (220 μm wide ground lines) are given in Figure 7.8. These lines did not exhibit as clear a trend with capacitance as the 150 μm wide ground lines did. Figure 7.11 shows the measured values for S11 for the parallel plate lines. The resonant wavelengths are also multiples of λ/2 and are nearly the same as the narrow ground line structures.

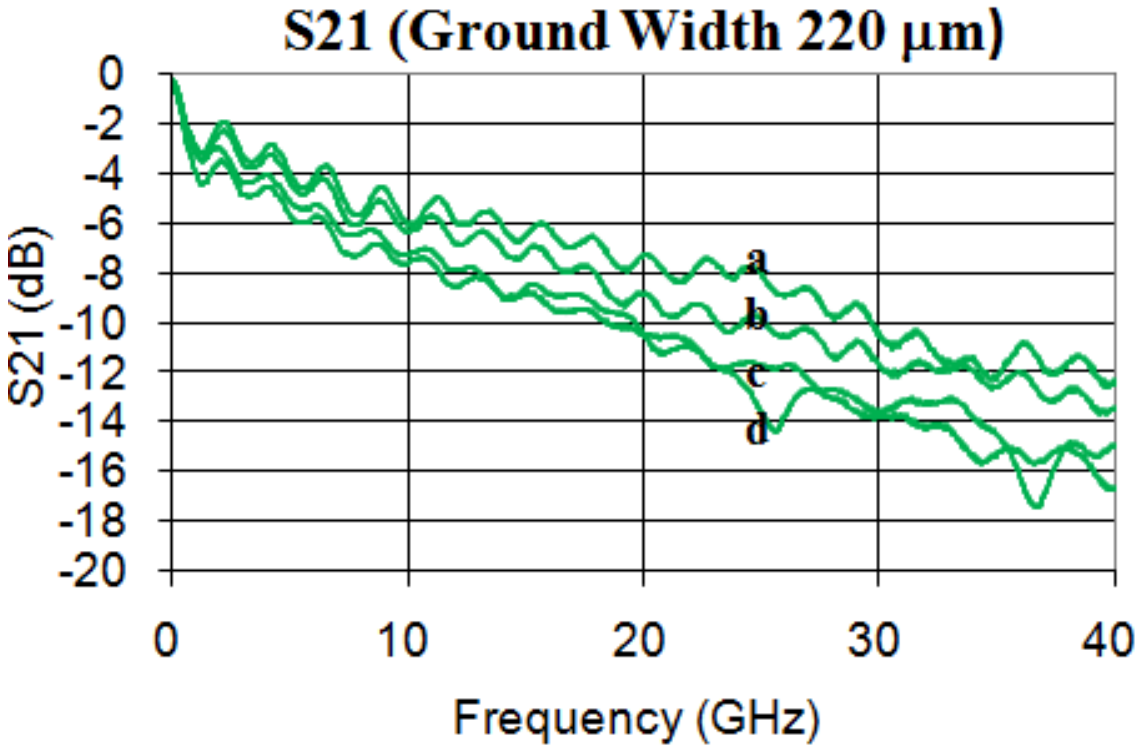

Figure 7.9 S21measurements for 220 μm wide ground lines

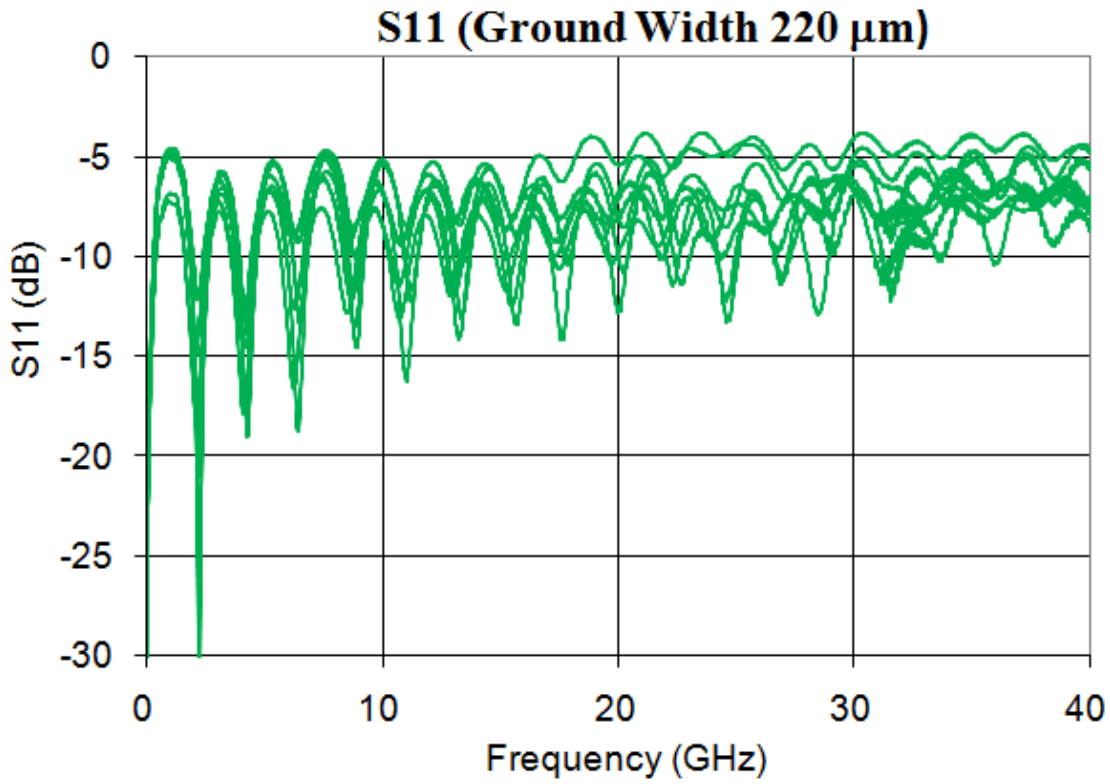

Figure 7.10 S11measurements for 220 μm wide ground lines

The measured values of S21 for the 650 μm wide ground lines are shown in Figure 7.9. The line which had shown anomalously high capacitance and loss tangent at 100 kHz exhibits a sharp increase in attenuation between 20 GHz and 30 GHz. The measured values for S11 for the 650 μm wide ground lines are shown in Figure 7.12.

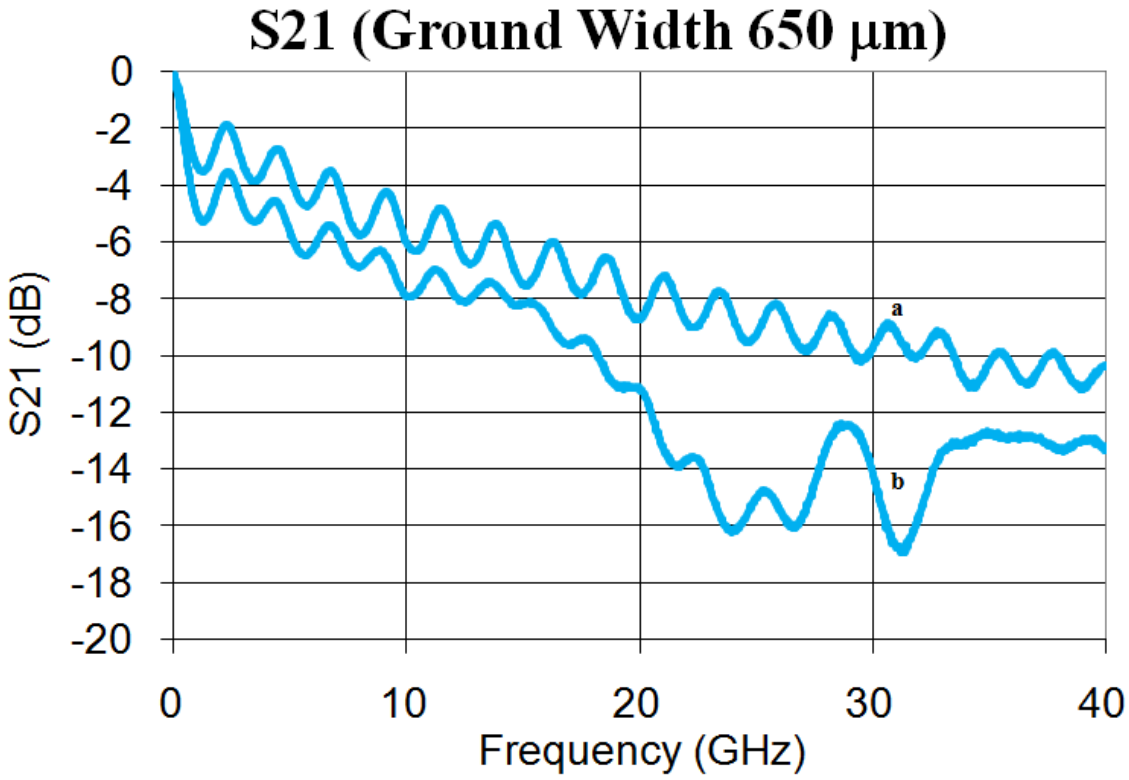

Figure 7.11 S21measurements for 650 µm wide ground lines

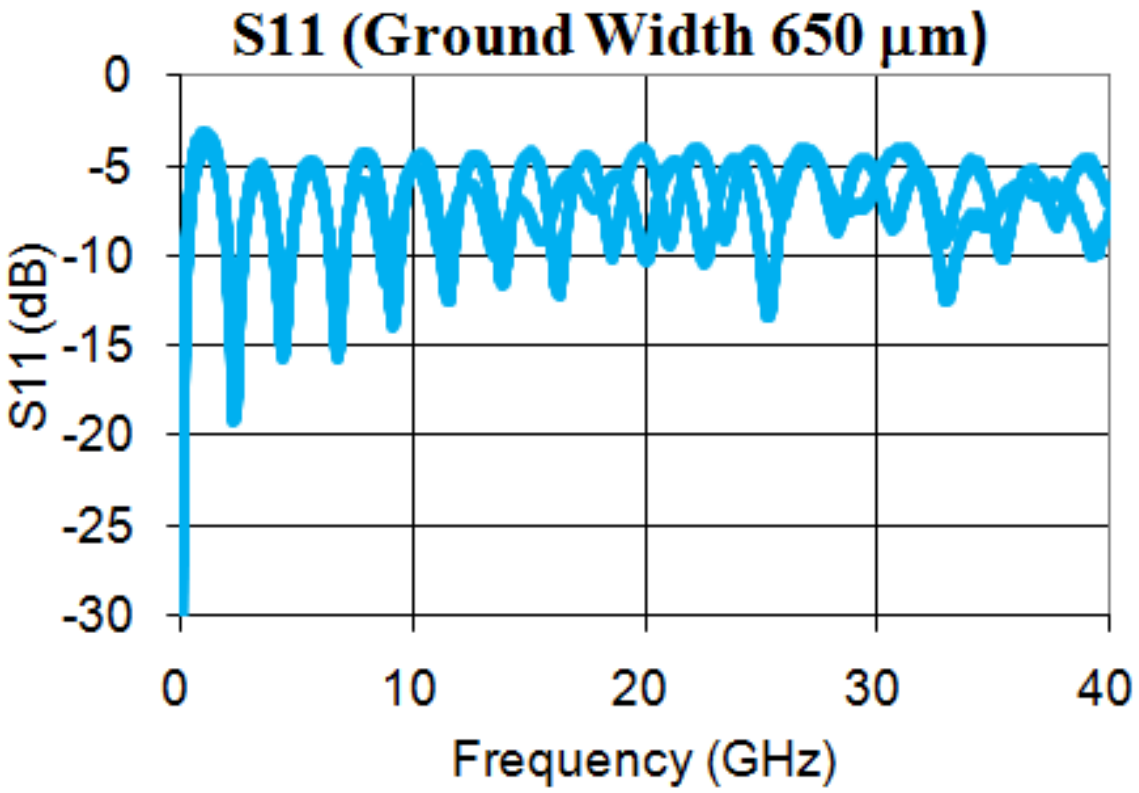

Figure 7.12 S11measurements for 650 µm wide ground lines

From the definition of phase loss in Eq. 7.5, an effective dielectric constant can be determined from the unwrapped phase of the S-parameter measurements. The effective dielectric constant, based on a line length of 5.8 cm is plotted in Figure 7.13. Wide ground structures show slightly lower effective dielectric constants, which is expected. All line dielectric constants are between 1.25 and 1.45. These values are extremely impressive for a fully encapsulated copper signal wire because the encapsulating dielectric only contributes a small portion to the overall capacitance.

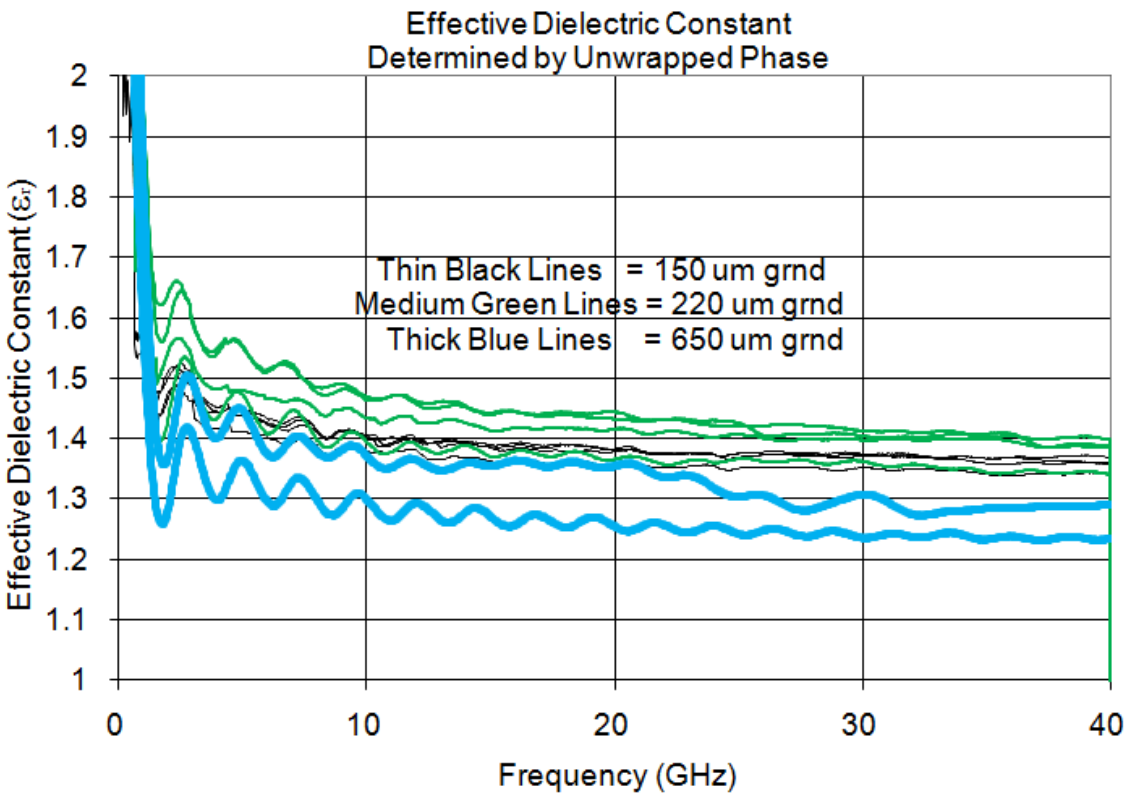

Figure 7.13 Effective dielectric constant (ε_r) determined by unwrapped phase

The attenuation in the conductor and dielectric can be estimated using the effective dielectric constant determined from the S-parameters and the loss tangent determined by LCR meter. Using Equation 7.3 to calculate the attenuation in the conductor and Equation 7.5 to calculate attenuation in the dielectric, a comparison between data and theory can be made. The conductor loss can be modified by the root mean square surface roughness. Based on these electrical properties and the air cavity thickness *d* between lines measured from Figures 7.3 through 7.6, a calculation of overall attenuation in the line is calculated and plotted in Figure 7.14.

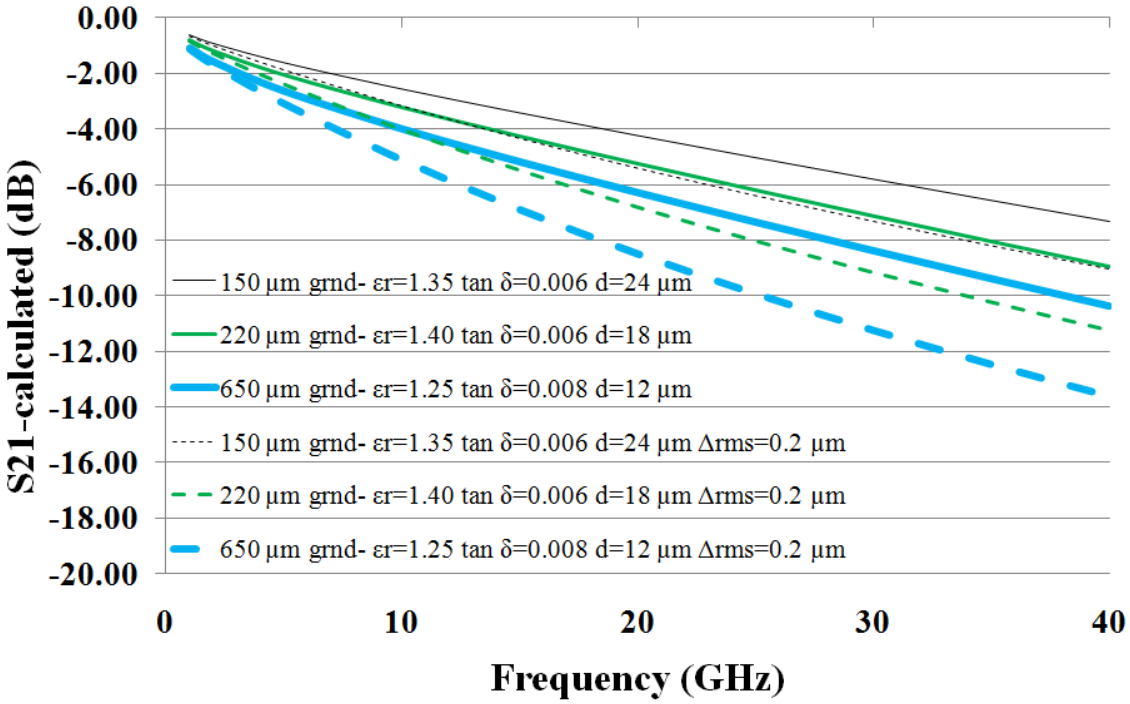

Figure 7.14 Calculated S21 based on conductor loss from Equation 3 and Equation 4 and dielectric loss from Equation 7.5. Total attenuation including surface roughness effects are shown in dashed lines.

7.6. Conclusions

Attenuation in off-chip signal wires will continue to be a critical limitation for low power chips with large bandwidth. Low-loss transmission lines with an air cavity dielectric offer the lowest achievable loss because of a relative permittivity near one and essentially zero loss tangent. The air cavity lines described in this paper exhibited low dielectric constants and low loss tangents.

Air cavity microstriplines and parallel plate lines described here had effective dielectric constants below 1.5. Some uncertainty is associated with this calculation because of probe pad effects as well as surface roughness on the board and copper surface. Because the effective dielectric constant is limited by fringing fields due to geometrical layout of the line, further reduction of the dielectric constant is not seen as

practical.

Improved line characteristics will benefit design of associated transmission circuitry. Better signal quality allows lower transmit powers and simpler decoding circuitry. Differential signaling can enhance data rates by offering better noise immunity and lower swing voltages and could be coupled with the high performance air cavity lines described here. Air cavities housing multiple conductors have also been fabricated using the techniques described here. Their electrical performance has not been characterized but will be evaluated in future work.

8. SUMMARY AND CONCLUSIONS

8.1. Summary

The air cavity parallel plate and microstrip lines presented in Chapter 3 and Chapter 7 represent the only literature reported air gap transmission line structures fabricated on low-cost epoxy-fiberglass substrates. The structures in Chapter 3 are novel because they incorporate an air cavity below the signal conductor, but the general geometry is roughly that of a microstrip line. The structures in Chapter 7 are particularly impressive because the dielectric remains low despite having a relatively higher dielectric constant above the line.

Process advancements in the understanding of sacrificial PPC decomposition during pattern develop and air cavity formation. The unique aspects of the interaction of PPC with copper enabled a self-patterning process step which could be cleverly integrated into a process flow to reduce production steps. Overcoats based on inorganic-organic hybrid monomers were evaluated as encapsulants due to their potential to resist various chemical species. Avatrel 8000P was adopted as the encapsulant due to its superior mechanical properties and processibility.

8.2. Conclusions

The air cavity parallel plate and microstrip lines presented in Chapter 7 is the first reported fully encapsulated line to suspend one copper metal line above another. The low attenuation reported for these lines is particularly impressive in light of the fact they were built on very rough FR-4 substrates as opposed to the semiconductor and ceramic substrates reported in literature. Attenuation of -5 dB is calculated from Equation 7.3 for

a 5.8 cm long line for perfectly smooth copper surfaces with no dielectric loss and a plate spacing of 18 μm (same as the parallel plate lines reported here). This is the physical limit based on the finite conductivity of the copper conductor. Further improvement of these lines will be difficult because of the need for an encapsulating layer and the limitations of surface roughness on epoxy-fiberglass boards.

Overcoat materials and encapsulating layers will continue to be a challenge for the integration of air-cavity transmission lines. The challenges of sagging overcoats observed in Chapter 7 were resolved to some extent by using a higher modulus overcoat. However, slightly thicker overcoats were used in Chapter 7, so direct comparison of their processing characteristics was not possible.

Thicker overcoats, although better for structural reasons, are undesirable for integration with microelectronics because vias must be etched through the overcoat material and plated with metal to connect wires on different levels. Because vias are limited by aspect ratio, thicker overcoats require wider via structures, decreasing the density of interconnections.

Thinner overcoats allow a greater via density at the expense of less structurally robust films. Thin polymer films are susceptible to sagging, especially at the elevated temperatures of the air cavity decomposition, while thin glasses easily crack. Composite layers of alternating polymer and glass have shown promise and were the motivation for the work in Chapter 6, but the structural benefits of composite layers are offset by the added processing complexity and need for multiple etch steps for via formation.

Thinner overcoat materials may also do little to improve the electrical loss characteristics of structures similar to the ones reported here. This is because the more

rigid, higher modulus overcoat materials also tend to have higher dielectric constants. Thus, any benefit from decreasing the overcoat thickness with a higher modulus material to minimize fringing field effects will likely be offset by slightly higher loss due to the higher dielectric constant of the material.

Although these BECHETS and ECHETS blends were not satisfactory to replace polynorbornene-based overcoats, they still may be of interest for use in composite over coats or as an encapsulant for chip packaging. The superior resistance to chemical and plasma assisted etches indicate the potential for passivation. Investigation of gas permeability would be required to more fully evaluate BECHETS or ECHETS for these applications. For air-gap overcoats, however, Avatrel 8000P will remain the preferred choice due to its superior modulus and processibility.

One important drawback of Avatrel 8000P is that it is dispensed in propylene glycol methyl ether acetate (PGMEA), a polar solvent which readily dissolves PPC. When overcoating PPC, the sacrificial pattern distorts slightly as the PPC is temporarily redissolved before drying during overcoat softbake. While this did not cause any difficulties in building the dimensions featured in this work, scaling down this process would be difficult because of the probability of delaminating the sacrificial material. An overcoat material such as a spin-on glass or PECVD SiO_2 would be required to passivate the PPC from dissolution into PGMEA. As mentioned in Chapter 5, the passivating dielectric could be integrated into a process flow to act as a diffusion barrier layer and to provide confining stress on the conductor.

Another critical remaining challenge to further improving the electrical transmission lines presented here is the surface roughness. The surface roughness amplifies attenuation

in the conductor. Because no conductors are superior to copper for low resistivity and high electromigration resistance, copper will remain the metal of choice for the foreseeable future and every effort should be made to minimize additional attenuation in the conductor due to the surface roughness. Although Equation 7.4 can be used to express this additional attenuation, it has been criticized because it may underestimate attenuation in extremely rough surfaces[133].

The rms surface roughness of the structures fabricated here are between 0.1 μm and 0.5 μm. As was illustrated in Figure 7.14, surface roughness can substantially increase the loss in the line, even when surface roughness is small. Surface roughness in typical FR-4 boards is between 0.4 μm and 0.5 μm locally and may be much larger across the substrate[134].

Surface roughness of boards will likely remain relatively constant as the roughness provides physical anchoring for photoresist, metal lines, and other build-up layers. Techniques which planarize conductors prior to air-gap encapsulation or during the encapsulation process would be valuable and could be implemented by using chemical mechanical polishing or by adding leveling agents[135]. Such techniques may be undesirable may be undesirable because uniform polishing across large surface areas such as printed circuit boards is difficult. Additionally, leveling agents are typically based on the reflow of solder, which would result in a surface layer of higher resistivity metal at the surface interface, especially important given the reduced skin depth in the GHz frequency range.

Techniques to integrate air cavities for lower cost are required to make such technologies viable. Print and etch manufacturing techniques used to manufacture

conventional PCB boards are advantageous because of the simplicity of steps. Similarly, techniques for making multilayer boards utilize the low cost print and etch techniques and via metallization. Imprint lithography represents a valuable opportunity in improving the manufacturability of air-cavity transmission lines because a line and via can be simultaneously formed, eliminating masking and plating steps as well as the need for alignment. Additionally, the smooth transitions eliminate reflections and improve the quality of the data channel. The unique interaction of PPC with copper detailed in Chapter 5 is ideal for coupling with imprint lithography because of the self-patterning nature of the PPC on copper. A cleverly designed process could utilize the interaction of PPC and copper to create a line and via encapsulated by PPC, which after decomposition would allow a copper signal wire with smooth transitions in an air dielectric environment.

Few techniques remain to achieve the 0.20 pJ/bit milestone set forth by the ITRS because the physical limit of single-ended wire transmission lines is quickly approaching. Differential signaling across electrical wires and optical signaling offer potential solutions to increasing the energy efficiency of communication. Optical signaling suffers from challenges with low capacitance detectors and electro-optic overhead concerns discussed briefly in the introduction. Differential signaling, however, extends the use of copper signal wires by combining the benefits of low power signaling, low loss transmission lines, and good noise immunity. Air cavities housing multiple conductors will be of interest because the lower swing voltage and better noise immunity means less power is consumed in the transmitter and receiver, collectively. Design of the signal wires will be critical to minimizing transmission losses. In order to maximize benefits from the low permittivity environment, air-gap differential pairs may require copper

conductors supported on dielectric posts or strips as in Chapter 2 so more of the electric field travels through the air. Beyond the limitation of low loss signal wires in differential configurations using active signaling techniques to maximize the data on a waveform, the only alternative is for communication distances to decrease.

APPENDIX A

Cross-section of cake served at Ph.D. thesis defense presentation.

REFERENCES

1. De Vries, T.S. and Vedejs, E., *Electrophilic Activation of Lewis Base Complexes of Borane with Trityl Tetrakis(pentafluorophenyl)borate.* Organometallics, 2007. **26**: p. 3079-3081.

2. Djordjevic, A.R., Likar-Smiljanic, V.D., and Sarkar, T.K., *Wideband frequency-domain characterization of FR-4 and time-domain causality.* IEEE Transactions on Electromagnetic Compatibility, 2001. **43**: p. 662-667.

3. Simpson, J.J., Taflove, A., Mix, J.A., and Heck, H., *Substrate Integrated Waveguides Optimized for Ultrahigh-Speed Digital Interconnects.* IEEE Transactions on Microwave Theory and Techniques, 2006. **54**(5): p. 1983-1990.

4. Sinsky, J., Duelk, M., and Adamiecki, A., *High-speed electrical backplane transmission using duobinary signaling.* IEEE Transactions on Microwave Theory and Techniques, 2005. **53**: p. 152-166.

5. Kohl, P.A., Zhao, Q., Patel, K., Schmidt, D., Bidstrup Allen, S.A., Shick, R., and Jayaraman, S., *Air-Gaps for Electrical Interconnections.* Electrochemical and Solid-State Letters, 1998. **1**(1): p. 49-51.

6. Reed, H.A., White, C.E., Rao, V., Bidstrup Allen, S.A., Henderson, C.L., and Kohl, P.A., *Fabrication of microchannels using polycarbonates as sacrificial materials.* Journal of Micromechanics and Microengineering, 2001. **11**: p. 733-737.

7. Bhusari, D., Reed, H.A., Wedlake, M., Padovani, A.M., Bidstrup Allen, S.A., and Kohl, P.A., *Fabrication of Air-Channel Structures for Microfluidic, Microelectromechanical, and Microelectronic Applications.* Journal of Microelectromechanical Systems, 2001. **10**(3): p. 400-408.

8. Jayachandran, P.J., Reed, H.A., Zhen, H., Rhodes, L.F., Henderson, C.L., Bidstrup Allen, S.A., and Kohl, P.A., *Air-Channel Fabrication for Microelectromechanical Systems via Sacrificial Photosensitive Polycarbonates.* Journal of Microelectromechanical Systems, 2003. **12**(2): p. 147-159.

9. Pozar, D., *Microwave Engineering*. 3 ed. 2004, New York: J.W. Wiley & Sons. 98-105, 143-145, 272-280.

10. Ayoub, A.F.A., *Analysis of rectangular microstrip antenna with air substrates.* Journal of Electromagnetic Waves and Applications, 2003. **17**: p. 1755-1766.

11. Bahl, I.J. and Trivedi, D.K., *A designer's guide to microstrip line.* Microwaves, 1977: p. 174-182.

12. Lee, K.F. and Dahele, J.S., *Circular disc microstrip antenna with an airgap.* IEEE Transactions on Antennas and Propagation, 1984. **AP-32**: p. 880-884.

13. Jeong, I., Shin, S.H., Go, J.H., Lee, J.S., Nam, C.M., Kim, D.W., and Kwon, Y.S., *High-performance air-gap transmission lines and inductors for millimeter wave applications.* IEEE Transactions on Microwave Theory and Techniques, 2002. **50**(12): p. 2850-2855.

14. Lee, H.S., Kim, S.C., Lim, B.O., Kim, K.M., Uhm, W.Y., Chun, Y.H., Shin, D.H., Kim, S.K., Park, H.C., and Rhee, J.K., *New micromachined microstrip transmission lines for application in millimeter wave circuits.* Microwave and Optical Technology Letters, 2004. **40**: p. 6-9.

15. Lee, H.S., Shin, D.H., Kim, S.C., Lim, B.O., Baek, T.J., Ko, B.S., Chun, Y.H., Kim, S.K., Park, H.C., and Rhee, J.K., *Fabrication of new micromachined transmission line with dielectric posts for millimeter-wave applications.* Journal of Micromechanics and Microengineering, 2004. **14**: p. 746-749.

16. Anand, M.B., Yamada, M., and Shibata, H., *Use of gas as low-k interlayer dielectric in LSI's: Demonstration of feasibility.* IEEE Transactions on Electron Devices, 1997. **44**: p. 1965-1971.

17. Debatosh, G. and Siddiqui, J.Y., *Resonant frequency of equilateral triangular microstrip antenna with and without air gap.* IEEE Transactions on Antennas and Propagation, 2004. **52**: p. 2174-2177.

18. Queck, C.K. and Davis, L.E., *Improved design of microstrip air-bridges.* International Journal of RF and Microwave Computer Aided Engineering, 2003. **13**: p. 246-255.

19. Havemann, I.H. *Thermal Conductivity of Particle Reinforced Polymer Composites*. in *NATOASI*. 2003.

20. Eisenstadt, W.R. and Eo, Y., *S-parameter-based IC interconnect transmission line characterization.* IEEE Transactions on Components, Hybrids and Manufacturing Technology, 1992. **15**: p. 483-490.

21. Sinsky, J., Duelk, M., and Adamiecki, A., *High-speed electrical backplane transmission using duobinary signaling.* IEEE Transactions on Microwave Theory and Techniques, 2005. **53**: p. 152-160.

22. Wu, X., Reed, H.A., Wang, Y., Rhodes, L.F., Elce, E., Ravikiran, R., Shick, R.A., Henderson, C.L., Allen, S.A., and Kohl, P.A., *Fabrication of Microchannels using Polynorbornene Photosensitive Sacrificial Materials.* Journal of the Electrochemical Society, 2003. **150**(9): p. H205-H213.

23. Inoue, S., Koinuma, H., and Tsuruta, T., *Copolymerization of carbon dioxide and epoxide.* Journal of Polymer Science: Part B: Polymer Letters, 1969. **7**: p. 287-292.

24. Thorat, S.D., Phillips, P.J., Semenov, V., and Gakh, A., *Physical Properties of Aliphatic Polycarbonates Made from CO2 and Epoxides.* Journal of Applied Polymer Science, 2003. **89**(5): p. 1163-1176.

25. Zhu, Q., Meng, Y.Z., Tjong, S.C., Zhao, X.S., and Chen, Y.L., *Thermally stable and high molecular weight poly(propylene carbonate)s from carbon dioxide and propylene oxide.* Polymer International, 2002. **51**: p. 1079-1085.

26. Tao, Y., Wang, X., Chen, X., Zhao, X., and Wang, F., *Regio-Regular Structure High Molecular Weight Poly(propylene carbonate) by Rare Earth Ternary Catalyst and Lewis Base Cocatalyst.* Journal of Polymer Science: Part A: Polymer Chemistry, 2008. **46**: p. 4451-4458.

27. Peng, S., An, Y., Chen, C., Fei, B., Zhuang, Y., and Dong, L., *Thermal degradation kinetics of uncapped and end-capped poly(propylene carbonate).* Polymer Degradation and Stability, 2003. **80**: p. 141-147.

28. Du, L., Qu, B., Meng, Y., and Zhu, Q., *Structural characterization and thermal and mechanical properties of poly(propylene carbonate)/MgAl-LDH exfoliation nanocomposite via solution intercalation.* Composites Science and Technology, 2006. **66**: p. 913-918.

29. Gao, L.J., Du, F.G., Xiao, M., Wang, S.J., and Meng, Y.Z., *Thermally stable aliphatic polycarbonate containing bulky carbazole pendants.* Journal of Applied Polymer Science, 2008. **108**(6): p. 3626-3631.

30. Gao, L.J., Xiao, M., Wang, S.J., and Meng, Y.Z., *Thermally Stable Poly(propylene carbonate) Synthesized by Copolymerizing with Bulky Napthalene Containing Monomer.* Journal of Applied Polymer Science: Part B, 2008. **108**(2): p. 1037-1043.

31. Li, X.H., Tjong, S.C., Meng, Y.Z., and Zhu, Q., *Fabrication and Properties of Poly(propylene carbonate)/Calcium Carbonate Composites.* Journal of Polymer Science: Part B: Polymer Physics, 2003. **41**: p. 1806-1813.

32. Song, P.F., Xiao, M., Du, F.G., Wang, S.J., Gan, L.Q., Liu, G.Q., and Meng, Y.Z., *Synthesis and Properties of Aliphatic Polycarbonates Derived from Carbon Dioxide, Propylene Oxide, and Maleic Anhydride.* Journal of Applied Polymer Science, 2008. **109**: p. 4121-4129.

33. Yu, T., Yong, Z., Liu, K., Zhao, Y., Chen, E., Wang, F., and Wang, D., *Improving thermal stability of biodegradable aliphatic polycarbonate by metal ion coordination.* Polymer Degradation and Stability, 2009. **94**(2): p. 253-258.

34. Yu, T., Zhou, Y., Zhao, Y., Liu, K., Chen, E., Wang, D.Y., and Wang, F., *Hydrogen-Bonded Thermostable Liquid Crystalline Complex Formed by Biodegradable Polymer and Amphiphilic Molecules.* Macromolecules, 2008. **41**: p. 3175-3180.

35. Zhang, Z., Lee, J.-H., Lee, S.-H., Heo, S.-B., and Pittman Jr., C.U., *Morphology, thermal stability and rheology of poly(propylene carbonate)/organoclay nanocomposites with different pillaring agents.* Polymer, 2008. **49**: p. 2947-2956.

36. Zhang, Z., Mo, Z., Zhang, H., Zhang, Y., Na, T., An, Y., Wang, X., and Zhao, X., *Miscibility and Hydrogen-Bonding Interactions in Blends of Carbon Dioxide/Epoxy Propane Copolymer with Poly(p-vinylphenol).* Journal of Polymer Science: Part B: Polymer Physics, 2002. **40**: p. 1957-1964.

37. Li, X.H., Meng, Y.Z., Zhu, Q., and Tjong, S.C., *Thermal decomposition characteristics of poly(propylene carbonate) using TG/IR and Py-GC/MS techniques.* Polymer Degradation and Stability, 2003. **81**: p. 157-165.

38. Du, L.C., Meng, Y.Z., Wang, S.J., and Tjong, S.C., *Synthesis and Degradation Behavior of Poly(Propylene Carbonate) Derived from Carbon Dioxide and Propylene Oxide.* Journal of Applied Polymer Science, 2004. **92**: p. 1840-1846.

39. Yan, H., Cannon, W.R., and Shanefield, D.J., *Thermal Decomposition Behavior of Poly(propylene carbonate).* Ceramics International, 1998. **24**: p. 433-439.

40. Cupta, M.G., Joseph, P.J., and Kohl, P.A., *Photoacid generators for catalytic decomposition of polycarbonate.* Journal of Applied Polymer Science, 2007. **105**(5): p. 2655-2662.

41. White, C.E., Balogun, A., and Henderson, C.L., *Effects of the Photoacid Generator Type on the Imaging and Thermal Decomposition Properties of Photodefinable, Thermally Sacrificial Poly(propylene carbonate) Materials.* Journal of Applied Polymer Science, 2006. **102**: p. 266-271.

42. Dang, B., Joseph, P., Bakir, M., Spencer, T., Kohl, P., and Meindl, J. *Wafer-Level Microfluidic Cooling Interconnects for GSI*. in *IEEE- International Interconnect Technology Conference (IITC)*. 2005. San Fransisco, CA.

43. Metz, S., Jiguet, S., Bertsch, A., and Renaud, P., *Polyimide and SU-8 microfluidic devices manufactured by heat-depolymerizable sacrificial material technique.* Lab on a Chip, 2004. **4**: p. 114-120.

44. Spencer, T.J., Joseph, P.J., Kim, T.H., Swaminathan, M., and Kohl, P.A., *Air-Gap Transmission Lines on Organic Substrates for Low-Loss Interconnects.* IEEE Transactions on Microwave Theory and Techniques, 2007. **55**(9): p. 1919-1925.

45. Joseph, P.J., Monajemi, P., Ayazi, F., and Kohl, P.A., *Wafer-level packaging of micromechanical resonators.* IEEE Transactions on Advanced Packaging, 2007. **30**(1): p. 19-26.

46. Lu, J.Y., Yu, C.P., Chang, H.C., Chen, H.W., Li, Y.T., Pan, C.L., and Sun, C.K., *Terahertz air core microstructure fiber.* Applied Physics Letters, 2008. **92**: p. 064105-1-064105-3.

47. Hassani, A., Dupuis, A., and Skorobogatiy, M., *Low loss porous terahertz fibers containing multiple subwavelength holes.* Applied Physics Letters, 2008. **92**: p. 071101-1-071101-3.

48. Yan, H., Cannon, W.R., and Shanefield, D.J., *Evolution of carbon during burnout and sintering of tape-cast aluminum nitride.* Journal of the American Ceramic Society, 1993. **76**: p. 166-172.

49. Wedlake, M. and Kohl, P.A., *Thermal decomposition kinetics of functionalized polynorbornene.* Journal of Materials Research, 2002. **17**(3): p. 632-340.

50. Jones III, C.A. and DeSimone, J.M., *Critical Phase Polymerizations*, in *Encyclopedia of Polymer Science and Technology*. 2002, John Wiley & Sons, Inc. p. 111-126.

51. Liu, B., Zhao, X., Wang, X., and Wang, F., *Thermal Degradation Kinetics of Poly(propylene carbonate) Obtained from the Copolymerization of Carbon Dioxide and Propylene Oxide.* Journal of Applied Polymer Science, 2003. **90**: p. 947-953.

52. Chen, S., Xiao, Z., and Ma, M., *Copolymerization of Carbon Dioxide and Epoxides with a Novel Effective Zn–Ni Double-Metal Cyanide Complex.* Journal of Applied Polymer Science, 2008. **107**: p. 3871-3877.

53. Tao, Y., Wang, X., Zhao, X., Li, J., and Wang, F., *Crosslinkable Poly(propylene carbonate): High-Yield Synthesis and Performance Improvement.* Journal of Applied Polymer Science: Part A: Chemistry, 2006. **44**: p. 5329-5336.

54. Qin, Y., Wang, X., Zhang, S., Zhao, X., and Wang, F., *Fixation of Carbon Dioxide into Aliphatic Polycarbonate, Cobalt Porphyrin Catalyzed Regio-Specific Poly(propylene carbonate) with High Molecular Weight.* Journal of Applied Polymer Science: Part A: Chemistry, 2008. **46**: p. 5959-5967.

55. Darensbourg, D.J., Lewis, S.J., Rodgers, J.L., and Yarbrough, J.C., *Carbon Dioxide/Epoxide Coupling Reactions Utilizing Lewis Base Adducts of Zinc Halides as Catalysts. Cyclic Carbonate versus Polycarbonate Production.* Inorganic Chemistry, 2003. **42**(2): p. 581-589.

56. Meng, Y.Z., Du, L.C., Tiong, S.C., Zhu, Q., and Hay, A.S., *Effects of the Structure and Morphology of Zinc Glutarate on the Fixation of Carbon Dioxide into Polymer.* Journal of Polymer Science: Part A: Polymer Chemistry, 2002. **40**: p. 3579-3591.

57. Li, B., Wu, G.P., Ren, W.M., Wang, Y.M., Rao, D.Y., and Lu, X.B., *Asymmetric, Regio- and Stereo-Selective Alternating Copolymerization of CO_2 and Propylene Oxide Catalyzed by Chiral Chromium Salan Complexes.* Journal of Polymer Science: Part A: Polymer Chemistry, 2008. **46**: p. 6102-6113.

58. Lu, L. and Huang, K., *Synthesis and characteristics of a novel aliphatic polycarbonate, poly[(propylene oxide)-co-(carbon dioxide)-co-(γ-butyrolactone)]*. Polymer International, 2005. **54**: p. 870-874.

59. Aikawa, S., Yoshida, Y., Nishiyama, S., Noguchi, H., and Shoji, A., *Optical Properties of Poly(Propylene Carbonate) which Contains $C_{60}(OH)_n$ Structure in the End of Polymer Chain.* Molecular Crystal Liquid Crystal, 2006. **445**: p. 315/[606]-321[611].

60. Guan, L.T., Du, F.G., Wang, G.Z., Chen, Y.K., Xiao, M., Wang, S.J., and Meng, Y.Z., *Foaming and chain extension of completely biodegradable poly(propylene carbonate) using DPT as blowing agent.* Journal of Polymer Research, 2007. **14**: p. 245-251.

61. Guan, L.T., Xiao, M., and Meng, Y.Z., *Chemically Foaming of Biodegradable Poly(propylene carbonate) Derived from Propylene Oxide and Carbon Dioxide.* Polymer Engineering and Science, 2006: p. 153-159.

62. Liu, Q., Zou, Y., Bei, Y., Qi, G., and Meng, Y., *Mechanic properties and thermal degradation kinetics of terpolymer poly(propylene cyclohexene carbonate)s.* Materials Letters, 2008. **62**: p. 3294-3296.

63. Luinstra, G.A., *Poly(Propylene Carbonate), Old Copolymers of Propylene Oxide and Carbon Dioxide with New Interests: Catalysis and Material Properties.* Polymer Reviews, 2008. **48**: p. 192-219.

64. Luinstra, G.A. and Molnar, F., *Poly(propylene carbonate), old CO2 Copolymer with New Attractiveness.* Macromolecular Symposia, 2007. **259**: p. 203-209.

65. Shi, X. and Gan, Z., *Preparation and characterization of poly(propylene carbonate)/montmorillonite nanocomposites by solution intercalation.* European Polymer Journal, 2007. **43**: p. 4852-4858.

66. Yang, D.Z. and Hu, P., *Miscibility, Crystallization, and Mechanical Properties of Poly(3-hydroxybutyrate) and Poly(propylene carbonate) biodegradable blends.* Journal of Applied Polymer Science, 2008. **109**: p. 1635-1642.

67. Huang, Y., Wang, J., Liao, B., Chen, M., and Cong, G., *Epoxy Resins Toughened by Poly(propylene carbonate).* Journal of Applied Polymer Science, 1998. **64**(12): p. 2457-2465.

68. Ma, X., Chang, P.R., Yu, J., and Wang, N., *Preparation and properties of biodegradable poly(propylene carbonate)/thermoplastic dried starch composites.* Carbohydrate Polymers, 2008. **71**: p. 229-234.

69. Jiao, J., Xiao, M., Shu, D., Li, L., and Meng, Y.Z., *Preparation and Characterization of Biodegradable Foams from Calcium Carbonate Reinforced Poly(propylene carbonate) Composites.* Journal of Applied Polymer Science, 2006. **102**: p. 5240-5247.

70. Pang, M.Z., Qiao, J.J., Wang, S.J., Xiao, M., and Meng, Y.Z., *Miscibility and Properties of Completely Biodegradable Blends of Poly(propylene carbonate) and Poly(butylene succinate)*
Journal of Applied Polymer Science, 2008. **107**: p. 2854-2860.

71. Ning, W., Zhang, X., Yu, J., and Jianming, F., *Partially miscible poly(lactic acid)-blend-poly(propylene carbonate) filled with carbon black as conductive polymer composite.* Polymer International, 2008. **57**: p. 1027-1035.

72. Zhang, Z., Zhang, H., Zhang, Q., Zhou, Q., Zhang, H., Mo, Z., Zhao, X., and Wang, X., *Thermotropic Liquid Crystallinity, Thermal Decomposition Behavior,*

and Aggregated Structure of Poly(propylene carbonate)/Ethyl Cellulose Blends. Journal of Applied Polymer Science, 2006. **100**: p. 584-592.

73. Luinstra, G.A., Haas, G.R., Molnar, F., Bernhart, V., Eberhart, R., and Rieger, B., *On the formation of aliphatic polycarbonates from epoxides with chromium(III) and aluminum(III) metal-salen complexes.* Chemistry: A European Journal, 2005. **11**(21): p. 6298-6314.

74. Joshi, S.S. and Mebel, A.M., *Computational modeling of biodegradable blends of starch amylose and poly-propylene carbonate.* Polymer, 2008. **48**(13): p. 3893-3901.

75. Zhang, Z., Shi, Q., Peng, J., Song, J., Chen, Q., Yang, J., Gong, Y., Ji, R., He, X., and Lee, J.-H., *Partial delamination of the organo-montmorillonite with surfactant containing hydroxyl groups in maleated poly(propylene carbonate).* Polymer, 2006. **47**: p. 8548-8555.

76. Lu, L., Liu, S., and Huang, K., *Molecular Simulation of Structure and Loading-Drug Character of Poly(propylene-co-γ-butyrolactone carbonate).* Journal of Applied Polymer Science, 2008. **107**: p. 872-880.

77. Cupta, M., *Photoacid Generators for Catalytic Decomposition of Polycarbonate*, in *School of Chemical & Biomolecular Engineering*. 2005, Georgia Tech. p. 137.

78. Chen, Y. and Wang, Q., *Thermal oxidative degradation kinetics of flame-retarded polypropylene with intumescent flame-retardant master batches in situ prepared in twin-screw extruder.* Polymer Degradation and Stability, 2007. **92**: p. 280-291

79. Ozawa, T., *Kinetic Analysis of Derivative Curves in Thermal Analysis.* Journal of Thermal Analysis, 1970. **2**: p. 301-324.

80. Ozawa, T., *A New Method of Analyzing Thermogravimetric Data.* Bulletin of the Chemical Society of Japan, 1965. **38**: p. 1881-1886.

81. Flynn, J.H. and Wall, L.A., *A Quick, Direct Method for the determination of activation energy from thermogravimetric data.* Journal of Polymer Science: Part B: Polymer Letters, 1966. **4**(5): p. 323-328.

82. Nasirzadeh, K., Neueder, R., and Kunz, W., *Vapor Pressures of Propylene Carbonate and N,N-dimethylacetimide.* Journal of Chemical Engineering Data, 2005. **50**: p. 26-28.

83. Chernyak, Y. and Clements, J.H., *Vapor Pressure and Heat Capacity of Alkylene Carbonates.* Journal of Chemical Engineering Data, 2004. **49**: p. 1180-1184.

84. Verevkin, S.P., *Determination of Vapor Pressures and Enthalpies of Vaporization of 1,2-alkanediols.* Fluid Phase Equilibria, 2004. **224**: p. 23-29.

85. Moore, T., Adhikari, R., and Gunatillake, P., *Chemosynthesis of bioresorbable poly(g-butyrolactone) by ring-opening polymerisation: a review.* Biomaterials, 2005. **26**: p. 3771-3782.

86. van der Mee, L., Helmich, F., de Bruijn, R., Vekemans, J.A.J.M., Palmans, A.R.A., and Meijer, E.W., *Investigation of Lipase-Catalyzed Ring-Opening Polymerizations of Lactones with Various Ring Sizes: Kinetic Evaluation.* Macromolecules, 2006. **39**: p. 5021-5027.

87. Houk, K.N., Jabbari, A., Hall Jr., H.K., and Aleman, C., *Why δ-Valerolactone Polymerizes and γ-Butyrolactone Does Not.* Journal of Organic Chemistry, 2008. **73**(7): p. 2674-2678.

88. Spencer, T.J. and Kohl, P.A., *Decomposition of Poly(propylene carbonate) with UV Sensitive Iodonium Salts.* Polymer Degradation and Stability, 2009. **Submitted for review on 3/1/2010**.

89. Niu, Y., Zhang, W., Li, H., Chen, X., Sun, J., Zhuang, X., and Jing, X., *Carbon dioxide/propylene oxide coupling reaction catalyzed by chromium salen complexes.* Polymer, 2009. **50**(2): p. 441-446.

90. Qin, Y.S., Qing, W.M., Xian, H.W., Sun, J.Z., Zhao, X.J., and Wang, F.S., *Electron-beam irradiation on poly(propylene carbonate) in the presence of polyfunctional monomers.* Polymer Degradation and Stability, 2007. **92**: p. 1942-1947.

91. Zacharia, R.E., Simon, S.L., Beckman, E.J., and Enick, R.M., *Improving the thermal stability of a polymer through liquid carbon dioxide extraction of a metal compound.* Polymer Degradation and Stability, 1999. **63**: p. 85-88.

92. Wu, M.S., Chiang, P.C.J., Lin, J.C., and Lee, J.T., *Effects of copper trifluoromethanesulphonate as an additive to propylene carbonate-based electrolyte for lithium-ion batteries.* Electrochimica Acta, 2004. **49**: p. 4379-4386.

93. Anson, C.E., Ponikiewski, L., and Rothenberger, A., *Halide Abstraction from Organic Solvents in Reactions of a Copper(I) Alkoxide: Synthesis and Crystal Structures of [Cu5(dppm)(dppm-)2(OtBu)Cl2] and [Cu3(dppm)3Br2][CuBr2].*

Zeitschrift für anorganische und allgemeine Chemie, 2006. **632**(15): p. 2402-2404.

94. Crivello, J.V., Lockhart, T.P., and Lee, J.L., *Diaryliodonium salts as thermal initiators of cationic polymerization.* Journal of Polymer Science: Part A: Polymer Chemistry, 1983. **21**: p. 97-109.

95. Choi, Z.S., Monig, R., and Thompson, C.V., *Activation energy and prefactor for surface electromigration and void drift in Cu interconnects.* Journal of Applied Physics, 2007. **102**(8): p. 083509-1 – 083509-4.

96. *International Technology Roadmap for Semiconductors*. 2007, Semiconductor Industry Association.

97. Park, S., Bidstrup Allen, S.A., and Kohl, P.A., *Air-Gaps for High Performance On-Chip Interconnect Part I: Improvement in Thermally Decomposable Template.* Journal of Electronic Materials, 2008. **37**(10): p. 1524-1533.

98. Park, S., Bidstrup Allen, S.A., and Kohl, P.A., *Air-Gaps for High Performance On-Chip Interconnect Part II: Modeling, Fabrication, and Characterization.* Journal of Electronic Materials, 2008. **37**(10): p. 1524-1533.

99. O'Brien, S., Copuroglu, M., and Crean, G.M., *Effects of refractive index modifiers and UV light on an epoxyfunctional inorganic–organic hybrid sol–gel derived thin film system.* Applied Surface Science, 2007. **253**: p. 7969-7972.

100. VMIC.

101. Cho, Y.H., Kawade, R., Kubota, T., and Kawakami, Y., *Control of morphology and diffraction efficiency of holographic gratings using siloxane-containing reactive diluent.* Science and Technology of Advanced Materials, 2005. **6**: p. 435-442.

102. Cho, Y.H. and Kawakami, Y., *High performance holographic polymer dispersed liquid crystal systems using multi-functional acrylates and siloxane-containing epoxides as matrix components.* Applied Physics, 2006. **83**(3): p. 365-375.

103. Chung, D., Kim, J.P., Kim, D., and Lim, J., *Synthesis of Multifunctional Epoxy Monomers and their Potential Application in the Production of Holographic Photopolymers.* Journal of Industrial Engineering and Chemistry, 2006. **12**(5): p. 783-789.

104. Kawakami, Y. and Cho, Y.H., *Siloxane-containing bifunctional epoxide together with multi-functional acrylates to improve the performance of holographic gratings.* Macromolecular Symposia 2006. **240**: p. 130-140.

105. Kim, H., *Sol-gel based sulfonic acid-functionalized silica proton conductive membrane.* Journal of Power Sources, 2009. **193**(2): p. 562-569.

106. Colicchio, I., Wen, F., Keul, H., Simon, U., and Moeller, M., *Sulfonated poly(ether ether ketone)-silica membranes doped with phosphotungstic acid. Morphology and proton conductivity.* Journal of Membrane Science, 2009. **326**: p. 45-57.

107. Grunlan, M.A., Lee, N.S., Mansfeld, F., Kus, E., Finlay, J.A., Callow, J.A., Callow, M.E., and Weber, W.P., *Minimally Adhesive Polymer Surfaces Prepared from Star Oligosiloxanes and Star Oligofluorosiloxanes.* Journal of Polymer Science: Part A: Chemistry, 2006. **44**: p. 2551-2566.

108. Sbirrazzuoli, N. and Vyazovkin, S., *Learning about epoxy cure mechanisms from isoconversional analysis of DSC data.* Thermochimica Acta, 2002. **388**: p. 289-298.

109. Zong, Z., Soucek, M.D., and Xue, C., *Unusual Inorganic Phase Formation in Ultraviolet-Curable Organic-Inorganic Hybrid Films.* Journal of Polymer Science: Part A: Polymer Chemistry, 2005. **43**: p. 1607-1623.

110. Shaw, M., Nawrocki, D., Hurditch, R., and Johnson, D., *Improving the process capability of SU-8.* Microsystems Technologies, 2004. **10**(1): p. 1-6.

111. Zong, Z., Soucek, M.D., Liu, Y., and Hu, J., *Cationic Photopolymerization of Epoxynorbornane Linseed Oils: The Effect of Diluents.* Journal of Polymer Science: Part A: Polymer Chemistry, 2003. **41**: p. 3440-3456.

112. Kohl, A.T., Mimna, R., Schick, R., Rhodes, L., Wang, Z.L., and Kohl, P.A., *Low k, Porous Methylsilsesquioxane and Spin-On-Glass.* Electrochemical and Solid State Letters, 1999. **2**(2): p. 77-79.

113. Soucek, M.D. and Chen, J., *Model for the Effects of Water on the Cationic UV-Curing of Cyclohexyl Epoxides.* Journal of Coatings Technology, 2003. **75**(937): p. 49-58.

114. Udagawa, A., Yamamoto, Y., Inoue, Y., and Chujo, R., *Dynamic mechanical properties of cycloaliphatic epoxy resins cured by ultra-violet and heat-initiated cationic polymerizations.* Polymer, 1991. **32**(15): p. 2779-2784.

115. Crivello, J.V. and Lee, J.L., *Synthesis, characterization, and photoinitiated cationic polymerization of silicon-containing epoxy resins.* Journal of Polymer Science Part A: Polymer Chemistry, 1990. **28**(3): p. 479-503.

116. Hua, Y. and Crivello, J.V., *Development of Polymeric Photosensitizers for Photoinitiated Cationic Polymerization.* Macromolecules, 2001. **34**(8): p. 2488-2494.

117. Udagawa, A., Yamamoto, Y., Inoue, Y., and Chujo, R., *Plasticization and Antiplasticization Effects of Photo- and Heat-Induced Initiator Fragments Remaining in Cured Cycloaliphatic Epoxy Resins: Solid-State (13)C N.M.R. Study.* Polymer, 1991. **32**(16): p. 2947-2952.

118. Morita, Y., Tajima, S., Suzuki, H., and Sugino, H., *Thermally initiated cationic polymerization and properties of epoxy siloxane.* Journal of Applied Polymer Science, 2006. **100**(3): p. 2010-2019.

119. Rajarathinam, V., Lightsey, C.H., Osborn, T., Knapp, B., Elce, E., Allen, S.A.B., and Kohl, P.A., *Aqueous-Develop Photosensitive Polynorbornene Dielectric: Properties and Characterization.* Journal of Electronic Materials, 2009. **38**(6): p. 778-786.

120. Wang, Z., Lin, X., and Liu, W., *Synthesis of bis(2,3-epoxycyclohexyl) and its cationic photopolymerization in the presence of different diols* Polymer International, 2009. **58**(1): p. 74-80.

121. Mochalin, V.B., Kornilov, A.N., Vul'fson, A.N., and Varpakhovskaya, I.S., *Reaction of alcohols and some nitrogen-containing compounds with 2-ethoxy-Δ^3-dihydropyrans* Chemistry of Heterocyclic Compounds, 1975. **11**(2): p. 141-143.

122. Sekar, D., King, C., Dang, B., Spencer, T., Thacker, H., Joseph, P., Bakir, M., and Meindl, J. *A 3D-IC technology with integrated microchannel cooling*. in *IEEE International Interconnect Technology Conference*. 2008.

123. Cho, H., Koo, K.-H., Kapur, P., and Saraswat, K. *The delay, energy, and bandwidth comparisons between copper, carbon nanotube, and optical interconnects for local and global wiring application*. in *IEEE International Interconnect Technology Conference*. 2007.

124. Kim, J.T. and Choi, C.G., *Simultaneous optical/electrical interconnection of polymer planar-lightwave-circuit chip based on polymer MOEMS and replication technology* Sensors and Actuators A: Physical, 2006. **126**(2): p. 425-429.

125. Koo, K., Cho, H., Kapur, P., and Saraswat, K., *Performance comparisons between carbon nanotubes, optical, and Cu for future high-performance on-chip interconnect applications.* IEEE Transactions on Electron Devices, 2007. **54**(12): p. 3206-3215.

126. Park, S.H., Allen, S.A.B., and Kohl, P.A., *Air-Gaps for High-Performance On-Chip Interconnect Part I: Improvement in Thermally Decomposable Template.* Journal of Electronic Materials, 2008. **37**(10): p. 1524-1533.

127. Gosset, L.G., Arnal, V., Brun, P., Broekaart, M., Monget, C., Casanova, N., Rivoire, M., Oberlin, J.C., and Torres, J., *Integration of SiOC air gaps in copper interconnects.* Microelectronic Engineering, 2003. **70**(2-4): p. 274-279.

128. Hoofman, R.J.O.M., Caluwaerts, R., Michelon, J., Herrero Bernabé, P., Gueneau de Mussy, J.P., Bruynseraede, C., Lee, J.M., List, S., Bancken, P.H.L., and Beyer, G., *Self-aligned multi-level air gap integration.* Microelectronic Engineering, 2006. **83**(11-12): p. 2150-2154.

129. Lee, H.S., *New micromachined microstrip transmission lines for application in millimeter wave circuits.* Microwave and Optical Technology Letters, 2004. **40**: p. 6-9.

130. Lee, H., Shin, D., Kim, S., Lim, B., Baek, T., Ko, B., Chun, Y., Kim, S., Park, H., and Rhee, J., *Fabrication of new micromachined transmission line with dielectric posts for millimeter-wave applications,.* Journal of Micromechanics and Microengineering, 2004. **14**: p. 746-749.

131. Jeong, I.*e.a.*, *High-performance air-gap transmission lines and inductors for millimeter wave applications.* IEEE Transactions on Microwave Theory and Techniques, 2002. **50**: p. 2850-2855.

132. Pozar, D.M., *Microwave Engineering (Third Edition)*. 2005: John Wiley & Sons, Inc.

133. Tsang, L., Gu, X., and Braunisch, H., *Effects of Random Rough Surface on Absorption by Conductors at Microwave Frequencies.* IEEE Microwave and Wireless Components Letters, 2006. **16**(4): p. 221-223.

134. Chang, Y.T., Gaylord, T.K., and Chang, G.K., *Attenuation in waveguides on FR-4 boards due to periodic substrate undulations.* Applied Optics, 2007. **46**: p. 6476-6482.

135. Wu, X., Cullen, D., Brist, G., and Ramahi, O.M., *Surface Finish Effects on High-Speed Signal Degradation.* IEEE Transactions on Advanced Packaging, 2008. **31**(1): p. 182-189.